UNIVERSITAT POLITÈCNICA
DE CATALUNYA
BARCELONATECH

Study of the beam induced vacuum effects in the cryogenic beam vacuum chamber of the future Circular Hadron Collider

Ignasi Bellafont

UNIVERSITAT POLITÈCNICA DE CATALUNYA

DOCTORAL THESIS

Study of the beam induced vacuum effects in the cryogenic beam vacuum chamber of the Future Circular Hadron Collider

---

Author:
Ignasi BELLAFONT

Supervisor:
Dr. Roberto KERSEVAN
CERN. Vacuum, Surfaces and Coatings group

Thesis director:
Dr. Xavier ESCALER
UPC. Departament de Mecànica de Fluids

Co-director:
Dr. Marcos QUISPE
ALBA Synchrotron. Engineering Division

Thesis submitted in fulfilment of the
requirements for the degree of Doctor by the UPC

in the

Mechanical, Fluids and Aerospace Engineering doctoral programme

Monday 23rd November, 2020

Abstract

The Future Circular Hadron Collider (FCC-hh) is a proposal for a 100 km long hadron collider conceived as the successor of the Large Hadron Collider (LHC). The FCC-hh is designed to reach 50 TeV of beam energy, greatly surpassing the current energy frontier set by the LHC at 7 TeV. Thus, it is expected to expand the current horizon of understanding of the Standard Model of particle physics.

The beam vacuum chamber of the FCC-hh will have to cope with unprecedented levels of synchrotron radiation power for hadron colliders, around 160 times higher than its predecessor, dealing simultaneously with a tighter magnet aperture. Since the higher radiation power will result in a much higher gas load, the difficulty to achieve a good vacuum quality increases considerably compared with the LHC.

This thesis presents a study of the so-called beam induced vacuum effects in the FCC-hh, meaning the different phenomena which, due to the presence of the particle beam, have a detrimental impact on the accelerator's vacuum level. These studied effects are the photon stimulated desorption (PSD), the electron stimulated desorption (ESD) and ion stimulated desorption (ISD). Each effect has been thoroughly studied, calculating analytically and with a series of Monte Carlo simulations the resulting gas density in the chamber for all the common gas species. Finally, the feasibility of the FCC-hh from the vacuum point of view has been assessed.

To mitigate the beam induced effects and to improve the vacuum quality in the FCC-hh (essential for a proper machine operation) it was necessary to propose a new beam screen design. The new beam screen features new solutions to mitigate the e^- cloud, to handle the synchrotron radiation and a much higher pumping speed, at the expense of a higher manufacturing complexity. A dedicated experimental setup was used by CERN during the design phase to measure the vacuum performance of the developed beam screen prototypes. Finally, the obtained experimental results were compared with the theoretical results to further enhance their validity.

It is concluded that thanks to the new beam screen design, the vacuum level in the FCC-hh should be adequate. Using nominal beam parameters, the established FCC-hh vacuum specifications could be met within the first months of conditioning, a reasonable amount of time.

Resumen

El Futuro Colisionador Circular de Hadrones (FCC-hh) es un colisionador de hadrones de 100 km de longitud, propuesto como sucesor del Gran Colisionador de Hadrones (LHC). El FCC-hh está diseñado para alcanzar 50 TeV de energía de haz, superando notoriamente la frontera de energía actual establecida por el LHC, 7 TeV. De esta manera, se espera expandir las fronteras de conocimiento actuales del Modelo Estándar de la física de partículas.

La cámara de vacío del haz del FCC-hh deberá soportar niveles de potencia de radiación de sincrotrón sin precedente en los colisionadores de partículas, alrededor de 160 veces más altos que su predecesor, debiendo además de adaptarse a una apertura mucho más reducida. Dado que la alta potencia de radiación resulta en una elevada generación de gas en el sistema, la dificultad de alcanzar un buen nivel de vacío se incrementa considerablemente comparado con el LHC.

Esta tesis presenta un estudio de los efectos de vacío inducidos por el haz de partículas en el FCC-hh, esto es, los diferentes fenómenos que, debido a la presencia del haz, tienen un impacto perjudicial en el nivel de vacío del acelerador. Los efectos estudiados son la desorción inducida por fotones (PSD), la desorción inducida por electrones (ESD) y la desorción inducida por iones (ISD). Cada efecto ha sido separadamente estudiado, calculando de manera analítica y mediante simulaciones de Monte Carlo la densidad de gas resultante en la cámara para todas las especies de gas habituales. Por último, la viabilidad del FCC-hh desde el punto de vista del vacío ha sido evaluada.

Con el fin de mitigar los efectos de vacío inducidos por el haz y mejorar la calidad del vacío del FCC-hh (esencial para una correcta operación de la máquina) ha sido necesario proponer un nuevo diseño de la pantalla del haz. Este nuevo diseño presenta nuevas soluciones para mitigar la nube de electrones en la cámara, lidiar con la radiación de sincrotrón y una velocidad de bombeo mucho más alta, a expensas de una mayor complejidad en su fabricación. Además, un equipo experimental ha sido usado por el CERN durante la fase de diseño para medir el rendimiento en vacío de los prototipos de pantalla de haz construidos. Los resultados experimentales obtenidos han sido finalmente comparados con los resultados teóricos para incrementar su fiabilidad.

Se concluye que, gracias al nuevo diseño de la pantalla del haz, el nivel de vacío del FCC-hh será adecuado, alcanzando las especificaciones de vacío establecidas con parámetros de haz nominales dentro de los primeros meses de condicionamiento.

Acknowledgements

This thesis would not have been possible without the help, support, collaboration and advice of many people who directly or indirectly have contributed on its development.

First, I would like to thank Roberto Kersevan for guiding me through this thesis as my supervisor at CERN. Tireless and friendly, he always had a moment for discussions, provided me with all the experimental resources I needed and never wavered in supporting me with his knowledge and encouragement.

I would also like to extend my gratitude to Francis Pérez, who provided me with guidance during my time at ALBA and who trusted me as a doctoral student to undertake this project. I most appreciate his kind and sincere advice that helped me to effectively focus in the most important parts of my work. I thank him and Carles Colldelram for all the resources provided to carry out this study. I am also thankful to all my colleagues from ALBA, for so many nice times during these years and for those to come.

A great thank you to Xavier Escaler at the UPC for accepting the academic supervision of this thesis. I much appreciate his help with all the university formalities, which was always provided when needed, and his commitment to my thesis, from the first until the last day.

During the development of this thesis, I spent half of each year at CERN's Vacuum Group. I am truly thankful to all my colleagues and to the group leader Paolo Chiggiato, for creating such a nice work environment where the working hours passed so fast. I will always treasure all the wonderful memories I have of these years.

I am specially indebted to Lotta Mether. The inputs she provided within the frame of the WP2 and WP4 collaboration have been essential to fully evaluate the feasibility of the proposed beam screen. I am also thankful to Marco Morrone for the smooth cooperation we had in the beam screen design and in writing a common publication.

I gratefully acknowledge the support of Marton Ady in using the simulation programs he and Roberto are developing, which have been used extensively in this thesis. This thesis would not be the same without their work.

Many thanks as well to Oleg Malyshev for the interesting discussions on vacuum science, his encouraging feedback, for guiding me to his useful publications and for his collaboration in one of the published papers, and to Vincent Baglin and Cedric Garion, for the interesting discussions we had and for their vital insights on some key points of this study.

A very special acknowledgement goes to Roberto Cimino and his team from LNF-INFN, whose collaboration, carried out with the highest level of professionalism, was truly instrumental in the development of this thesis. I am also thankful for the opportunity he gave me to assist in the experimental measurements.

Furthermore, I cannot finish this part without thanking Luis González, BEXTEX's responsible and my office companion at CERN. My interaction with him, carried out on a daily basis during all the project, was extremely dynamic and fruitful. His advice on the daily issues of a PhD student and his friendship have been invaluable to me. I also wish to thank Miguel Gil-Costa and Javier Fernández, the rest of the WP4 Spanish team at CERN, for the nice collaboration we had during the project. It was great to work with them.

Finally, my deepest thanks to Laura, my couple. Without her help, patience and unconditional support during these years, this thesis would not have been possible.

Contents

List of Figures

List of Tables

List of Acronyms

AC	Amorphous Carbon
ASTEC	Accelerator Science and Technology Centre
BAG	Bayard-Alpert ionization Gauge
BESSY	Berliner Elektronenspeicherring-Gesellschaft für Synchrotronstrahlung
BESTEX	Beam Screen Test Bench Experiment
BS	Beam Screen
BW	Band Width
CB	Cold Bore
CDR	Conceptual Design Report
CERN	European Organization for Nuclear Research
COLDEX	Cold Bore Experiment
CSEM	Swiss Center for Electronics and Microtechnology
ESD	Electron Stimulated Desorption
FCC	Future Circular Collider
FCC-hh	Future Circular Lepton Collider
INFN	Instituto Nazionale di Fisica Nucleare
IP	Interaction point
HL-LHC	High luminosity LHC
IPAC	International Particle Accelerator Conference
ISD	Ion Stimulated Desorption
KARA	Karlsruhe Research Accelerator
KIT	Karlsruher Institut für Technologie
LASE	Laser Ablation Surface Engineering
LHC	Large Hadron Collider
LNF	Laboratori Nazionali di Frascati
LEP	Large Electron-Positron Collider
MB	Bending magnet
NEG	Non evaporable getter
OFE	Oxygen Free Electronic
PSD	Photon Stimulated Desorption
RF	Radio Frequency
RGA	Residual Gas Analyzer
RMS	Root Mean Square
RRR	Residual Resistivity Ratio

RT	Room Temperature
SEM	Scanning Electron Microscope
SEY	Secondary Electron Yield
SR	Synchrotron Radiation
SS	Stainless Steel
SSS	Short Straight Section
STFC	Science and Technology Facilities Council
UHV	Ultra High Vacuum
UV	Ultraviolet
WP	Work Package

List of Variables

Term	Unit	Description
A	m^2	area
a		slope of η's decay over the photon dose
α	$\mathrm{m}^3/(\mathrm{s\,m})$	distributed pumping
B	T	magnetic flux density (magnetic field)
b		slope η's growth over the ε_c
$\beta_{x,y}$	m	beta functions
C		constant of dependence of η on ε_c
c	m/s	speed of light
D	photons/m	photon dose
d	m	flow channel diameter
E	eV	beam energy
e	C	electron charge
ε_c	eV	critical energy
$\varepsilon_{c\,eq}$	eV	equivalent critical energy
ϵ_n	m	transverse normalized emittance
η_e	molecules/electron	electron molecular desorption yield
η_i	molecules/ion	ion molecular desorption yield
η_{ph}	molecules/photon	photon molecular desorption yield
η'_e	molecules/electron	secondary electron molecular desorption yield
η'_i	molecules/ion	secondary ion molecular desorption yield
η'_{ph}	molecules/photon	secondary photon molecular desorption yield
f	Hz	frequency
$\dot{\Gamma}_e$	electrons/s	electron impingement rate
$\dot{\Gamma}_{ph}$	photons/s	photon flux
γ		Lorentz factor
h	m	beam screen half height
I	A	particle beam current
I_c	A	critical current
j		studied gas species
$K_{\eta_{ph}}$		equivalence coefficient of η_{ph,H_2} into $\eta_{ph,H_2\,eq}$
Kn		Knudsen's number
k		second term to represent a studied gas species
k_a		fraction of scattered power absorbed by the cold mass

k_b		fraction of protons not resulting in energy deposition
$\bar{l}$	m	mean free path
L	m	longitudinal length of the structure
λ	m	wavelength
M	kg/mol	molar mass
m_0	kg	particle mass
μ_0	H/m	vacuum permeability
N_e	electrons/s	photoelectron generation rate
n	molecules/m^3	gas density
$n_{H_2\,eq}$	molecules/m^3	H_2 equivalent gas density
ν_s		Synchrotron tune
ω	rad/s	angular frequency
P	W	power
P_n	W/m	nuclear scattering heat load
Q	molecules/s	gas load (outgassing)
q	molecules/(m^2 s)	thermal outgassing rate
R	J/(K mol)	ideal gas constant
R_a	m	average surface roughness
R_q	m	RMS surface roughness
r_e	m	classical electron radius
r_p	m	classical proton radius
ρ	Ω m	electrical resistivity
ρ_{MB}	m	dipole bending radius
S	m^3/s	pumping speed
σ_n	m^2	nuclear scattering cross section
σ_i	m^2	ionization cross section
$\sigma_{x,y,z}$	m	transverse beam sizes (x,y) and bunch length (z)
T	K	temperature
T_r	m	auto-correlation length
τ_{bg}	s	nuclear scattering beam lifetime
τ_r		roughness ratio
τ_t	s	total beam lifetime
u	m^4/s	specific conductance
Y_{ph}	electrons/photon	photoelectron yield
$Z_\perp^{RW}$	Ω/m	transverse resistive wall impedance
Z_0	Ω	free space impedance

Chapter 1

Introduction

1.1 Statement of the problem

The Future Circular Hadron Collider (FCC-hh) [1, 2] is a proposal of a 100 km long particle accelerator designed to reach an unprecedented centre-of-mass collision energy of 100 TeV, more than seven times higher than that of its predecessor, the Large Hadron Collider (LHC). Such a high energy leaps into a completely uncharted territory of physics where fundamental new physical principles may be at play, offering answers to some of the fundamental questions about the origins and evolution of the Universe, as the nature of dark matter and the origins of the matter/antimatter asymmetry.

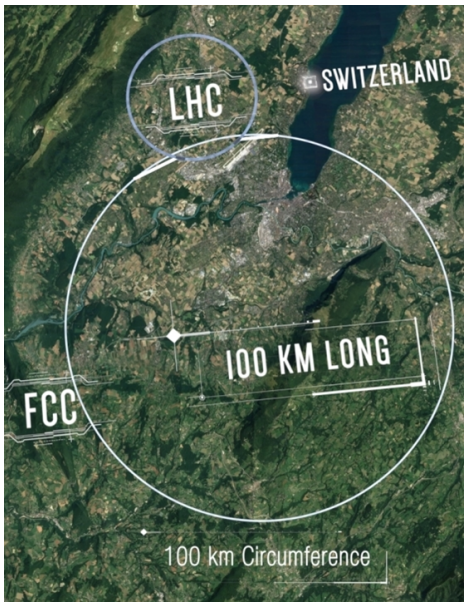

FIGURE 1.1: Comparison of the LHC's and the FCC-hh's size.

This unprecedented level of energy entails important challenges in the collider's design, such as the cryogenic beam vacuum system. To minimize the beam loss and preserve its quality, the gas density in the path of the beam has to be lower than 10^{15} molecules of $H_{2\,eq}/m^3$, ten orders of magnitude lower than that of air at sea level, with around 2.5×10^{25} molecules/m^3. The gas density in the vacuum chamber (the pipe through which the beam travels) is directly proportional to the gas generation taking place inside, following the basic equation of vacuum engineering:

$$n[molecules/m^3] = \frac{Q[molecules/s]}{S[m^3/s]} \leq 10^{15} H_{2\,eq}/m^3 \tag{1.1}$$

where n is the gas density, Q the gas load/outgassing, and S the pumping speed, term which expresses the system's capacity to evacuate the generated gas. The magnitude of Q depends, among other things, on the magnitude of the synchrotron radiation (SR) emitted by the beam, which in turn depends on the beam's energy (E) and current

(I). Due to the increase of beam energy, the SR linear power generation in the bending magnets of the FCC-hh (35.4 W/m) is around 160 times higher than in the LHC (0.22 W/m). This difference is expected to entail a much higher Q, and consequently, a much worse vacuum level.

Additionally, the high SR power makes necessary a much higher cooling capacity. As in the LHC, this is an important issue since the outer bore of the vacuum chamber and most of the magnet components are held at 1.9 K (-271.25 ^{o}C). In order to reach the stronger magnetic field required to stir the beam along its circular path (16 T), the free space available for the vacuum chamber has been considerably reduced, making difficult the implementation of larger cooling channels and reducing the gas conductance.

Therefore, even if the vacuum specifications of the FCC-hh are the same as in the LHC, 10^{15} $H_{2\ eq}/m^3$, attaining this value with nominal beam parameters is expected to be considerably more difficult.

The assessment of the feasibility of the FCC-hh from a vacuum point of view and the proposal of a vacuum chamber design capable of meeting the FCC-hh requirements are therefore two most necessary and challenging tasks in order to fully complete the FCC-hh study. Given the considerable estimated cost of the machine (more than 20000 M€ [3]) a preliminary but detailed study is necessary before moving forward with the FCC-hh.

All the phenomena taking place inside the vacuum chamber, which, owing to the beam's presence, are responsible for the gas generation and have an impact on the vacuum level, are the so-called *beam induced vacuum effects*. For the energy and temperature conditions of the FCC-hh, most of them have not been studied in depth yet. Up to date, no hadron collider with such high SR levels, comparable to low energy electron synchrotrons, has been built, so the need to study these effects has never existed before. Consequently, a lot of the data necessary to mathematically predict the behaviour of the beam induced vacuum effects and the evolution of the gas density in the FCC-hh is not present in the literature.

1.2 Objectives

The main objectives pursued in this thesis are:

- The assessment of the feasibility of the FCC-hh cryogenic beam vacuum system. To achieve this, a thorough study of the beam induced vacuum effects in the cryogenic vacuum chamber of the FCC-hh will be carried out.
- The proposal and performance evaluation of a new cryogenic beam vacuum system able to meet the FCC-hh requirements.
- Ultimately, validation of the hypotheses and calculation methodologies considered in the study, testing a series of beam screen prototypes in a dedicated experimental setup (BESTEX, from Beam Screen Test bench Experiment).

These three main objectives can be itemized in a series of secondary ones:

- Assessment of the necessary conditioning time, and its achievability, to meet the beam vacuum specifications of the FCC-hh cryogenic beam vacuum system.
- Identification of the main beam induced vacuum effects taking place in the FCC-hh and evaluation of their nature.
- Calculation of their relative weight in the total gas load.
- Estimation of the missing literature data needed to perform the vacuum level calculations.
- Calculation of the gas density limits.
- Study of the SR features and its detrimental effects in the FCC-hh.
- Calculation of the FCC-hh gas density profile, gas composition and its evolution over time.
- Assessment of the suitability of the LHC's and the initial FCC-hh beam screen for the FCC-hh conditions.
- Proposal of new BS design, featuring new solutions in order to cope with the beam induced vacuum effects.
- Identification of the work needed in collaboration with other research groups in order to successfully carry out the feasibility study.
- Calculation of the total heat load transmitted from the vacuum system to the magnet's cold mass.
- Evaluation of options to implement cryo-photon absorbers in the cryogenic beam vacuum system, and propose a conceptual design for these absorbers. They should be compatible with the accelerator magnet design and accelerator layout.
- Identification of the BESTEX lessons applicable to the theoretical calculations.
- Identification of the future work required in the FCC-hh design phase.

1.3 Work frame

This thesis has been developed in the framework of the EuroCirCol project, within the Work Package 4 (WP4) "Cryogenic Beam Vacuum System" [4], receiving funding from European Union's Horizon 2020 research and innovation programme under grant No 654305. For the specific tasks allocated to this thesis, a collaboration was arranged between ALBA Synchrotron Light Source (Spain) and the European Organization for Nuclear Research (CERN, Switzerland).

Chapter 2

Background knowledge

2.1 Context and main parameters of the FCC-hh

The discovery in 2012 of the Higgs Bosson [5, 6] at the Large Hadron Collider (LHC) finalized a fifty year long research effort aimed to develop and consolidate the Standard Model of Particle Physics. This success had a significant impact in the scientific community and, along with all the related R&D developed during this time, improved science and technology in all the world. However, there are many observations that the Standard Model cannot explain, such as the nature of dark matter, the prevalence of matter over antimatter or non-zero neutrino masses [2]. Searching for new physics, and to keep Europe at the forefront of particle physics during the 21st century, the global Future Circular Collider (FCC) study was initiated in 2013 by CERN as a direct response to the recommendation made in the Update of the European Strategy for Particle Physics. Such study explores the feasibility of different particle collider scenarios with the intention of expanding the energy and luminosity frontiers, permitting a direct observation of yet unknown particles and phenomena and providing a higher precision in the measurements of rare events.

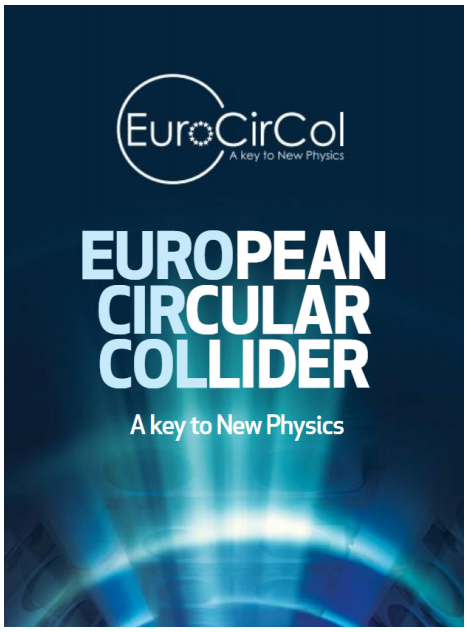

FIGURE 2.1: EuroCirCol - The European Circular Energy-Frontier Collider Study.

The most ambitious scenario of the FCC is the FCC-hh. It aims to reach a centre-of-mass collision energy of 100 TeV [1] by means of two counter rotating 50 TeV proton beams (about 8.3 GJ per beam). Such a high energy is unprecedented for particle accelerators, leaping into a completely uncharted territory of physics where fundamental new physical principles may be at play. As the LHC, it is intended to have four experimental interaction regions. Two high luminosity experiments will be located on opposite insertions, ensuring the highest luminosity and best compensation of the

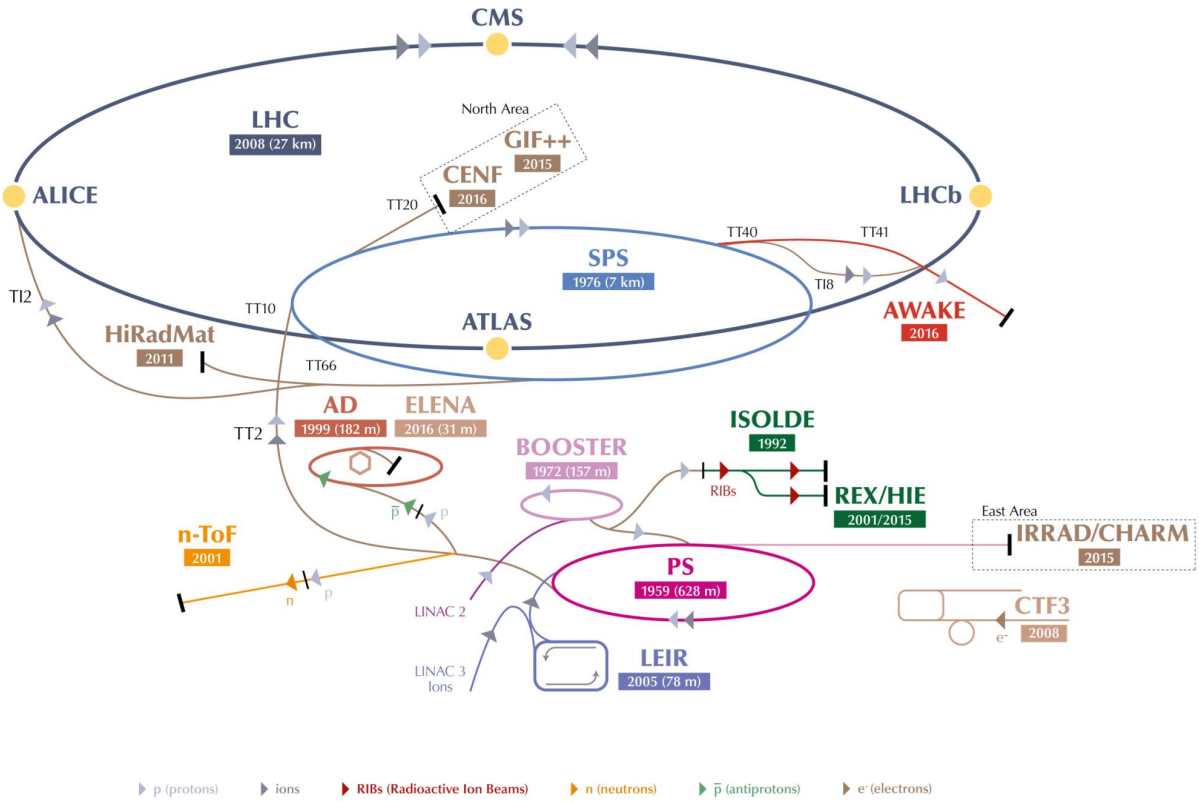

FIGURE 2.2: CERN's accelerator complex, showing the LHC injection chain and experiments [8]. The FCC-hh would be next in the chain, using the LHC as an injector.

beam-beam effects independently of the filling pattern of the beam [7], and two additional experiments of lower luminosity located together in the injection points.

The FCC-hh would be built at CERN (Meyrin, Switzerland) using the LHC as an injector (baseline option [9]), running at 3.3 TeV. The LHC needs in turn other accelerators as injectors, as shown in Fig. 2.2. These pre-injectors would be kept for the FCC-hh. The FCC-hh tunnel would pass through Switzerland and France (see Fig. 1.1), lying underground at an average depth of 300 m. In the best case scenario, and without prior implementation of an electron collider (FCC-ee) [10] in the new tunnel, the FCC-hh would start to be constructed by 2033 and would be operated by mid 2040s [3]. Its timeline would be similar to that of the previous colliders built at CERN (see Fig. 2.3). Currently, CERN is focused in the construction of the High Luminosity - LHC (HL-LHC) [11].

The conceptual design study name of the FCC-hh, named EuroCirCol [2, 12], was coordinated by CERN and received funding from the European Union's H2020 Framework Programme.

The FCC-hh needs to incorporate 4668 superconducting bending magnets (MB, also called dipole magnets). They are able to provide a high quality magnetic field

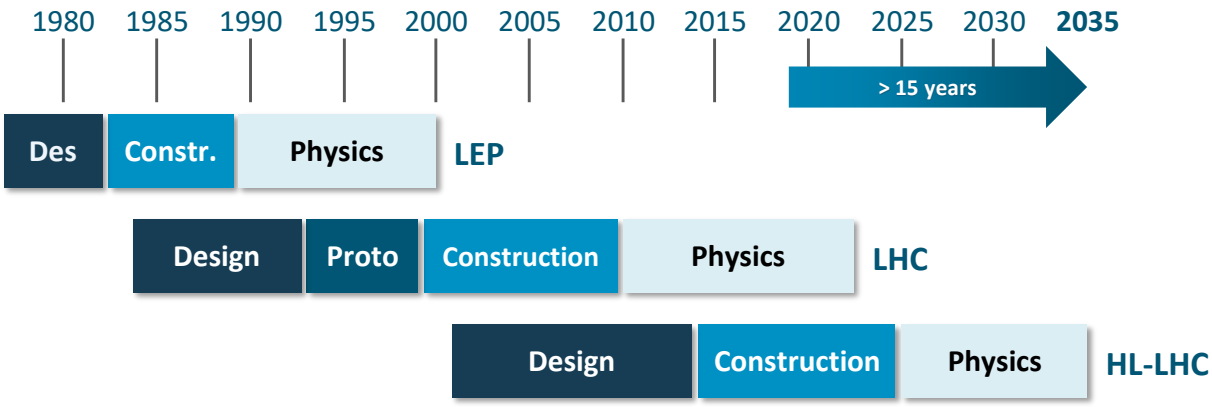

FIGURE 2.3: Timeline diagram of the previous colliders built at CERN.

of around 16 T, which, by means of the Lorentz Force, curves the trajectory of the particle beam and keeps it in a circular track. The high number of magnets result in a total machine length of around 100 km, almost four times longer than the LHC, with 27 km. A comparison of the main parameters of the two colliders is displayed in the Table 2.1.

	LHC	FCC-hh
Energy [TeV]	7	50
Current [mA]	580	500
Circumference [km]	26.7	97.75
Dipole max magnetic field [T]	8.33	15.96
Photon flux [ph/(m s)]	1×10^{17}	1.7×10^{17}
SR power [W/m arc dipole trajectory]	0.22	35.4
SR critical energy [eV]	43.8	4286.3
Magnet bore aperture [mm]	56	50
Transverse normalized emittance [µm]	3.75	2.2
Angle between dipoles [°]	0.29	0.077
Beam screen temperature [K]	5–20	40–60

TABLE 2.1: Comparison of the LHC's and the FCC-hh's relevant design parameters [1, 13, 14].

To achieve the 16 T magnetic field, two main measures have been taken. In first place, the NbTi superconducting ductile alloy used in the LHC coils (see Fig. 2.12) has been replaced by Nb_3Sn. It is considerably more expensive and difficult to manufacture, but it is able to remain in superconducting state up to a much higher magnetic flux density. However, Nb_3Sn is extremely brittle and cannot be easily drawn into a wire, contrary to NbTi. To overcome this issue, composite wires containing ductile precursors are drawn down and taken through heat treatment to become the final compound. This process rises considerably the cost of the FCC-hh superconducting magnets.

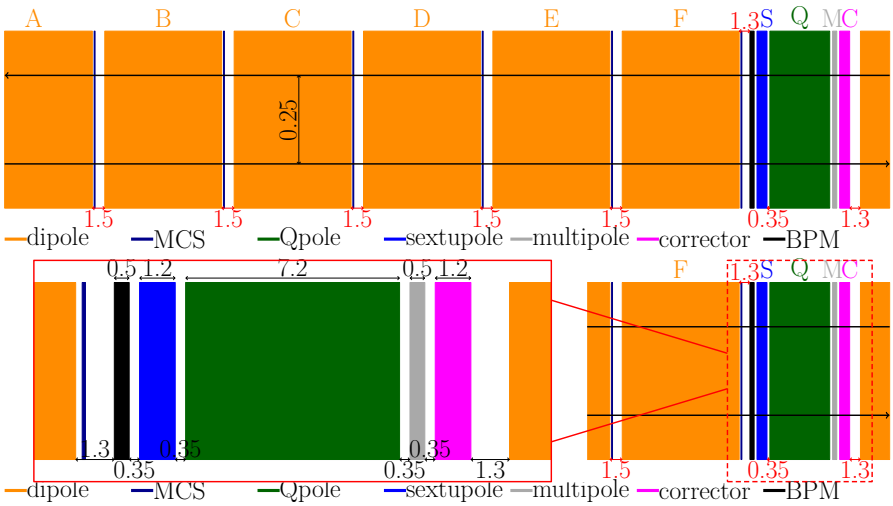

FIGURE 2.4: Layout of an arc half-cell (top) and of the SSS (bottom) [1].

Secondly, the main coil aperture, a key cost driver, has been made smaller. Now it is 50 mm, compared to the 56 mm of the LHC. Such smaller available space for the beam pipe entails a further challenge for its design.

The arcs are made of FODO cells of around 213 m, with a phase advance of 90° in both the horizontal and vertical plane [15]. Each arc cell hosts 12 cryo-dipoles and 2 SSS (short straight section). In Fig. 2.4 half of the cell is shown, including the magnetic length and separation of each element.

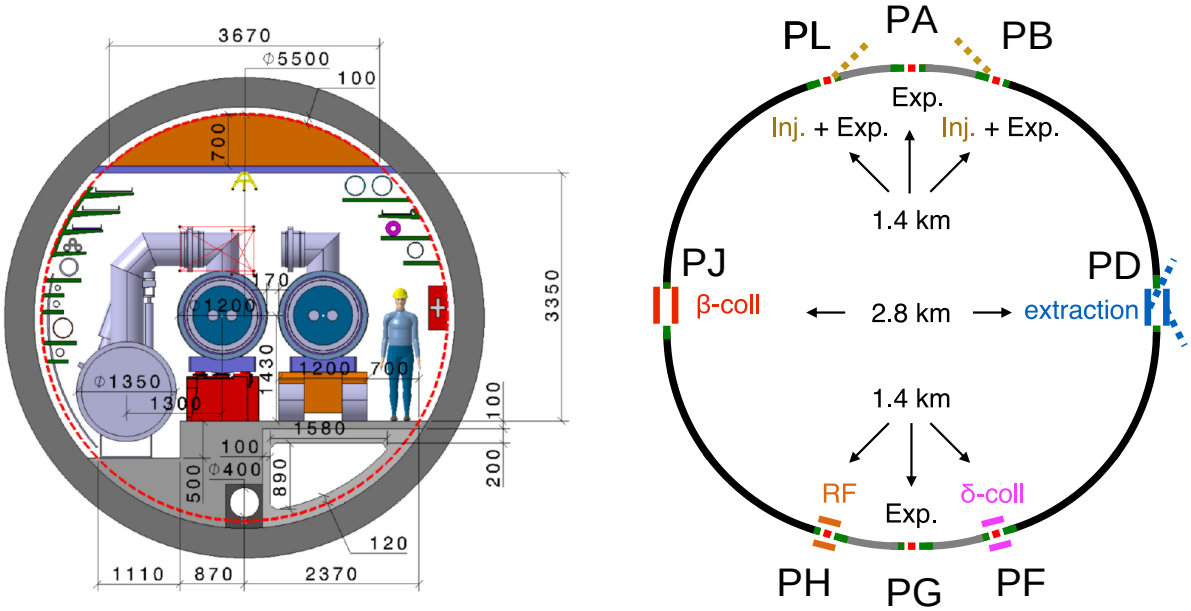

FIGURE 2.5: The FCC-hh conceptual layout (right) and an arc tunnel section (left) [1].

Each SSS, 12 m long, contains one beam position monitor (BPM), one 1.2 m long sextupole, one 7.2 m long quadrupole, one 0.5 m long multipole corrector and one

1.2 m long dipole corrector. Each dipole contains one 14.069 m long MB and one small sextupole corrector, 0.11 m long [1]. The interconnection between dipoles is 1.5 m long. Contrary to the LHC, in the FCC-hh the MB magnet yokes and beam pipes are straight. All the offset angle between MB are now absorbed by the interconnections. The angle between dipoles for the FCC-hh can be calculated as 360^o/number of MB = 360^o/4668 [16] $\approx 0.077^o$.

Figure 2.5 shows the layout of the FCC-hh and the cross section of the tunnel in an arc. The grey equipment on the left sub-figure represent cryogenic distribution line, feeding a superconducting magnet. Another magnet is shown next to it, in the transport passage. The FCC-hh hosts 4 experiments in total (as the LHC): 2 high luminosity ones, located in opposite insertions, and 2 with lower luminosity, located together with the injection systems.

2.2 Vacuum in particle accelerators

Vacuum is defined as a space totally or in a large extent devoid of matter. It is a main field of study in particle accelerators. The interaction of the accelerated beam particles with the free gas molecules present in its path (see Fig. 2.6) entails a series of detrimental effects:

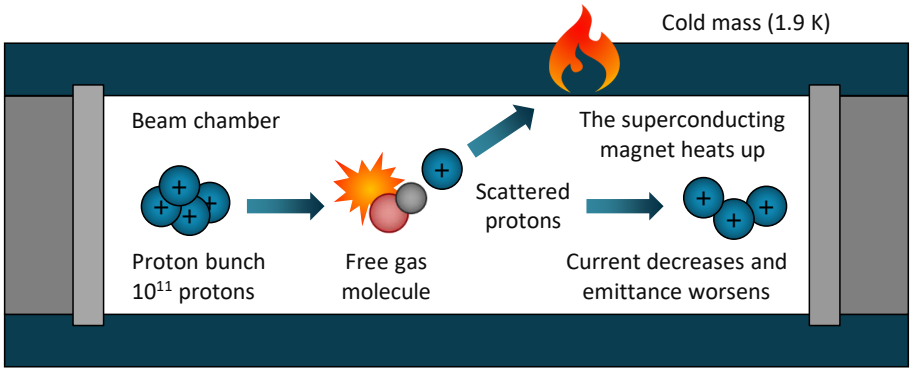

FIGURE 2.6: Representation of the nuclear scattering in the FCC-hh.

- Progressive beam current degradation.
- Progressive growth of the transverse beam size, lowering the luminosity (the beam's interaction rate, relevant for colliders) and the brilliance (the emitted photon density at a given wavelength and direction per unit of time, relevant for X-ray sources).
- Increase of the radiation dose in the accelerator elements and their surroundings.
- Increase of the detectors background.

- Increase of the thermal load on the accelerator components (relevant for superconducting colliders).

Perfect vacuum is not achievable by any means in any vacuum system. All synchrotron storage rings will always have a considerable amount of residual gas. Storage rings are usually designed to operate in Ultra High Vacuum (UHV) regime, reaching vacuum levels within 10^{13}–10^{12} molecules/m^{-3}, lower than low earth orbit (see Table 2.2). This gas density value is equivalent to around 10^{-9}–10^{-10} mbar at room temperature (RT).

Environment	Molecules /m^3
Atmosphere, sea level	2.5×10^{25}
Vacuum cleaner	2×10^{25}
Freeze dryer	10^{22}
Light bulb	10^{20}
Low earth orbit	10^{14}
Storage rings	10^{13}
Moon surface	10^{11}
Interstellar space	10^{5}

TABLE 2.2: Gas density comparison in different environments

In UHV, the free gas molecules are in molecular flow regime. Molecular flow occurs when the mean free path (the average distance travelled between successive impacts, $\bar{l}$) of the gas molecules in the chamber is larger than the diameter of the flow channel (d). The presence of molecular flow can be estimated with the Knudsen number (Kn):

$$Kn = \frac{\bar{l}}{d} \tag{2.1}$$

If $Kn >> 1$, the system can be considered to be in molecular flow. For chambers of size of the order of several cm, it means pressures well below 10^{-3} mbar. In molecular flow, intermolecular collisions have a negligible influence. The gas molecules travel around the chamber randomly, with an insignificant chance of colliding with each other. They only collide with the chamber walls. It is considered that the new direction of each molecule after a collision with the wall follows Knudsen's cosine law [17]. This law states that the probability of a gas molecule leaving the surface in a given direction within a solid angle $d\omega$ is proportional to $cos\,\theta\, d\omega$, where θ is the angle between the new direction and the surface normal [18]. The tangential and normal momentum and the energy transfer from the surface to a gas molecule in Maxwellian equilibrium can be calculated entirely from the fundamental notions of the kinetic theory of gases, where it is considered that the Maxwellian distribution function applies [19]. In UHV, the interaction between molecules is thus neglected for vacuum calculation purposes. A molecule is only considered "pumped" when it is removed permanently from the

vacuum system, independently of the pumping mechanism. This happens in the vacuum pumps. In a pump, the molecule has a defined probability of being removed from the system, either by exiting the vacuum chamber, as in turbomolecular or mechanical pumps, or by getting sticked on a surface, as in cryogenic pumps and non-evaporable getter (NEG) pumps.

All technical materials (as the chamber walls) release continuously gas into the system, with a variable rate defined here as q. The origin of the gas can be the surface contaminants, the bulk of the material (through diffusion) or the atmosphere, arriving into the system by permeation or leaks. In a short time scale the gas density (n) in a vacuum system is usually kept in equilibrium, as a balance between the total outgassing rate (the system's gas load, Q) and the gas removal (defined by the pumping speed, S) as represented with Eq. 2.2.

$$n[molecules/m^3] = \frac{Q[molecules/s]}{S[m^3/s]} \tag{2.2}$$

The most common gas species present in a vacuum system without leaks are H_2, CO, CO_2, CH_4 and H_2O. In unbaked systems at RT, the predominant gas is H_2O for low pumping times. In baked and cryogenic systems, H_2O is absent. Consequently, only H_2, CO, CO_2, CH_4 have been considered in the presented work.

Observing Eq. 2.2 it is straightforward to deduce that in order to achieve a low gas density in the storage ring of a particle accelerator, S has to be maximized whilst Q minimized. S depends mainly on the size and features of the pumps installed and on the conductance between the analysed volume and the pump.

Q depends to a large extent on the beam induced vacuum effects, which take place in dynamic mode, when the beam is present. The gas desorption caused by them depends mostly on the beam current and energy. Given the high, unprecedented energy levels of the FCC-hh, it is expected that its gas load will be highest of all the hadron colliders built up to date. Meeting the vacuum requirements is therefore expected to be a challenging task. In static mode, without beam, the residual gas density in a cryogenic system is usually orders of magnitude lower than in dynamic mode. In this mode, the only gas source is the thermal outgassing q, the static release of gas stored in the vacuum chamber walls. In baked or cryogenic systems it is mostly composed by H_2. It depends on the nature of the material, on the applied treatments and on the system's temperature.

At cryogenic temperatures, and depending on the system's pressure, some of the gas species are able to condense on the chamber walls. If a gas species is able to condense, its pressure will keep dropping until reaching its equilibrium vapour pressure (see Fig. 2.7). This principle is exploited by the cryopumps, which provide an equivalent sticking probability (also called sticking factor) to the gas molecules impacting onto them provided that their temperature is low enough. The low temperatures are also able to increase the adsorption capacity of high specific surface density materials

by many orders of magnitude.

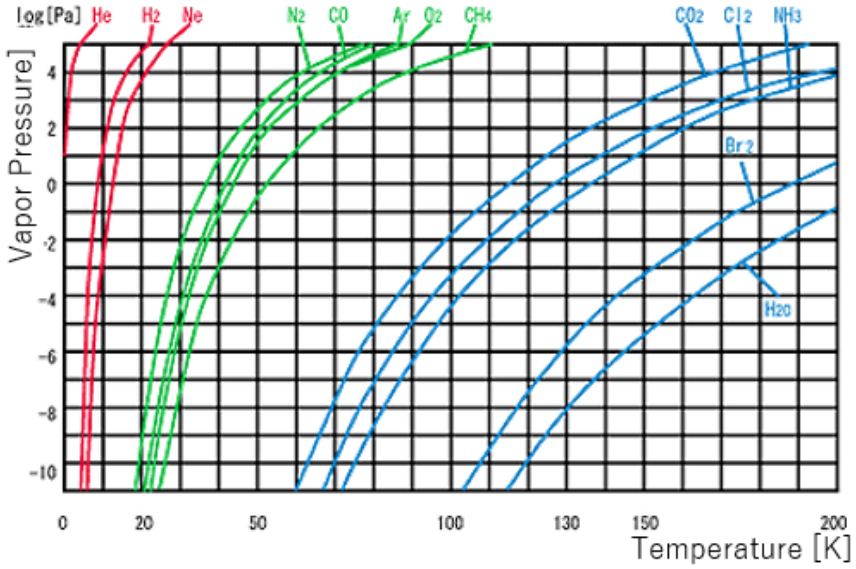

FIGURE 2.7: Vapour pressures of different gases, from [20].

As it will be explained latter, the vacuum quality in the FCC-hh is required to be good enough to provide a beam-gas lifetime of at least 100 h, corresponding to the previously mentioned gas density of 10^{15} $H_{2\,eq}/m^3$ (see Section 4.2), equivalent to 5.5×10^{-9} mbar at 40 K. Such requirements also guarantees that less than 0.2 W/m of thermal power are deposited on the magnets cold mass by the scattered protons as an average, as requested by the cryogenics specifications. The cold mass is a term which alludes to all the elements held at 1.9 K that are directly cooled by the cryogenic system, such as the CB, the coils, collars and the iron yoke. Limiting the number scattered protons deposited in the cold mass is especially relevant in the FCC-hh, owing to the high energy accumulated per beam. It is equivalent to the kinetic energy of a 415 t Airbus A380 at a speed of 720 km/h, enough to melt 12 tons of copper, or drill a 300 m long hole.

2.3 Beam induced vacuum effects

The beam induced vacuum effects studied in this document are: photon stimulated desorption (PSD), electron stimulated desorption (ESD) and ion stimulated desorption (ISD).

For each effect, all the most common gas species of cryogenic vacuum systems have been taken into account, namely H_2, CO, CO_2 and CH_4. The gas load and the resulting gas density of each effect have also been separately calculated. The partial n of each

gas (n_j) are added together according to the following expression, to obtain the H_2 equivalent gas density $n_{H_2\,eq}$:

$$n_{H_2\,eq} = \sum_j \frac{\sigma_{n,j}}{\sigma_{n,H_2}} n_j \tag{2.3}$$

where $\sigma_{n,j}$ is the nuclear scattering cross section (σ_n) of an arbitrary gas species with index j.

Expanding Q in Eq. (1.1), we obtain a representative, discrete expression to calculate n_j, accounting for all the beam induced vacuum effects:

$$n_j = \frac{Q_j}{S_j} = \frac{\overbrace{\dot{\Gamma}_{ph}\left(\eta_{ph,j} + \eta'_{ph,j}\right)}^{\text{photon-stimulated desorption}} + \overbrace{\dot{\Gamma}_e\left(\eta_{e,j} + \eta'_{e,j}\right)}^{\text{electron-stimulated desorption}} + \overbrace{\sum_k \left\{\left(\eta_{i,k,j} + \eta'_{i,k,j}\right)\sigma_{i,k}\left(I/e\right)n_j\right\}}^{\text{ion-stimulated desorption}} + \overbrace{Aq_j}^{\text{thermal outgassing}}}{S_j} \tag{2.4}$$

where S_j is the BS pumping speed of j, η_{ph} and η'_{ph} are the primary and secondary photon molecular desorption yields (with different values for each species, as the other molecular yield terms), η_e and η'_e the primary and secondary electron molecular desorption yields, $\dot{\Gamma}_e$ the electron impingement rate, η_i and η'_i the primary and secondary ion desorption yields, σ_i the ionization cross section, the index k represents each ionized gas species impacting against the surface of the chamber, A the surface area of the studied volume and q the thermal outgassing rate. All the mentioned yields depend directly on the energy of the corresponding impinging particle.

If the sticking probability of the molecules hitting a pumping surface is the same for all gas species present in the system (this is the case of the FCC-hh cold bore, for H_2, CO, CO_2 and CH_4), S_j can be calculated with Eq. 2.5:

$$S_j = S_{H_2}\sqrt{M_{H_2}/M_j} \tag{2.5}$$

2.3.1 Photon stimulated desorption (PSD)

PSD is the main gas load source in electron synchrotrons. It is caused directly by the SR [21]. The most commonly accepted mechanism through which PSD takes place is depicted in Fig. 2.8. When the SR impacts with the chamber wall, electrons are generated through the photoelectric effect provided that the photon energy is higher than the work function of the material, 4–5 eV for the common materials used in vacuum applications.

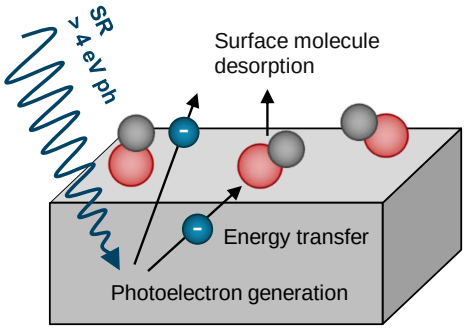

FIGURE 2.8: PSD mechanism.

These photoelectrons can interact with the contaminants or adsorbed gas present in the material surface, breaking their bonds or directly desorbing them and releasing them into the vacuum chamber. The higher the photon energy is, the higher the desorption rate. Since the nominal critical energy (ε_c) of the SR in the FCC-hh (4286.3 eV) is around 100 times higher than that of the LHC (43.8 eV) this effect will have in the FCC-hh a much higher relevance than in its predecessor. ε_c is defined as the median of the photon power distribution, i.e. 50% of the power is generated above it and 50% below.

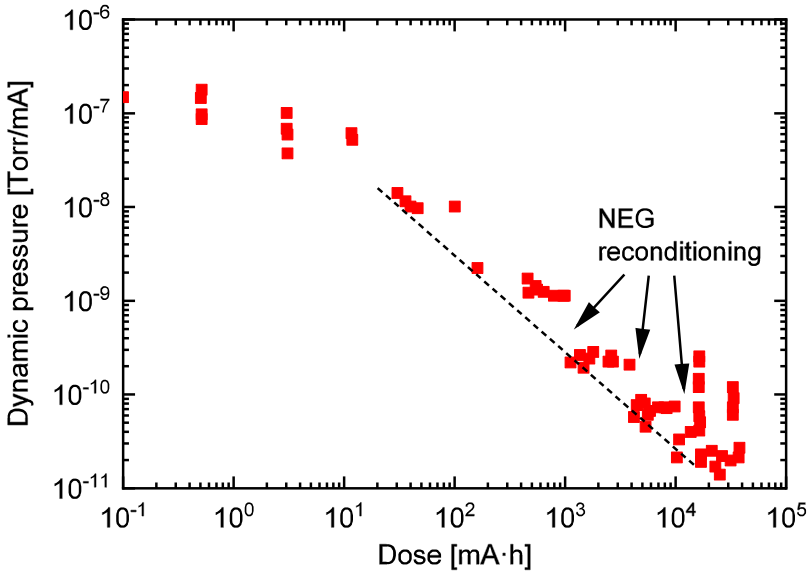

FIGURE 2.9: Specific dynamic pressure rise in LEP as a function of the beam cleaning with SR. Data taken from [22].

Besides the photon energy, the PSD molecular desorption yield (η_{ph}, expressed in molecules per photon) is highly dependent on the chosen material and the photon dose (in photon/m) received by the surface. The process when a photon dose is accumulated and η_{ph} is lowered is the so-called surface conditioning, or just conditioning. An example of conditioning is illustrated in Fig. 2.9, where it can be seen how the pressure in the chamber per unit of beam current (proportional to the number of released molecules per photon, η_{ph}) diminishes progressively over the accumulated beam dose.

A similar conditioning effect is also intrinsic to the other beam induced vacuum effects. η_e and η_i suffer from a similar decreasing trend. Most storage rings, including the LHC, need some conditioning time before achieving vacuum levels within the specifications. The FCC-hh will need it too, to a considerable extent. Furthermore, all the molecular desorption yields are strongly influenced by the temperature of the irradiated surface. Less molecules per incident photon/electron/ion are released the colder the surface is [23], provided there is no molecular condensed layer on the surface. However, a lower temperature entails a slower conditioning rate.

2.3.2 Electron stimulated desorption (ESD)

ESD is defined as the gas desorption caused by high energy electrons impinging on the vacuum chamber walls. Such electrons are part of the so-called electron cloud (e^- cloud).

The e^- cloud is a phenomenon observed in most accelerators of positively charged particles. It originates from the electrons created on the chamber walls by the SR, the electrons generated by beam loss (specially for ion beams) and the electrons generated within the beam path by the residual gas ionization [24]. These initial electrons, called seeds, are accelerated by the positive space-charge potential generated by the passage of a particle bunch and impact onto the chamber's opposite wall. Upon colliding with the wall, and providing that the secondary electron yield (SEY) is higher than 1, the incident electrons can release secondary ones with lower energy. The secondary electrons can then be accelerated towards the opposite part of the chamber by a new passing bunch, ensuring the persistence of this process and establishing a constant "cloud" of electrons inside the chamber. This phenomenon is illustrated in Fig. 2.10.

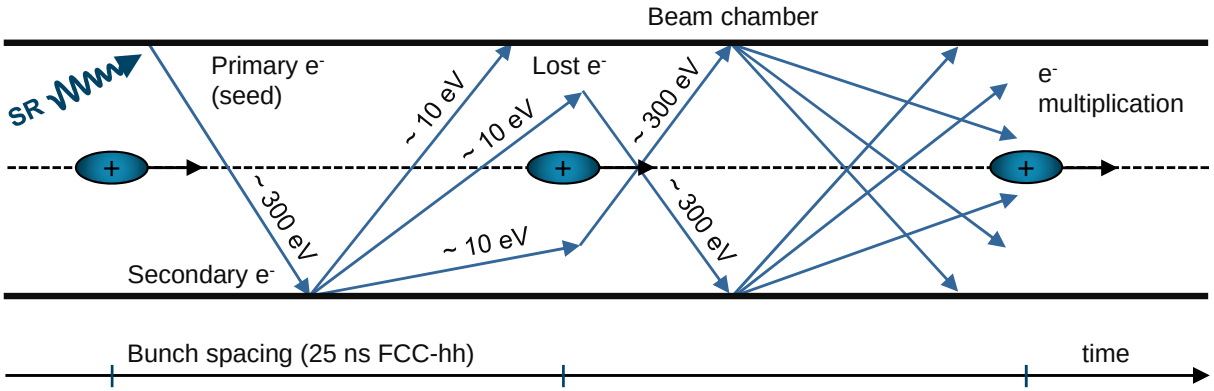

FIGURE 2.10: Formation of the e^- cloud in a particle accelerator, redrawn based on Fig. 1 in [25].

The e^- cloud build-up depends on many factors, as the SEY of the chamber surfaces, the chamber geometry, the beam charge, the photoelectron generation rate (N_e) and the bunch spacing. Among these factors, the SEY is usually the one which features the highest and fastest influence on the e^- cloud development. The e^- cloud can lead to bunch and beam current limitations if beam induced multipacting occurs. This term is defined as the phenomenon where the secondary electron emission achieves a resonance with the bunch spacing of the beam, leading to an exponential electron multiplication. It is also observed in radio frequency wave guides and amplifier vacuum tubes.

When the primary electrons impinge on the surface, not only additional electrons can be generated, but they also trigger the gas desorption in a similar manner as PSD. When the SEY of the surface is high enough, the original number of electron seeds is exponentially multiplied, and the gas load caused by ESD can achieve very high

values, even surpassing PSD. Besides the gas desorption, the interaction of the e^- cloud with the particle beam induces detrimental effects on the beam quality and stability [26], being a main concern for the machine operators.

2.3.3 Ion stimulated desorption (ISD)

When the positively charged particle beam interacts with the residual gas in its path, the gas can be ionized. The positively charged ions are then repelled towards the chamber walls, triggering gas desorption upon their collision. This process is illustrated in Fig. 2.11. The additional gas load in the chamber results in an increase of the gas density, leading to a further ionization rate. In vacuum chambers with low pumping speed and a high beam current (entailing a high ionization rate) an avalanche process may then occur, resulting in a gas density overrun and easily surpassing the limits.

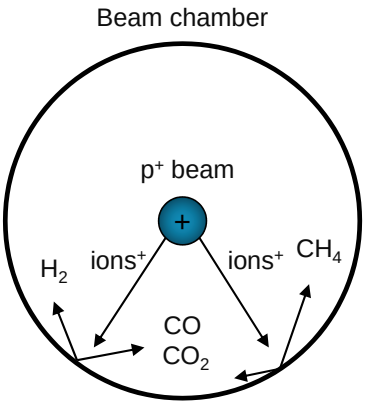

FIGURE 2.11: ISD mechanism, redrawn from Fig. 11 in [27].

Particle accelerators of positively charged particles must take into account this effect in the design phase, keeping the beam current under a threshold value (called critical current, I_c) above which the gas density overrun would happen, and keeping a high pumping speed to maximize the removal of generated gas molecules.

That being said, the critical current for the FCC-hh is computed to be much higher than the nominal one. This effect is thus considered the least dangerous one in terms of gas load contribution.

2.4 State of the art of the cryogenic beam vacuum chambers

2.4.1 The LHC cryogenic beam vacuum chamber

Being the FCC-hh meant to be the successor the LHC, it is clear that to start the development of the FCC-hh's vacuum system one should firstly analysed that of the LHC.

The LHC [28] is the world's largest particle collider, with the highest particle energy (7 TeV) and with the longest and most complex cryogenic vacuum system [13, 29]. It was installed in the 27 km underground tunnel of the Electron Positron Collider (LEP) at CERN. It contains 1232 MB, designed to reach a magnetic field of 8.33 T and a bending radius of 2.808 km.

The MB are mounted in a two-in-one configuration (see 2.12), where the two beam pipes are incorporated into a common iron yoke inside the same cryostat, cooled by superfluid He at 1.9 K. Such temperature is necessary to achieve a high current density

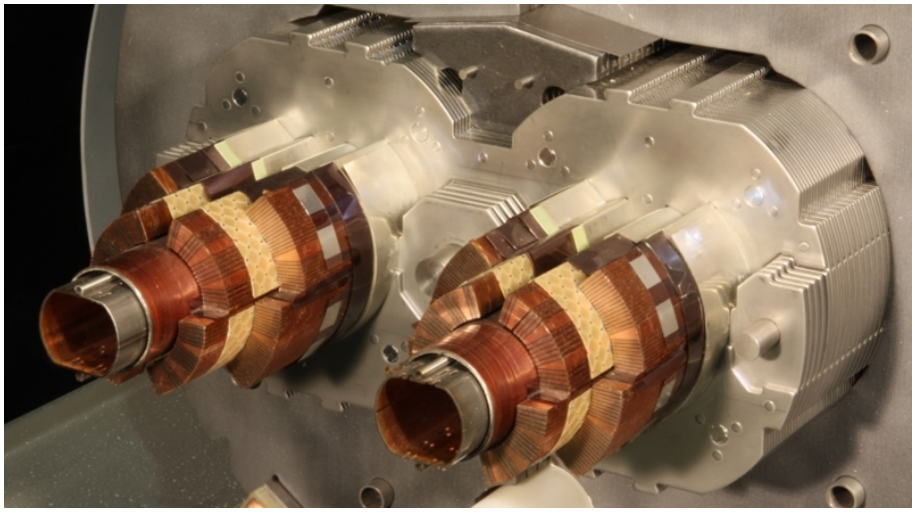

FIGURE 2.12: Cut of an LHC MB showing the two-in-one configuration. Courtesy of CERN.

in the magnet NbTi coils. Each beam pipe in the arcs is formed by two main elements, the cold bore (CB) and the beam screen (BS).

The CB separates the beam vacuum from the coils, which is surrounded by the He. The low He temperature turns the CB into an excellent cryopump, able to condense all gases except for He up to a saturated vapour pressure lower than 10^{-12} mbar. Apart from the turbomolecular pumps used for the initial atmospheric pressure pump down, there are no other means of pumping in the arcs other than the CB.

Owing to its high beam energy, the LHC was the first proton storage ring with a cryogenic vacuum system exposed to non-negligible SR levels. The SR has a ε_c of 43.8 eV and is emitted with 0.22 W/m at nominal beam parameters, 7 TeV and 580 mA.

To prevent the SR to reach the 1.9 K surfaces, in the beginning of the design phase it was proposed to install inside each CB a SR "barrier", the BS. It is operated at a higher temperature than the cold mass, at 5–20 K, achieving in this way a higher cooling efficiency. As the removal of 1 W in the 1.9 K cold mass requires nearly 1 kW of cooling power, this would result in an otherwise unaffordable size and cost of the cooling plants. Figure 2.13 shows the cross section and a close-up picture of the BS. In Fig. 2.12 the two BS can also be seen inserted inside the CB of the cryostat.

Besides of the SR interception, the BS has further purposes, as the interception of the heat load of photoelectrons and the removal of the resistive losses dissipated by the wall currents induced by the beam. In the LHC, these losses are of comparable magnitude to those of the SR [29]. Additionally, it prevents the removal of the gas condensed in the CB caused by the direct impact of high energy photons. Figure 2.13 shows a picture of the LHC BS along with a cross section diagram explaining its basic operation principle.

The BS is mainly made of 1 mm thick stainless steel (SS) P506 [31] co-laminated with a 75 µm layer of OFE copper (Cu). SS P506 has a very low magnetic permeability

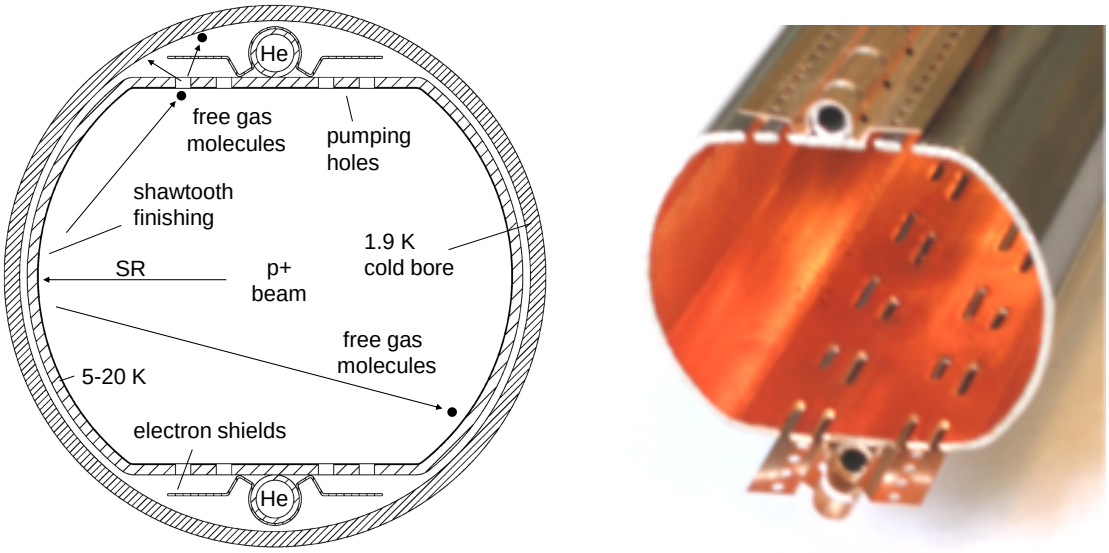

FIGURE 2.13: The LHC BS [30].

to prevent it from affecting the magnetic field quality and at the same time very good mechanical properties at low temperatures, to withstand the forces generated during a magnet quench. Since the both the electrical and thermal conductivity of SS are poor, the Cu layer is added to minimize the wall resistivity and to conduct the heat flux from the SR impact regions up to the cooling capillaries.

The BS has to be partially transparent to the gas generated inside. It must have a pumping speed high enough to achieve a low gas density (see Eq. 1.1). This is achieved by means of the pumping holes, a series of longitudinal perforations leading to the CB through which the molecules randomly pass. As the SR is generated in the horizontal plane, tangentially to the beam's direction, they are placed at the top and bottom of the BS. The pumping holes cause disturbances in the profile continuity of the BS, yielding a certain impedance to the beam's pass. In order to prevent a synchronous build-up, these perforations have a certain degree of randomization in their dimensions, as it can be observed in Fig. 2.13.

2 mm behind the pumping holes, a thin perforated Cu electron baffle is placed. This element stops the e^- cloud electrons which spiral back and forth around the magnetic field lines until eventually passing through the pumping holes. The absence of the electron baffle would entail a large amount of heat load on the CB [32]. The impact of accelerated electrons with the cold bore would also lead to the desorption of the cryo-condensed gas. The addition of this baffle decreases the original pumping speed around 30%. To relieve the loss of pumping speed, the electron baffle is longitudinally perforated in the regions where the electrons cannot impact.

To avoid the scattering of the SR all over the chamber, the region of the inner Cu layer where the SR impacts has a key feature, the sawtooth profile. This surface finishing is mechanically applied, in cold, using a roller with positive sawteeth. Owing to the softness of Cu, it is easily applied. The resulting engraved profile is shown in Fig.

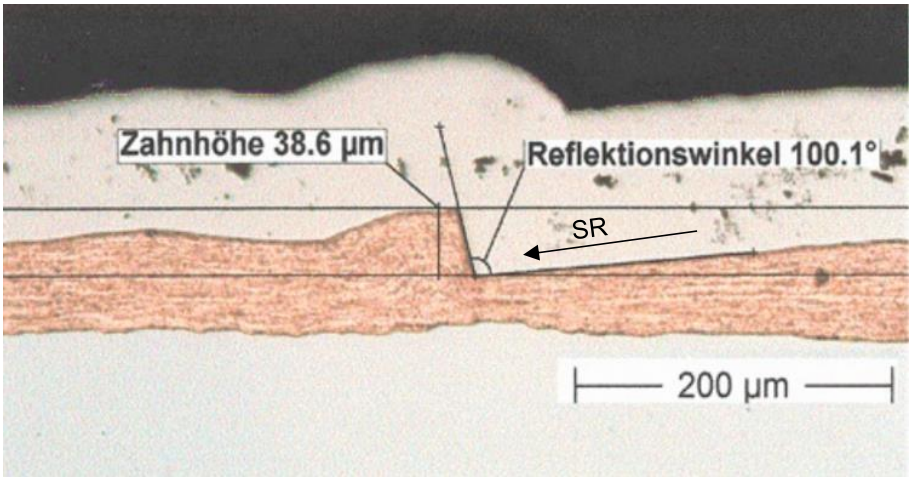

FIGURE 2.14: Cross section of the LHC sawtooth profile. The SR comes from the right, changing the original almost parallel grazing angle to an almost perpendicular one.

2.14. It can also be observed on the right picture of Fig. 2.13, on the left side of the BS inner chamber. The engraved geometry consists of a pattern of consecutive saw teeth of nominal 40 µm of height and 200 µm pitch. This pattern is aligned in a way that the SR impacts almost perpendicularly with the vertical area of each tooth. Owing to the physical properties of Cu, the reflectivity of perpendicular impacts is much lower than grazing ones, enhancing in this way the absorption factor of the original Cu surface.

The gas generation inside the LHC BS is caused for more than the 90% by ESD. This is due to, on one hand, to the low PSD taking place, and on the other one, due to the lack of advanced SEY mitigation, which relies only on surface conditioning (see Fig. 4.45).

In general, the LHC's vacuum chamber has been a successful design. It has achieved excellent vacuum levels, contributing to a satisfactory operation of the LHC for several years.

Figure 2.15 shows part of an arc in the tunnel of the LHC, with several MB aligned in a row. It is built underground, at an average depth of 100 m. The high radius of curvature allows one to see far into the tunnel. The MB at the forefront is represented cut, highlighting the two particle beams circulating in opposite directions through each BS. The insulation layers of the cryostat can also be observed.

2.4.2 The FCC-hh preliminary cryogenic beam vacuum chamber

As in the LHC, the magnets proposed for FCC-hh are mounted in a two-in-one configuration and cooled by superfluid He at 1.9 K. The two beam pipes, belonging to the two counter-rotating beams, are inserted in a common iron yoke, inside the same cryostat. Each beam pipe consists also of two concentric elements, the CB and the BS. The outer one, the CB, is in contact with the liquid He. The CB is similar to that of the LHC but with a 6 mm smaller diameter. Being at 1.9 K, it also acts as a cryopump,

FIGURE 2.15: Cross section representation of the LHC MB in the tunnel, where the beam screens and the high radius of curvature of the 27 km long tunnel can be observed. Courtesy of CERN.

condensing all the gas species arriving to its surface (with the exception of He) with a sticking probability of 1. The BS is mounted inside.

At a first glance, it could be naturally thought of using for the FCC-hh the same BS as in the LHC. Nevertheless, a series of reasons impede its use:

- The LHC's BS heat extraction is limited by design of the cryogenic system to 2.4 W/m per aperture [33]. The higher SR power of the FCC-hh (35.4 W/m) requires a higher cooling capacity and thus a larger cooling channel.
- The high SR power and ε_c of the FCC-hh (4286.3 eV vs 43.8 eV) result in a much larger gas load. Higher pumping speed is then needed to keep the same beam lifetime. This means that the conductance from the beam's path to the cold bore, low in the LHC BS, has to be enhanced.
- Beam impedance is a major concern in the FCC-hh. In order to meet the strict specifications, the pumping holes must be screened from the beam's sight.
- The higher BS temperature results in a higher heat transfer from the BS to the cold mass. The sliding rings of the LHC BS, which support it inside the CB, have a too

high conduction heat transfer. The design has to be adapted to keep it within the cryogenic system heat budget.

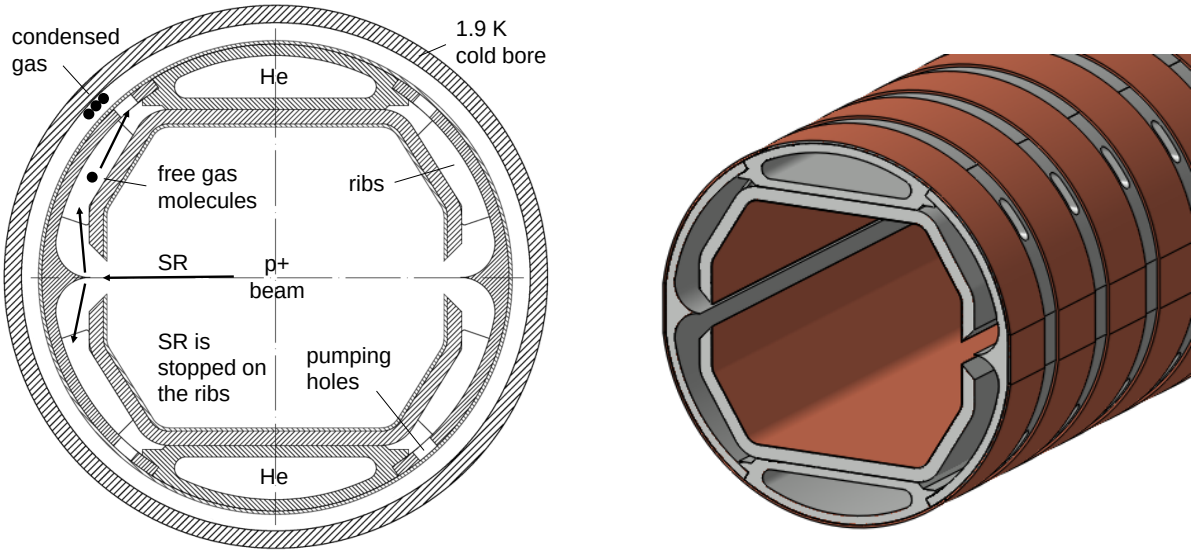

FIGURE 2.16: An old design of the FCC-hh BS. The 3D representation on the right corresponds to a slightly different version than the cross section shown on the left, which has smaller pumping holes.

By the start of this work, CERN proposed a preliminary BS for the FCC-hh [34, 35]. It is shown in Figure 2.16. It was used as a starting point to carry out this study.

Its intended strategy to handle the SR was based in the use of a sharp, highly polished SS edge (called reflector) to direct the SR out of the main chamber towards a series of stoppers, called the ribs, which were also used to guarantee mechanical stiffness during a magnet quench. Triggering the gas desorption out of the main chamber, close to the pumping holes, was expected to lower the system's gas density and to avoid creating photoelectrons in the main chamber, lowering the e^- cloud density. A photon absorber was meant to be placed in the interconnection between MB to absorb a high percentage of the reflected radiation. As it was placed out of the MB, it had the possibility to be at higher temperatures to increase the cooling efficiency.

The low angle of incidence of the SR against the wall, derived from the high MB radius, results a high SR reflection, and this design tried to take advantage of it. Other authors had previously proposed a similar strategy to handle the SR in future high energy colliders [36], taking advantage of the low grazing angle of the SR against the BS wall, but with focus in the cooling efficiency.

To cool down the reflector which receives the SR a series of Cu rings were implemented on the outer surface of the BS, due to the low thermal conductivity of SS. They were meant to be applied by cold spray [37]. The SR is emitted in only one direction, tangentially to the beam's trajectory, in a very narrow and dense cone. In this regard, only one reflector would be needed, but the impedance specifications required the BS to be symmetric, having another one on the opposite side.

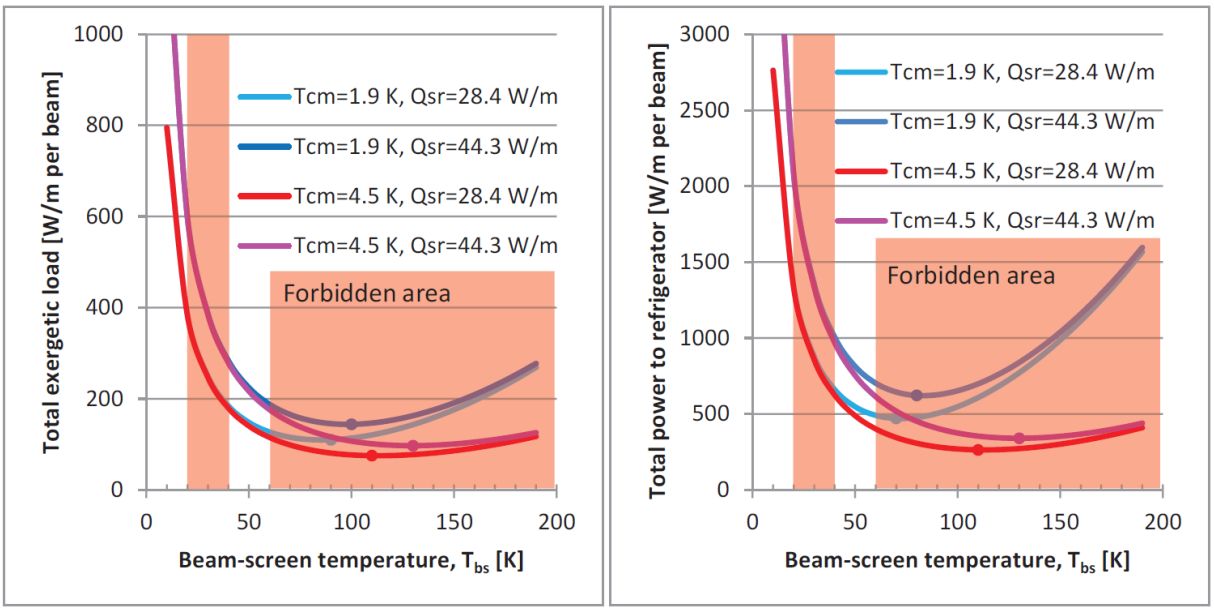

FIGURE 2.17: Exergetic load and electrical power to (real) refrigerator for BS cooling. Taken from [38].

The cooling channels, considerably larger, were placed on top and bottom of the BS, as in the LHC. The much higher values of SR power at the FCC-hh push the optimum BS temperature to a higher range, between 80–120 K (see Fig. 2.17 [38]).

However, this temperature range is forbidden by considerations of vacuum and wall impedance. In this latter case, because of its direct dependence on the temperature. At ≈ 60 K, physisorbed CO_2 with a sub-monolayer capacity would be thermally desorbed/condensed. Around 40 K, the same would happen with CO [39]. Temperature excursions around these values would result in vacuum transients, undesirable for a proper operation of the machine. The selected temperature window is the highest available, 40–60 K. The SR power emission per m of MB trajectory is 35.45 W in the FCC-hh, almost 500 W per MB and 2.4 MW per ring. In the LHC the lower SR power, 0.22 W/m and 3.6 kW per ring, allows lower BS temperatures (5–20 K). Without this higher temperature, the FCC-hh would need a cooling power of around 2.3 GW, of the order of a nuclear power plant. The vacuum stability at this range of cryogenic temperature was studied in the Task 4.4 of the WP4 [4, 40, 41].

As in the LHC, the straight sections of the FCC-hh (without MB) are held at RT. They are not cryogenic, as the arcs are. They use NEG coating [42–44] and sputter ion pumps to achieve the required vacuum level. Owing to the absence of SR, no BS is needed in the straight sections. The absence of SR, along with the use of NEG coating, results in a very low gas density, meeting easily the vacuum requirements. Therefore, the arcs remain as the main concern from the vacuum point of view.

A cryo-photon absorber (also known as SR absorber) was proposed to be inserted at the end of each MB, compatible with the accelerator magnet design and accelerator layout. The purpose of this element is to intercept much of the upstream reflected

SR, and project a shadow downstream which can protect the MB-MB interconnection elements from a direct irradiation. Even if just 1 W touches the non-actively cooled interconnection elements, it could be very detrimental for them.

The e^- cloud problem, the most detrimental beam induced vacuum effect in the LHC, is addressed in the FCC-hh BS. To mitigate this effect, several strategies have been considered. The most relevant strategy is the reduction of the SEY, given that it is the parameter which influences the most the e^- cloud development.

OFE copper has a relatively low SEY after conditioning for the range of electron energies present in the vacuum chamber. Akin to the PSD, electron dose is accumulated on the surface, changing its chemistry and progressively decreasing its SEY. This was the strategy adopted in the LHC. Nevertheless, besides of extending the commissioning time, this strategy can only lower the SEY up to a certain point.

In the FCC-hh it has been proposed to coat with a low SEY coating the BS regions where this effect is developed. Two options were considered in the beginning, amorphous carbon (a-C) [45, 46] and Laser Ablation Surface Engineering (LASE) [47–49].

Another difference between the LHC and the FCC-hh BS is that in the LHC, the BS was bent to follow the trajectory of the beam (as in common synchrotrons), which is curved in order to follow the curved iron yoke of the MB. In the FCC-hh the MB yoke is straight, because of its extremely large radius of curvature which limits the sagitta of the orbit. Therefore, the BS is straight.

As it will be explained later on, the initial design of the presented preliminary FCC-hh BS was discarded after a thorough analysis in favour of a more effective and simpler design, which became the baseline.

Chapter 3

Methodology

3.1 Strategy

As stated in Section 1.2, the main objectives of this thesis are the feasibility assessment of the FCC-hh vacuum system and the proposal of improvements in the chamber design in order to cope with the severe beam induced vacuum effects. To this end, a series of steps were taken:

1. First, to know the constraints of the work environment, a study of the relevant FCC-hh parameters and machine specifications was done. Beam parameters, SR properties, available aperture and the heat load budget of the cold mass where studied, among others. The literature on the topic was reviewed to identify the data available to be used as inputs for the calculations.

2. Lacking experimental reflectivity and photoelectron emission data of the BS candidate materials, a collaboration between CERN and LNF-INFN, led by the latter, was arranged in order to measure some samples at BESSY-II SR light source (Germany). The selected materials were SS P506, OFE copper, LASE Cu and sawtooth Cu. The reflectivity and photoelectron yield were measured for a photon energy range of 35–1800 eV and grazing angles <1°. A series of metrology measurements were also performed on the same samples at CERN and CSEM (Swiss Center for Electronics and Microtechnology), to characterize their surface.

   Since these data weren't available until later on within the project time frame, initial estimations were temporarily used.

3. The viability of the initial FCC-hh BS was assessed. After a careful evaluation, its strategy to handle the emitted SR was discarded. New SR handling strategies and consequently some major modifications in its geometry were proposed.

   Generally, all the calculations regarding SR have been done with nominal beam parameters, using a non-ideal 50 TeV, 500 mA, 25 ns bunch spacing proton beam. The β function has been set to a constant value of 355 m, the momentum offset dp/p to 0.06% and the transverse normalized emittance ϵ_n to 2.2 µm [1].

For the vacuum calculations the CB, at 1.9 K, has been set in all cases as a perfect vacuum pump with a sticking probability of 1 for all the studied gas species [50]. The interconnection areas which won't be touched directly by the SR are considered to be at 40–60 K to be conservative. It is the same temperature as the BS. In this areas a sticking probability of 0.1 has been set for CO_2, according to the data found in [51] for bare OFE copper. The rest of the studied gas species present a much lower sticking probability and have a much higher equilibrium vapor pressure for 40–60 K. To simplify the calculations no sticking probability has been set for them.

4. In the meantime, a dedicated experimental setup to test the BS prototypes (BESTEX) was being designed and built by CERN (see Section 3.4). Major support was given during the design and operation phases of BESTEX. A computer model was created from scratch to calculate the vacuum level in the setup for any given time, pump size and beam parameter. Calculations of the alignment, desired SR power, SR incidence angles, pumps selection, SR collimation parameters and system's pressure were routinely performed during all the design and operation process.

5. Lacking the most important input data to calculate the gas density in the FCC-hh, (η_{ph}), a conservative estimation was done. The validity of this estimation was latter checked at BESTEX at cryogenic temperature.

6. A long process of optimization and design of the FCC-hh BS was started. Small changes were successively applied in the design while analysing their impact in the vacuum level and checking the considered hypotheses. Many iterations were needed until converging to the final design. Owing to the different effects contributing to the total gas load in the chamber, different software tools had to be repetitively used to calculate the results in each iteration. Extensive SR tracing and vacuum simulations were performed using a built computer BS model. To speed up the simulations up to a reasonable time and increase their accuracy, a benchmark of the proposed solution to mitigate the SR in the BS was performed using the metrology and experimental reflectivity data. It was included in the computer model.

   During this step, the nature and origin of the contributions of each effect, and the influence of the BS geometry on them, were understood.

   The FCC-hh complete arc lattice was taken into account in the study. Nevertheless, only the most irradiated MBs and their interconnections were taken into account when carrying out the BS optimization. The chosen geometry represents most of the arc length and virtually all of the generated SR.

Additionally, and according to the initial directives, a preliminary photon absorber was designed with the help of CERN in order to protect the MBs interconnections from an otherwise direct impact of the SR on its elements, which could be detrimental for the RF contact fingers and the BPM buttons.

7. While the design process was being carried out, several teams in the FCC-hh study were simultaneously performing studies to assess its general feasibility. The thermal behaviour of the BS, the mechanical stability, the proton scattering, the electron density in the main chamber and the BS impedance were analysed, among others. As part of the work related to this thesis, a significant amount of effort was put into the coordination of some of these external calculations, essential to fully validate the BS design. The results of the BS temperature calculations and the electron impingement rate on the BS were used as inputs for the gas density calculations.

8. With the final BS geometry, the (η_{ph}) estimations and the photoelectron experimental data a thorough vacuum study was done. PSD, ESD and ISD were separately studied. Their partial gas loads and evolution over time were calculated. The gas density of the four most common gas species in UHV, namely H_2, CO, CO_2 and CH_4 were separately calculated and added together as H_2 equivalent units.

   The conditioning time to reach the vacuum specifications was then calculated and its feasibility assessed.

9. Three different BS prototypes were manufactured and tested at BESTEX by CERN. These prototypes had different features in order to assess their respective performances. PSD, photon reflectivity, SR heat load and photoelectron generation were explored by the WP4 members assigned to the setup operation. The experimental results of the gas density were then used, on one hand, to compare them with the performed estimations, and on the other hand to validate some of the hypotheses considered in the BS design, a most needed step. The good match between the experimental and calculated data was used to validate the calculation methodologies.

3.2 Design hypotheses

A series of hypotheses were considered in the chamber design and vacuum level calculations. Most of them were validated in the course of the study, either with specific simulations, or experimentally at BESTEX:

- The SR absorption maximization is a more efficient strategy than the reflection maximization when dealing with SR in UHV. This is ascribed to three reasons: (i)

concentrating the SR on clean areas, with a high photon dose, lowers the system's average η_{ph}. In other words, distributing the SR over a wider area lowers the overall conditioning rate and yields higher values of η_{ph} for the same amount of time. (ii) The same applies to the photoelectron generation. Lower generation of electrons is translated into a lower ESD gas load. Moreover, in the FCC-hh's case, only the photoelectrons generated in the main chamber of the BS receive a significant kick from the beam and are multiplied. The arrival of SR to the main chamber should be thus avoided. (iii) Furthermore, increasing the absorption by means of a surface with a sawtooth relief pattern converts a grazing incidence into a perpendicular one, which is known to have a lower η_{ph}.

- Following with the previous hypothesis, a BS receiving the SR on a sawtooth surface, would consequently perform better than with a sharp reflecting edge, resulting in a much lower gas load.

- As long as the pumping holes are not directly seen by the beam, they do not increase the total impedance. In this case, the only limitation in their dimensions will be the amount of leaked SR.

- The PSD molecular desorption yield (η_{ph}) and the photoelectron yield (Y_{ph}) are thought to be directly correlated. Consequently, a material featuring low Y_{ph} values would perform well under SR irradiation. The use of LASE (which features very low Y_{ph}) as a solution to mitigate the SEY or increase the photon absorption, is expected to yield a lower PSD gas load than raw Cu and sawtooth Cu. At the same time, being the e^- cloud suppressed, ESD would also be lower.

- $\eta_{ph,H_2\,eq}$ data of many common chamber materials present in the literature have been noticed to converge towards the same value after very high photon doses, above 3×10^{23} ph/m. To estimate the missing η_{ph} data for the FCC-hh conditions, it has been assumed that they follow the same tendency.

- $\eta'_{ph,H_2\,eq}$ is thought to behave in a similar manner to $\eta_{ph,H_2\,eq}$ regarding its dependence on ε_c. Photons with energy under the material's work function that impact onto the 1.9 K surfaces are expected to trigger a negligible desorption, and only through a purely thermal mechanism. That being said, even if the $\varepsilon_{c\,eq}$ of the SR arriving to the CB is considerably low, values of $\eta'_{ph,H_2\,eq}$ belonging to a ε_c of 284 eV have been conservatively chosen as input for the calculations. No other suitable data for lower energies was found, either.

3.3 Numerical tools

This section has the purpose of listing and explaining the two main numerical tools used to carry out the SR tracing and vacuum simulations shown in this thesis. It is

relevant to do so, owing to the extensive number of simulations performed with them to iteratively design and evaluate the presented vacuum system, a core part of this work. These programs are Molflow+ and Synrad+ [52–56]. Both of them are developed by M. Ady and R. Kersevan, at CERN. Over the years, they have become a common tool in the analysis and design of the vacuum systems of particle accelerators.

3.3.1 Molflow+

Molflow+ is a Monte Carlo simulation program which allows to calculate the steady state gas density and pressure in an arbitrarily complex geometry when UHV condition is met, which is the case of the FCC-hh. The name comes from molecular flow (see Subsection 2.2.)

In Molflow+, the user can define the location and magnitude of the outgassing and pumping regions in the studied geometry. Molecules are generated from the outgassing sources and their path traced, applying Knudsen's cosine law [17] to calculate the direction of particle generation and surface rebounds. When a particle randomly arrives to a pumping facet, it may be absorbed according to the sticking factor applied on such facet. This process is shown in Fig. 3.1. After a particle is removed from the system, a new particle is generated, starting anew another tracing. The data of the molecule impacts on each facet is kept during all the simulation.

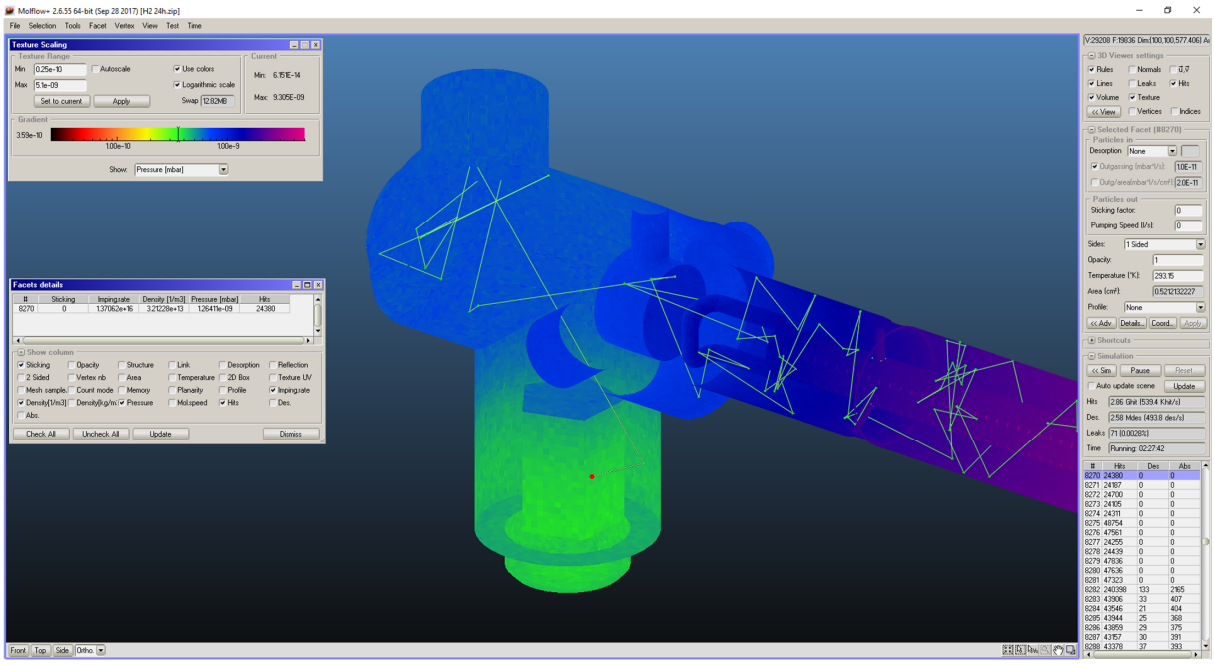

FIGURE 3.1: Example of a Molflow+ Monte Carlo simulation, showing a modelled NEXTorr pump installed in BESTEX. The trajectories of each molecule (in green) are traced until being pumped (red dot, on the pump's surface).

This process can be repeated millions of times, with the accuracy of the simulation increasing along with its running time and the number of statistics gathered. The

program then calculates the pressure and gas density on each facet according to the impact statistics. The molar mass of the traced gas molecules and the temperature of each facet in the studied geometry can also be defined by the user.

The real advantage of Moflow+ against analytical calculations resides in the complexity of the geometry able to be simulated. While classical analytical formulas rely on some basic shapes, being an almost impossible task to accurately calculate a complex system, Molflow+ is able to simulate any imported geometry (provided it has physical sense) no matter its complexity, as long as enough time and computer resources are available. When calculating the next location of a collision after a rebound, Molflow+ has to take into account all the facets of the studied geometry, so the simulation time depends directly on its amount. Thanks to the high computation power available nowadays in any standard workstation, most of the simulations achieve the desired level of accuracy within minutes.

Most of the geometries used for the calculations in this thesis have been drawn preliminary in CATIA V5 and then exported to Molflow+. In many cases, however, it has been necessary to manually draw or adjust them with the drawing tools provided by Moflow+. Molflow+ versions from 2.6.23 to 2.7.6 have been used during the development of this thesis.

3.3.2 Synrad+

Synrad+ is a photon ray tracing program. Instead of molecules, as Moflow+ does, photons are traced. Synrad+ allows the user to define magnetic regions and, within them, calculate the trajectory of particle beams. From the beams, SR photons are emitted with a representative flux and power. After impacting against a facet of the geometry, their reflection is calculated. The data carried by each impinging particle is recorded, and then used to compute the total SR power and flux over the chamber.

Two features of Synrad+ have been essential to the development of this thesis. The first one is its well implemented rough surface scattering code. As explained in [56], it is based on a model presented in [57], based on the scalar Kirchhoff theory [58, 59]. Synrad+ includes its own library of reflectivity data, created according to the methodology described in [60], using atomic scattering factors from the Henke Database [61] and using optical constants for low energies from [62]. This feature has allowed precise calculations of the SR absorption and reflection properties of the proposed BS materials and treatments. The second one, is the possibility of exporting the photon flux map on the chamber surfaces to Molflow+. After adding as in input η_{ph}, Molflow+ calculates the outgassing map and PSD gas load in the vacuum chamber, for each species. Along with the definition of the pumping areas, the resulting gas density in the system can be then calculated. An example of the gas density simulation steps is shown in Fig. 3.2, being (i) the geometry creation in a CAD software, (ii) the ray tracing simulation in Synrad+, where the photon flux map is obtained, (iii) and its exportation to Molflow+,

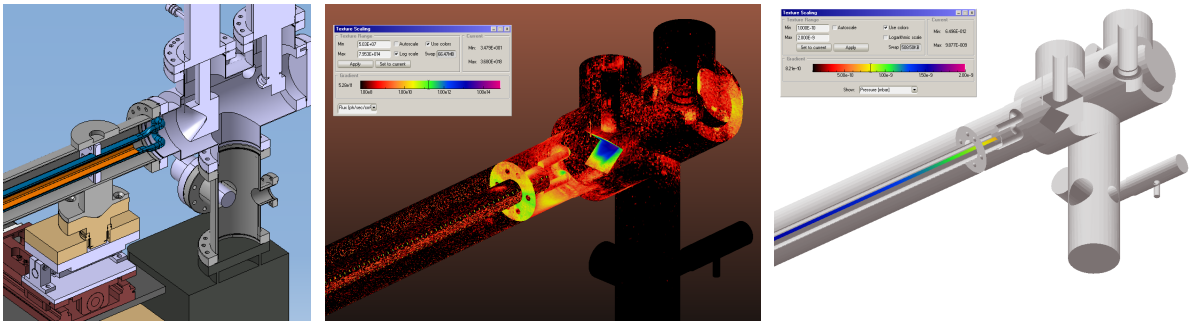

FIGURE 3.2: An example of the steps carried out to calculate the gas density in a concrete geometry.

where the gas density is calculated. In this example, the shown geometry belongs to the end chamber of BESTEX.

Both programs present the simulations results in many ways. A colour texture map can be created and the results can be visually displayed, as shown in the previous figure. The SR flux, power or spectrum arriving to each facet in the simulated geometry can also be individually calculated and read, in Synrad+'s case. The gas density, pressure, and molecular impingement rate can be read on any facet selected by the user, in Molflow+'s case, allowing one to visualize the vacuum level on any region of the system. And, it is also possible to export the data along any facet as a profile. This feature is especially useful to determine the pressure profile along the system, for instance.

Millions of photons can be emitted and traced during a normal Synrad+ simulation, increasing its accuracy along with the running time. Synrad+ versions from 1.3.14 to 1.4.25 have been used during the development of this thesis.

3.4 Experimental tools

In order to experimentally study the effects of the SR in the FCC-hh BS, and correlate them with the theoretical predictions, a Beam Screen Test Bench Experiment (BESTEX) [63–66] was designed and built by CERN in the framework of the EuroCirCol's WP4 collaboration. It was installed on the Karlsruhe Research Accelerator storage ring (KARA) at the Karlsruhe Institute for Technology (KIT) (see Figs. 3.4 and 3.3), in Germany. The acquisition of experimental data was managed by the WP4 members assigned to Task 4.6 [4, 66] with the assistance of KARA staff.

KARA was chosen because its SR spectrum, photon flux and power match reasonably well the ones foreseen for the FCC-hh, allowing a better emulation of its conditions. With the usual beam parameters, it is possible to obtain the 35.4 W/m of SR emitted by the MB in the FCC-hh. Provided that the beam energy is reduced from 2.5 GeV to 2.2 GeV, is also possible to match the 4.3 keV of ε_c. For 2.5 GeV, ε_c is around 6.2

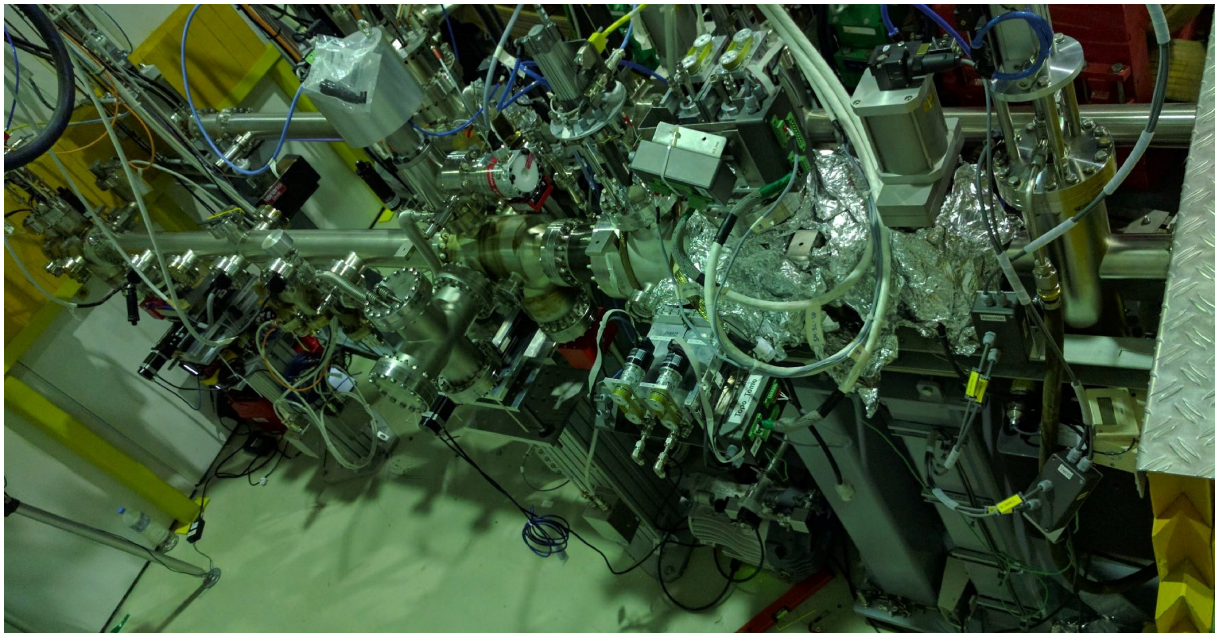

FIGURE 3.3: BESTEX set-up at KARA light source, in the foreground. The pipe in the background is an existing beamline. SR coming from the right.

keV. The main SR parameters of BESTEX and those of the FCC-hh are compared in the following Table. Note that the photon flux and SR power can be varied.

	BESTEX	FCC-hh
SR critical energy (ε_c) [keV]	6233	4286
Photon flux [p/(m s)]	4.5×10^{16}	1.7×10^{17}
Average SR power on the BS [W/m]	29	29

TABLE 3.1: Comparison of the experimental parameters of BESTEX at 2.5 GeV and the baseline ones of the FCC-hh.

BESTEX's schematic layout is shown in Fig. 3.5. The setup is an UHV system composed of two stages, the Front End and the Test Bench [63]. The Front End allows the extraction of the SR from a KARA's bending magnet into the Test Bench, allowing 180 W of maximum power and a maximum photon flux of around 5.2×10^{17} ph/s, for a 2.5 GeV and 130 mA electron beam. The Front End is equipped with a collimation stage, consisting in two pairs of slits which can be independently displaced. This permits the SR fan coming from KARA's storage ring to be cropped into a beam of rectangular footprint, enabling one to control the size, photon flux and power of the photon beam which impacts onto the inserted sample, inside the test bench.

The test bench, separated from the front end by a bellows, as the schematic shows, lays on two separated supports, equipped each one with a motorized stage. Such configuration allows an independent movement in a perpendicular direction with respect to the incoming photon beam. By orienting it properly, the walls of the studied sample

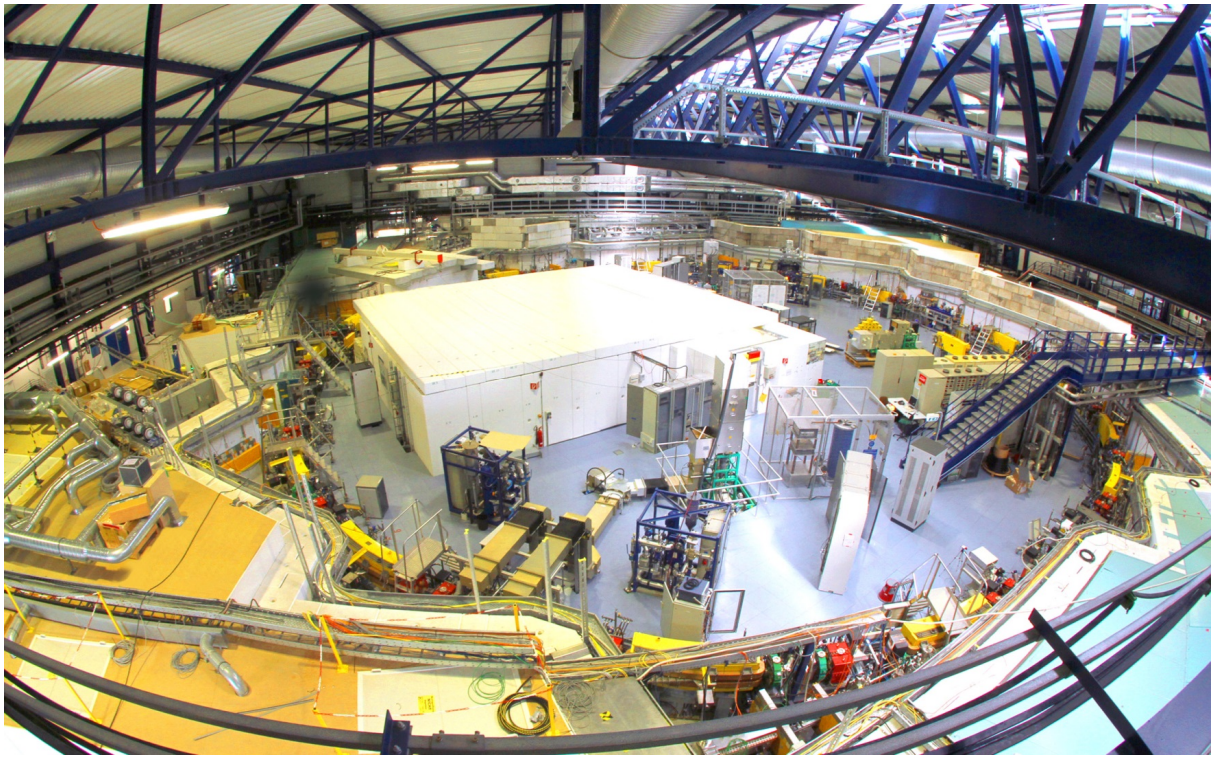

FIGURE 3.4: Storage ring of the Karlsruhe Research Accelerator (KARA) where BESTEX is installed.

can be irradiated with a user-defined glancing angle. For most of the tests, an angle of 18 mrad was chosen (being 1.8 mrad in the FCC-hh in average), achievable thanks to the long sample length.

Figure 3.6 shows a transversal cross section of BESTEX. It has been simplified for the sake of clarity, hiding some of its elements, as the cooling pipes of the sample and its supports. It depicts the sample irradiation procedure as seen from the SR origin. The SR beam is represented in green, being cropped in the slits and illuminating the inserted BS prototype with a fixed angle afterwards. In this case, the incidence angle of the SR was calculated to emulate the FCC-hh SR linear power density on the BS.

The test bench is equipped with several diagnostics, including Bayard-Alpert ionization gauges (BAG), a Residual Gas Analyser (RGA), a Pirani gauge, several PT100 temperature sensors located along the sample under study, an end copper photon cup connected to an electrode, and two fluorescent screens (before and after the sample) with the latter including a video camera to visualize the SR imprint through a view port. To increase the accuracy of the readings, the static pressure has to be kept as low as possible. To this end, the setup is equipped with two NEXTorr 2000 l/s NEG - ion pumps, placed at both extremes of the sample holder (see Fig. 3.5).

Initially, an existing setup, COLDEX [68, 69], was planned to be used instead of BESTEX. In the end, unfortunately, COLDEX was decided to be allocated to the HL-LHC project. Due to the unexpected allocation of time to the design and construction of BESTEX, the little remaining time only allowed tests at room temperature.

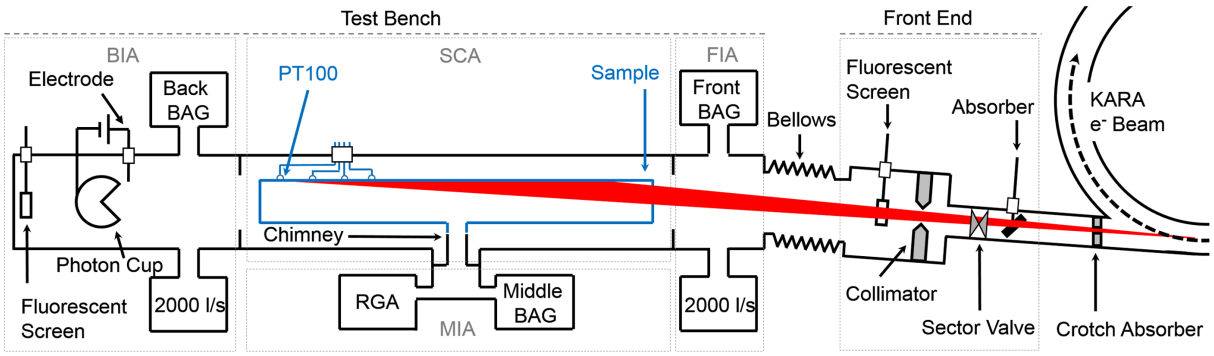

FIGURE 3.5: Schematic layout of BESTEX, from [67].

With the mentioned equipment, BESTEX is able to perform a series of studies on the inserted tubular, non leak-tight samples:

- **PSD performance:** This the main and most important functionality. With the readings of the BAG and the RGA, values of mbar/mA of each gas can be determined for each sample and compared, therefore assessing their vacuum suitability. The SS sharp reflecting edge, the LHC sawtooth and LASE were evaluated. The η_{ph}, in molecules per incident photon, can be calculated from the pressure readings. Since the BS and the SR spectrum in the experiment are intended to be as close as possible to the reality, it could be thought at first glance to directly correlate the pressure reading in the experiment with the one attributed to PSD in the FCC-hh. Nevertheless, since the pumping speed and temperature are different, a direct extrapolation is not possible in this case.

- **Photon reflectivity:** By means of a biased electrode placed next to the photon cup, at the end of the setup, it is possible to read the current of the photoelectrons generated on the photon cup surface, triggered by the SR reflected from the BS, placed upstream. Comparing this reading with that of a direct irradiation of the same SR beam, it is possible to estimate the reflectivity of the sample for the whole spectrum.

- **Photoelectron generation:** Similarly to the photon reflectivity, by means of an inner electrode in the BS, it is possible to estimate the number of photons arriving to the electrode area. This was measured on the second prototype, which was equipped with longitudinal copper, electrically insulated, clearing electrodes.

- **Temperature profile of the sample:** Using the readings of the PT100 temperature sensors, the temperature at different points of the sample can be plotted over time and compared with the simulated one. This measurement can be used to assess the cooling efficacy of the BS and its alignment.

The studied samples were three 2 m long FCC-hh BS prototypes, with different features and design stages [66]:

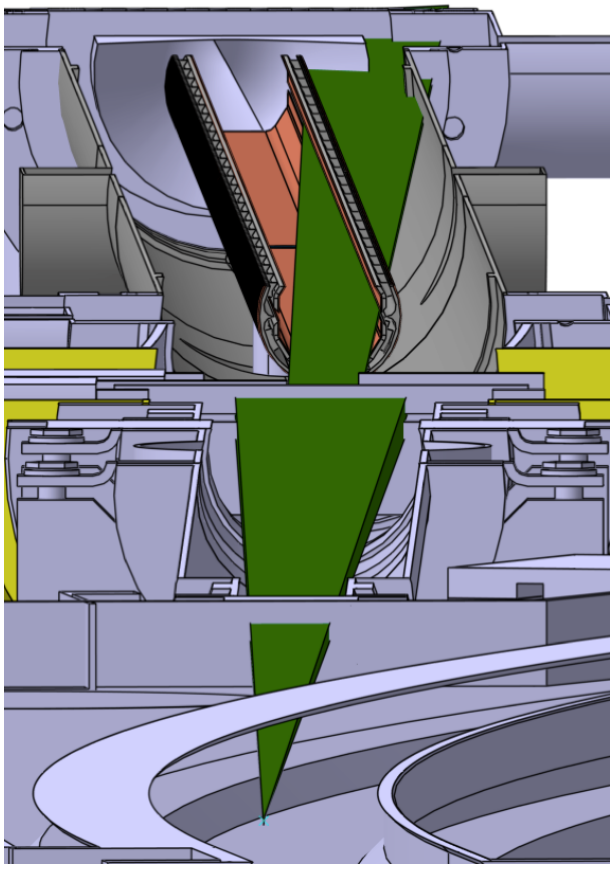

FIGURE 3.6: Simplified transversal cross section of BESTEX in KARA storage ring. The SR fan is depicted in green.

- **Prototype 1:** The initially proposed BS design (2.16), with a polished reflector. Aimed at the validation of the BS vacuum suitability, the temperature profile and the performance of the SR reflector. It was also used to validate and check any issues of the manufacturing process.

- **Prototype 2:** Similar to the prototype 1 but including two inner Cu electrodes on the BS's main chamber (see Fig. 3.7), aimed at photoelectron current measurements. These electrodes, where applied by cold spray on a ceramic layer, to be electrically isolated. The outer copper rings were lower in number and with a different layout, as well.

- **Prototype 3:** Baseline BS design. It includes a light version of LASE, larger pumping slots and Cu sawtooth profile instead of the SS reflector. The sawtooth baffle was cut from the LHC BS and welded to the other elements, so the specific variation of the sawtooth profile proposed FCC-hh sawtooth was not used. The applied LASE (see Fig. 3.7) was different than the baseline one, owing to the lack of time. It was applied with a scanning speed of 180 mm/s, leaving a pitch of 20 µm. The used laser had 50 W of power, a waveform factor of 30 and a wavelength of 1064 nm.

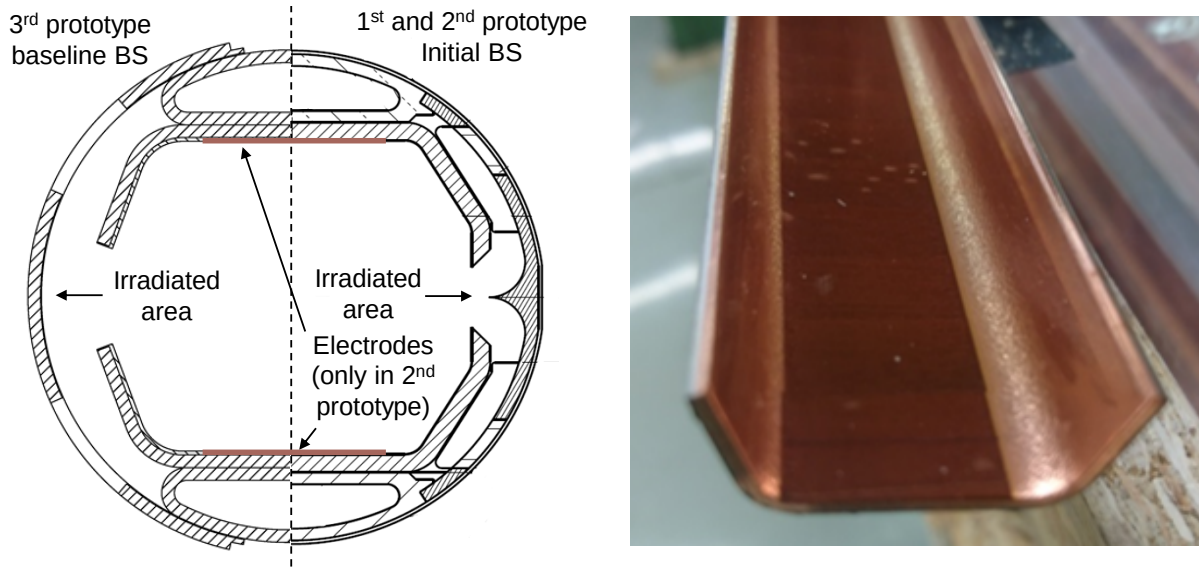

FIGURE 3.7: Profiles of the tested BS prototypes at BESTEX (left) and LASE applied on one of the primary chamber pieces of the 3rd prototype.

This prototype is aimed at the validation of the baseline design and comparison of its performance with that of the previous prototypes. In this case, not only the region designed to receive the SR was irradiated, but also the LASE ones, to evaluate the performance of this treatment. The irradiation of these areas was specially challenging because of their location, in a different axis from that of the movement provided by the motorized supports. To irradiate them, the vertical position of the sample had to be manually adjusted.

A summary of the experimental runs done during the project is presented in Table 3.2. More information about the experimental procedures can be found in [64–66].

	Prototype 1	Prototype 2	Prototype 3
BS features	Reflecting edge	Reflecting edge + cold sprayed electrode	Baseline, with sawtooth
Irradiated area	Reflecting edge	Reflecting edge	Sawtooth and LASE surface
Dates	July-Oct '17	Jan-May '18	June-Aug '18

TABLE 3.2: Summary of the experimental runs performed at BESTEX during the EuroCirCol project [66].

Chapter 4

Results and discussion

This part lists the results of the work carried out in order to fulfil the objectives listed in Section 1.2, along with their discussion. Most of these results have been already summarized during the development of this thesis in various conferences and scientific publications (see Chapter 6).

The obtained results can be divided into three major blocks:

- An initial assessment of the SR features, the initial BS and the vacuum specifications, namely, the assessment of the initial environment where the beam induced vacuum effects will take place.
- The assessment and design justification of the baseline BS.
- The study of the gas generation, the final evaluation of the machine feasibility from the vacuum point of view and the analysis of the experimental results.

4.1 Synchrotron radiation features in the FCC-hh

Since most of the beam induced vacuum effects and the BS design depend mostly on the SR, its features and impact on the vacuum system have been carefully evaluated. SR is always produced tangentially to the beam's direction (see Fig. 4.1), in the regions where the charged beam passes through a magnetic region. The particles experience Lorentz force and thus a normal acceleration, resulting in radiation emission.

In a relativistic regime, the emission pattern of the SR is sharply collimated forward. The width of such pattern is classically approximated as $2/\gamma$, where γ is the Lorentz factor. It can be derived from the following expression:

$$E = \gamma\, m_0 c^2 \tag{4.1}$$

where E is the beam energy and m_0 the rest mass of the particle.

SR emission depends on the beam energy and the magnetic field (B) intensity affecting each particle. The high beam energy (E) of the FCC-hh (50 TeV) results in unprecedentedly high levels of SR power (P), photon flux ($\dot{\Gamma}$) and critical energy (ε_c). In terms of linear power density (emitted in MB), it surpasses the LHC by a factor of around 160

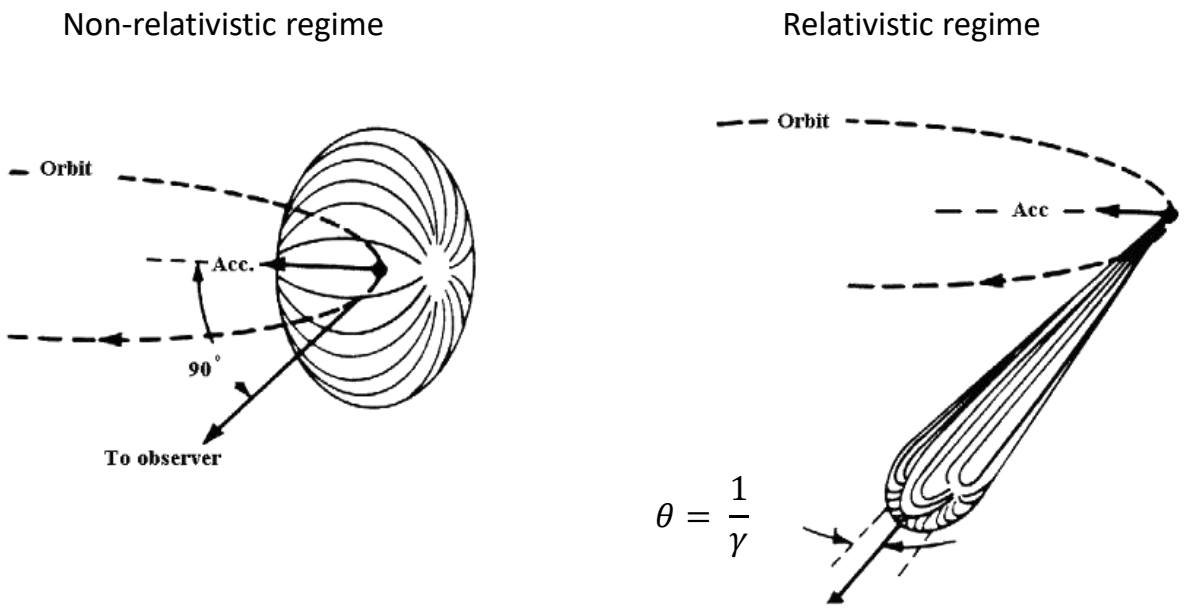

FIGURE 4.1: Qualitative radiation patterns from electrons in a circular orbit at low energy (left) and as distorted by relativistic transformation at high energy (right) [70].

at nominal beam parameters, even if the nominal beam current (I) is slightly lower. The SR emitted in the quadrupoles and other magnets has been found negligible compared with the one produced in the main dipoles. Therefore, when mentioning SR henceforward it will be related to that of MB.

The dependence of P, $\dot{\Gamma}$ and ε_c on E, I and the dipole bending radius (ρ_{MB}, around 10.45 km in the FCC and 2.8 km in the LHC) in MB is represented with Eqs. 4.2–4.4, in useful units. They have been derived from the expressions found in [71, 72]:

$$\dot{\Gamma}[ph/(m\,s)] = 7.007 \times 10^{16}\,\frac{E[TeV]}{\rho_{MB}[m]}\,I[mA] \tag{4.2}$$

$$P[W/m] = 1.239\,\frac{E^4[TeV]}{\rho^2_{MB}[m]}\,I[mA] \tag{4.3}$$

$$\varepsilon_c[eV] = 3.583 \times 10^2\,\frac{E^3[TeV]}{\rho_{MB}[m]} \tag{4.4}$$

Using Eq. 4.5,

$$B = \frac{E}{ec\rho_{MB}} \tag{4.5}$$

Equations 4.2–4.4 can be transformed to depend on the dipole B instead of ρ_{MB}. They become then Eqs. 4.6–4.8:

$$\dot{\Gamma}_{ph}\,[ph/(m\,s)] = 2.101 \times 10^{13}\;I[mA]\;B[T] \tag{4.6}$$

$$P[W/m] = 1.113 \times 10^{-7}\, E^2[TeV]\, B^2[T]\, I[mA] \tag{4.7}$$

$$\varepsilon_c\,[eV] = 1.074 \times 10^{-1}\, E^2[TeV]\, B[T] \tag{4.8}$$

As it can be observed, the dependence of P on E, is strong, since it is raised to the fourth power. $\dot{\Gamma}_{ph}$ is directly influenced by the dipole magnetic field, almost two times higher in the FCC-hh (≈16 T) than in the LHC (8.33 T).

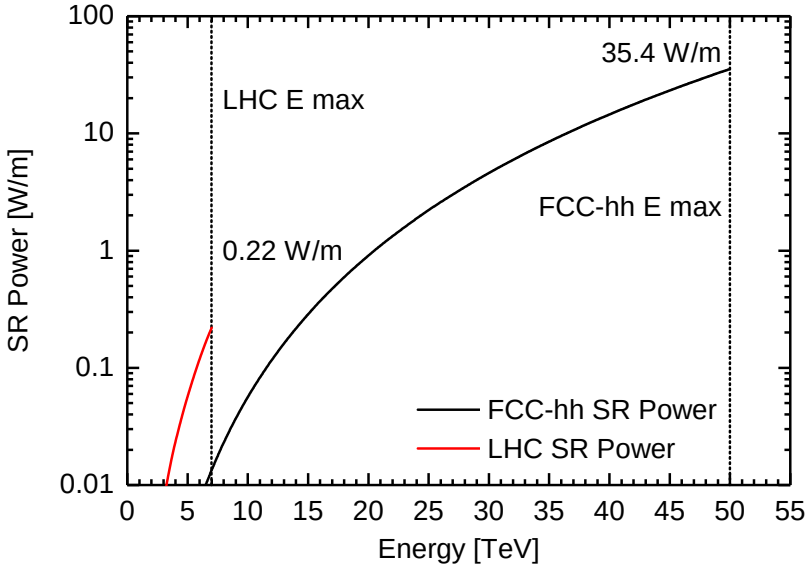

FIGURE 4.2: Comparison of the LHC and FCC-hh's SR power emitted per meter of bending magnet trajectory.

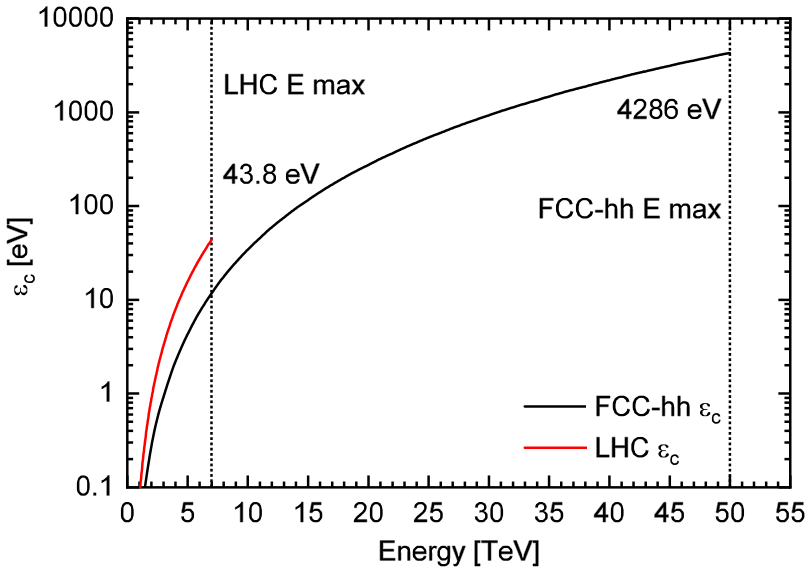

FIGURE 4.3: Comparison of the SR ε_c in the LHC and in the FCC-hh.

Equations 4.3 and 4.4 have been plotted for the LHC and the FCC-hh cases, over a range of E of 0–50 TeV. They can be seen in Figs. 4.2 and 4.3.

For the LHC range of E, 0–7 TeV the LHC surpasses the FCC-hh in both P and ε_c. Nevertheless, owing to its dependence on the beam energy, the LHC is surpassed at around 15 TeV, reaching 35.4 W/m and 4286 eV at nominal beam energy.

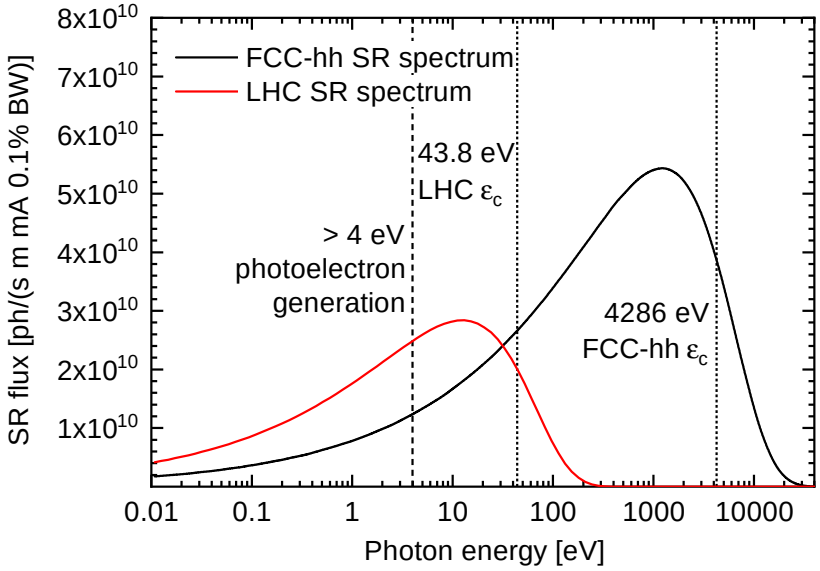

FIGURE 4.4: Comparison of the SR spectrum emitted in the FCC-hh MB vs the LHC's.

The SR spectrum for both colliders has also been calculated. They are plotted in Fig. 4.4. As it can be seen, around 95% of the total $\dot{\Gamma}$ in the LHC is generated in the infrared–UV region (1.24×10^{-3}–100 eV), and a marginal part, around 2%, in the soft X-ray region, (> 100 eV). In FCC-hh, around 66% of the photons are emitted in the soft and hard X-ray regions.

Such shift in the spectrum region entails dramatic consequences in the gas generation inside the beam vacuum chamber, and thus in the vacuum level. One of the hypotheses present in the literature which explains the mechanism of the photon stimulated desorption (PSD), states that photoelectrons are the direct source of gas generation [21, 27], as explained in Subsection 2.3.1. This hypothesis, the most commonly accepted one, has been assumed as valid for the presented work.

The photoelectron generation starts at the work function of the vacuum chamber material, 4–5 eV for metals usually employed in UHV. Photons below this energy are not expected to contribute to the gas generation inside the vacuum chamber, besides of the minimal desorption induced by thermal mechanisms. Therefore, the higher the region of the spectrum to the right of 4 eV (see Fig. 4.4), the higher the gas generation. In the LHC, at nominal beam parameters, the photon flux is 1×10^{17} ph/(m s) (see Eq. 4.2). 48 % of this amount lies above 4 eV. In the FCC-hh, the photon flux is 1.7×10^{17} ph/(m s), with the 88% of the photons being generated above 4 eV. On the assumption

that photoelectrons are the source of PSD, this entails a ≈3 times higher $\dot{\Gamma}_{ph}$ capable of increasing the gas load in the beam chamber.

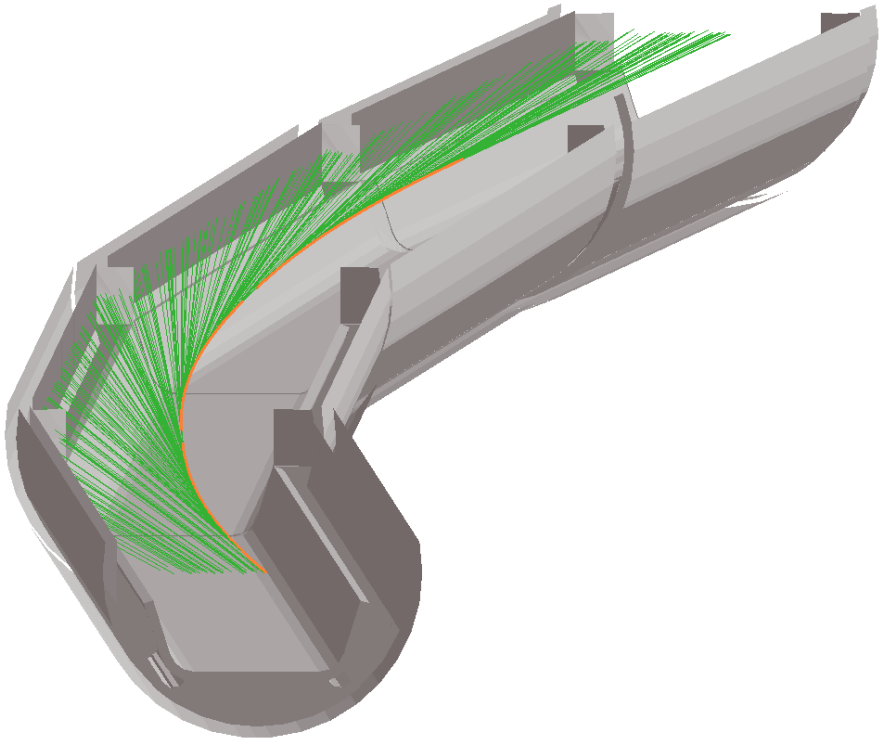

FIGURE 4.5: Representation of the SR (in green) being generated tangentially from the beam (in orange), in a sequence of three MB and one SSS. The long travel distance of the SR and the beam curvature can be noticed.

A simulation in Synrad+ of the SR generation in the arcs and its travel path is shown in Fig. 4.5. The end and initial facets of the geometry are connected, so that a photon going through the end, appears in the initial one, as if the shown geometry was periodic and infinite. It can be seen how the SR (in green) is generated tangentially from a 50 TeV proton beam (in orange) and travels a long distance before impacting onto the BS. Each green line represents a photon trajectory, with an average travel path of 21 m. The shown layout is a sequence of 3 MB BS in the arcs, with an offset angle of 0.077º, followed by a SSS BS, with half on the MB-MB angle. The magnetic length of each MB in this specific simulation is 14.242 m and B 15.78 T. The SR absorbers, in the interconnections, can also be seen, casting a shadow downstream.

4.2 FCC-hh vacuum specifications

UHV conditions are generally needed in storage rings of particle accelerators to minimize the beam-gas interaction (see Fig. 2.6). This interaction can disturb the beam, leading to its degradation by nuclear scattering and a series of detrimental effects, as

explained in Section 2.2. This beam degradation is expressed with the so-called beam lifetime, the time interval after which the beam current (I) has reached $1/e$ of its initial value (being e Euler's number). However, there are many other mechanisms in a particle collider which can degrade the beam current, such as proton-proton collisions (in the interaction points, commonly known as "beam burning"), the limited efficiency of the correction and focalization systems, the Coulomb scattering of the charged particles travelling together (including the Touschek effect) or operating errors [73]. Each process has a different lifetime value. The total beam lifetime (τ_t) can be calculated as:

$$\frac{1}{\tau_t} = \sum_n \frac{1}{\tau_n} \tag{4.9}$$

where the term n accounts for the different beam degrading mechanisms. Usually, the beam lifetime associated to beam-gas interaction (τ_{bg}) is large compared with the total one. In the LHC, while τ_{bg} is over 110 h, the total one is about 10 h [73].

The beam-gas interaction rate depends on the molecular gas density and the effective nuclear scattering cross section of such gas ($\sigma_{n,j}$), as expressed with Eq. 4.10 [74]:

$$R = \sum_j \sigma_{n,j}\, n_j \tag{4.10}$$

To quantify the residual gas remaining in a vacuum system, the gas density is reported instead of pressure when the vacuum vessels are at different temperature, as it is the FCC-hh's case. Therefore the gas density will be used henceforth to quantify the vacuum level/quality.

Using Eq. 2.3, one can express Eq. 4.10 in a more simplified way:

$$R = \sum_j \sigma_{n,j} n_j = \sigma_{H_2} \sum_j \frac{\sigma_{n,j}}{\sigma_{n,H_2}} n_j = \sigma_{n,H_2}\, n_{H_2\,eq} \tag{4.11}$$

where $n_{H_2\,eq}$ is the equivalent pure H_2 density once all the different nuclear scattering cross sections for other gas species have been taken into account. $n_{H_2\,eq}$ is a very useful term as it allows to asses with a single value the vacuum level, taking into account the impact on the beam lifetime of all the present species.

In order to establish a $n_{H_2\,eq}$ limit, the machine specifications where reviewed. Two main constraints were taken into account:

- The nuclear scattering (also known as beam-gas scattering) lifetime, τ_{bg}, which as in the LHC was requested to be higher than 100 h. The higher this value, the larger the amount of beam which can be burned in the interaction points and the more the acquired data available for research, the so-called integrated luminosity.

- The heat load on the magnets cold mass attributed to nuclear scattering (P_n). It should be lower than 0.2 W/m in average, according to the initial specifications [75].

These two constraints can be expressed with Eqs. 4.12 and 4.13, respectively:

$$\tau_{bg,H_2} = \frac{1}{\sigma_{n\,H_2}\, c\, n_{H_2\,eq}} > 100\ h \tag{4.12}$$

$$P_n = k_a\,(1-k_b)\,\frac{IE}{c\,\tau_{bg}} < 0.2\ W/m \tag{4.13}$$

$\sigma_{n\,H_2}$ (H_2's nuclear scattering cross section) is 86.4 mb, according to FLUKA [76, 77]. k_a is the fraction of the total scattered power in the arcs absorbed by the cold mass. In the latest design of the FCC-hh's vacuum chamber, k_a has been found to be ≈ 0.86 as an average in the arc cell [78]. The fraction of power deposited in the BS is only 0.05. The remaining power is deposited in the tunnel walls or escapes. k_b is defined as the fraction of protons whose interactions with the residual gas do not result in any energy deposition in the accelerator elements [79]. It has been found to be ≈ 0.042 [80].

The gas density value that fulfils both expressions (approximated by default) happens to be the same as that of the LHC, [81, 82], i.e. less than 1×10^{15} $H_{2\,eq}/m^3$. For this value, τ_{bg} results in 107.2 h and P_n in 0.178 W/m.

4.3 Assessment of the initial FCC-hh beam screen

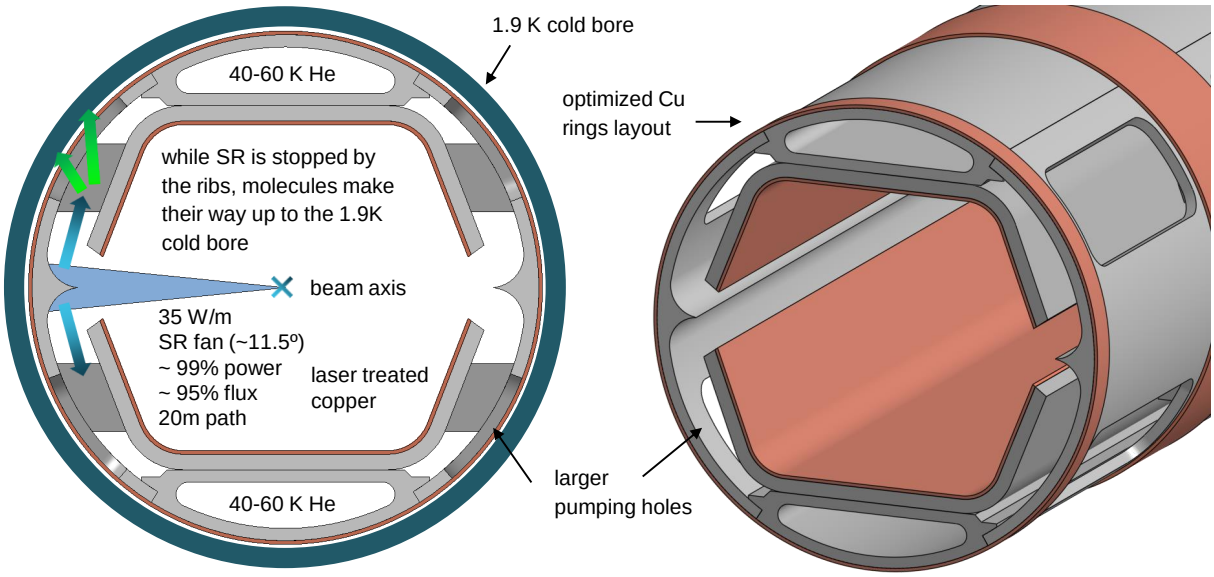

FIGURE 4.6: FCC-hh BS equipped with the sharp edge reflector, optimized from the initial design proposed by CERN (see Fig. 2.16). Presented in [83].

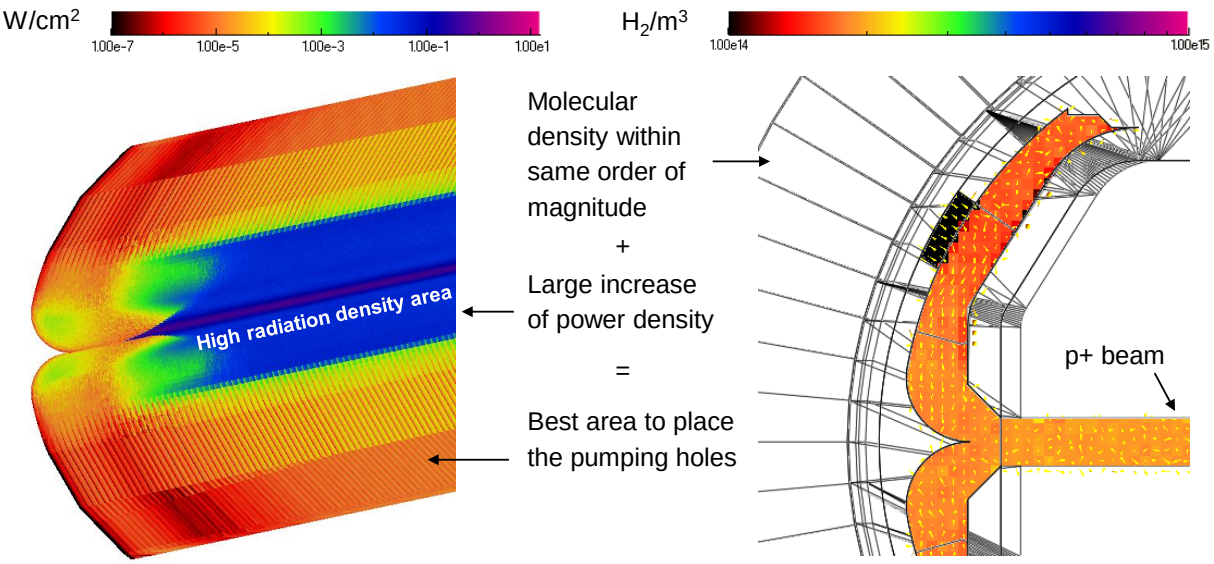

FIGURE 4.7: SR power density on the initial BS reflector (left) and gas density map on the BS cross section (right).

When starting the study of the beam induced vacuum effects in the FCC-hh, an initial BS geometry was already available [34]. After drawing the model in CATIA V5, it was exported to Synrad+ and Molflow+. Several vacuum and ray tracing simulations were carried out with it (see Fig. 4.7), in order to obtain an initial assessment of the vacuum level and to propose small modifications to optimize its design.

Many iterations were needed to optimize the initial BS design. The initial pumping speed, which was very low, was maximized, studying the pumping holes layout and the SR leakage through them. With the obtained results of the SR ray tracing, the heat load distribution in the BS was found. This information was shared with the WP4 team, who performed thermal studies on the BS geometry. With the results, the ribs were also optimized. The inner chamber sheet was kept with a straighter shape in order to allow a better fitting of the beam dynamic aperture (see Fig. 4.6).

Nevertheless, after a thorough analysis, it was realized that the initially proposed strategy was not feasible, and that the BS needed major modifications. The reasons why this decision was taken are listed next:

- **Little tolerance to beam misalignment:** According to the initial specifications, the FCC-hh BS will have to deal with a maximum beam vertical misalignment of 2 mm running with baseline parameters. Even with a much lower misalignment, the reflector does not reflect the SR as intended. When the SR beam impacts far from the sharp edge, it sees a different surface normal vector and the SR is directed towards undesired directions. In the maximum misalignment case, most of the SR beam ends on the SS edge delimiting the inner chamber (see Fig. 4.8). Such shift in the SR end area would lead to gas density increments, owing to triggering PSD on unconditioned regions.

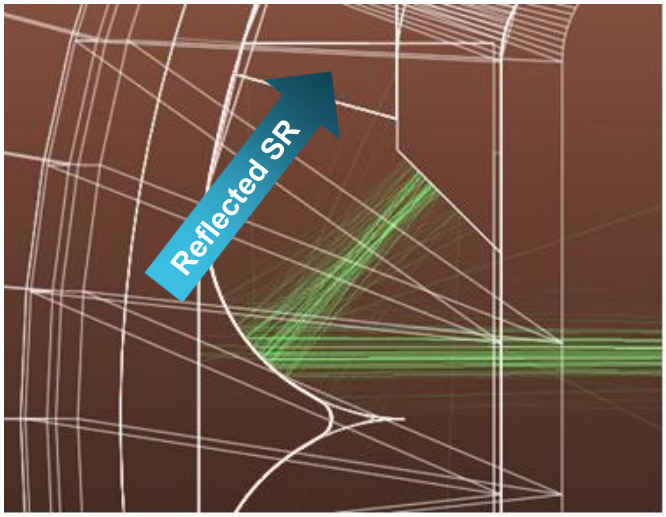

FIGURE 4.8: Detail of a ray tracing simulation showing the SR impacting on the BS sharp reflector with the 50 TeV proton beam vertically misaligned 2 mm. In this case, the SR is not reflected as intended by design.

- **Excessive gas load:** After carefully reviewing the literature and understanding the nature of the beam induced vacuum effects, it was theorized that this strategy (SR reflectivity maximization) was going to yield a much worse relative performance than its preceding one (SR absorption maximization), mainly to a much higher PSD gas load.

  To understand this, we have to take a look at the PSD mechanics. As explained in Subsection 2.3.1, it is assumed that the photoelectrons generated by the incident SR are the responsible agents transmitting the original photon energy to the molecules on the material's surface and causing gas desorption. As the photon dose accumulation (in photons/area) increases, the number of emitted molecules per incident photon (η_{ph}) decreases. The focusing of the SR incidence on small areas leads to a faster conditioning, and a lower gas load in the same amount of time than a system in which the SR incidence is distributed over a larger area. The latter is clearly the case of the BS equipped with the SS reflector. Geometrically, when the SR impinges on the sharp edge, it sees an almost-parallel surface on the very edge, distributing the SR over a wider area than if hitting the sawtooth Cu surface of the LHC BS. Even if most of the SR could be reflected, much would be absorbed, releasing significantly larger amounts of gas. Besides, the SR reflection would only widen further the SR distribution, leading to an even slower conditioning. The only advantage of the SR distribution is the minimization of the thermal stress, but in this case this is not an issue. Furthermore, it is known that grazing incidence results in higher values of η_{ph} than normal one.

  Therefore, the reflection maximization strategy is expected to entail a much larger gas load than the previous strategy, resulting in a higher beam disturbance and

longer conditioning times before meeting the vacuum requirements. Such hypothesis was checked running simulations with the different studied geometries. Some indicative results of the performances of each geometry are shown in Table 4.1. On top of that, this hypothesis was successfully validated in BESTEX by comparing the vacuum performance of the different prototypes, as explained in Subsection 4.5.1.

- **Excessive generation of e^- cloud seeds:** The intended behaviour of the SR after impacting onto the sharp reflector was to be reflected upwards and downwards, being the total photon flux of each divided beam half of the original, if it were well aligned (see Fig. 4.6). Nevertheless, even if perfectly aligned (far from being possible) this design presents one intrinsic flaw: owing to real manufacturing limits, the edge will always present a certain degree of rounding. It will never be perfectly sharp. The process used to manufacture the reflector would be extrusion, and the smallest rounding achieved by it would be around 0.3 mm [84]. Even if small, this rounding has important consequences in the SR handling. A comparison between the shape of a perfectly sharp reflector and a real one can be seen in Fig. 4.8. The SR beam is very narrow, with a Gaussian profile where the power density is highest in the middle. When hitting this rounded area, if not rectified, the photons find a normal vector which makes the reflection vector to point back to the BS inner chamber, increasing by a lot the amount of SR which goes back. The reflector has then the opposite effect of its original purpose. This effect is represented in Fig. 4.9.

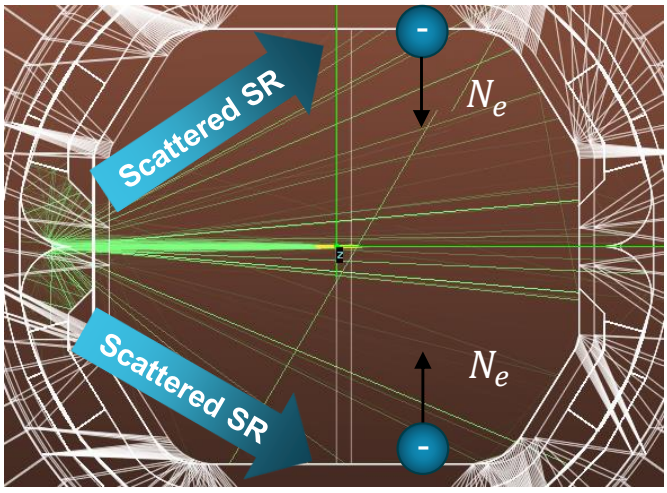

FIGURE 4.9: Detail of a ray tracing simulation showing the scattering of the SR back to the main chamber, ascribed to the rounded reflector edge.

The high number of photons reflected back to the main chamber resulted in an excessive N_e, likely to trigger transverse instabilities [85], making the design non-viable. Even if the reflector were perfectly sharp, the performed simulations show that a non-negligible amount of SR backscattering would always take place,

leading to a high N_e when the reflectivity is maximized. Table 4.1 shows a performance comparison of a BS equipped with a real, extruded reflector (with the 0.3 mm radius rounded edge), a BS with a perfectly sharp one and a BS with a perfect LHC sawtooth profile instead. As it can be seen, even if a real sawtooth surface (with intrinsic manufacturing flaws) would perform worse than the ideal one, the difference in performance is clear. Maximizing the SR on the first hit, results in less SR power arriving to the inner (main) chamber of the BS, where the e^- cloud is developed, and consequently less N_e and lower electron density. More specific data about this issue is presented later, in Tables 4.3 and 4.4, using a real sawtooth profile obtained from a benchmark with experimental data, and with specific values of N_e.

TABLE 4.1: Performance comparison of different elements hit by the SR beam, using one of the first BS versions. Gas density calculated with an arbitrary η_{ph}.

Analysed feature	Extruded reflector	Sharp reflector	Ideal Cu sawtooth
Leaked SR P to the CB	0.035	0.045	0.002
SR power on inner chamber Cu	80.1 W	3.6 W	0.18 W
SR power reflected back through central slot	20%	1%	0.01%
SR power on the ribs	25 W	91.2 W	0.0025 W
H_2 PSD gas density 36 Ah [H_2/m^3]	1.7×10^{14}	1.2×10^{14}	4.8×10^{13}
BS manufacturing complexity	Medium	High	Low

- **Excessive manufacturing costs:** The use of the SS reflector strategy entails the presence of external copper rings to enhance the heat dissipation, owing to the relatively bad heat conduction of SS. They are applied by cold spray [37], an expensive process. Additionally, according to the performed simulations [83], to achieve the optimal performance of this strategy (and, provided the beam is always well aligned with the BS axis, unlikely to happen), the reflector had to be polished as an additional manufacturing step (see Fig 4.10). Achieving a reasonably high X-ray reflectivity is challenging. Very small grazing angles (see Fig. 4.20) and very polished surfaces are needed. The manufacturing to a BS with a highly polished reflector, extended to the whole machine, and for the two beams, results in a considerable expense.

- **Excessive heat load on the CB:** The maximization of the SR reflected towards the ribs (see 4.6), even with a perfectly aligned beam and perfectly polished and sharp reflector, leads to an inevitably higher amount of SR leaked to the CB through the pumping holes. This leaked SR not only requires more cooling plants power, but can also lead to the desorption of the gas condensed on the CB (see Subsection 4.5.2), losing the theoretically higher effective pumping speed

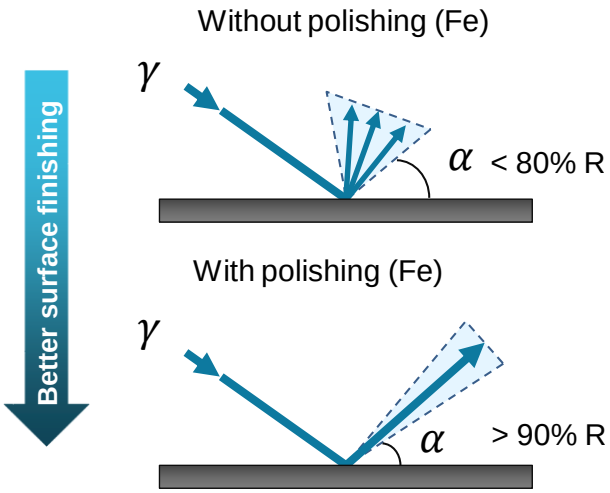

FIGURE 4.10: Comparison of the SR scattering and reflectivity of the BS reflector, depending on the surface treatment.

derived from triggering the gas desorption next to the pumping holes, far from the main chamber.

- **Excessive SR power directed to the MB-MB interconnections:** With a highly reflecting BS, a relevant amount of radiation is directed towards the MB-MB interconnections. Initially it seemed a good idea, since these areas are out of the magnet coils and the risk of a magnet quench could be reduced. Nevertheless, this creates three problems:

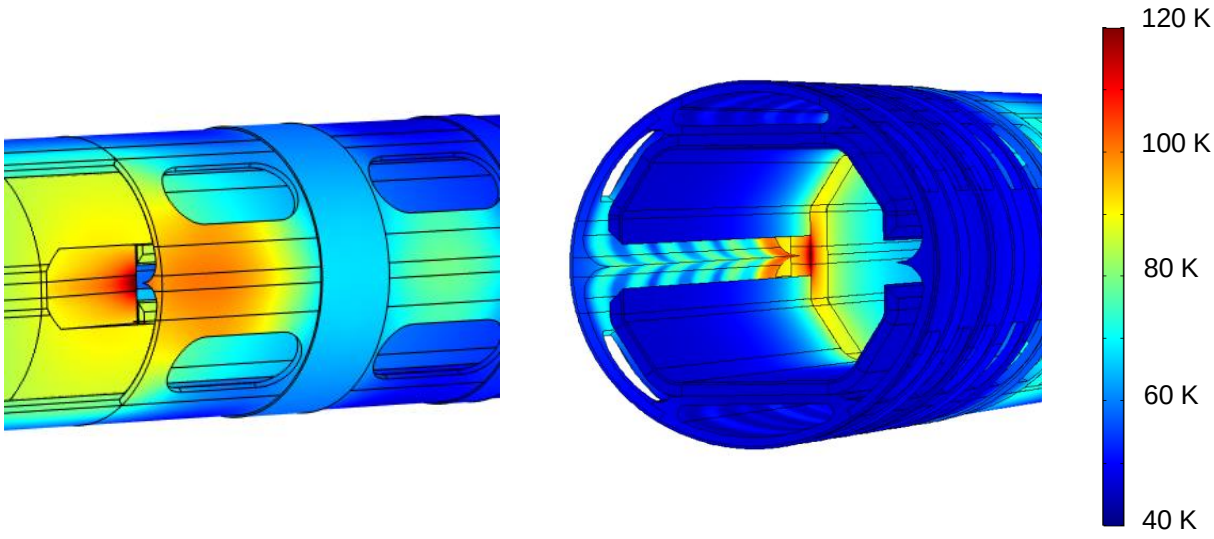

FIGURE 4.11: Thermal analysis of one of the earliest designs of the SR absorber, placed at the end of the MB, at the interconnection. Courtesy of J. Fernández.

(i) The heat load density in the SR absorber becomes too high, reaching values > 2 kW/cm^2 in pessimistic calculations, with an ideal beam and a short absorber,

leading to a high thermal stress and excessively high temperatures (see Fig. 4.11). More information about this element can be found in Subsection 4.4.2. The idea of having a dedicated cooling in this region at a higher temperature, to increase the cooling efficiency, was analysed by the cryogenics team. It was concluded that the potential savings were not worth the effort in terms of cost, since it entails a considerable amount of duplicated cooling equipment for the new line [86].

(ii) The high power in the SR absorber results in a high PSD gas load in the interconnection. The lack of 1.9 K surfaces in the interconnection makes the pumping speed to be very low in this region. The temperature has been assumed to be that of the supercritical He in this region, around 40–60 K. The sticking factor for H_2 within this range of temperatures is assumed to be zero, and lower than 0.1 for the rest of the studied gas species [51]. The high gas load added to the low pumping speed results in a high pressure peak, placing the gas density in the interconnection one order of magnitude above that of inside the magnet bore, rising considerably the average in the arcs.

(iii) The high amount of photon flux in this region leads to a dangerous value of N_e in the MB-MB interconnection. Since the e^- cloud density is proportional to N_e, as it will be later explained, the instability threshold could be easily reached, according to the initial calculations. The gas load due to ESD would be increased, as well.

Summarizing, the initially proposed BS design was finally deemed non-viable. The reflection maximization strategy, in the context of this specific problem, has no real advantage over the maximization of absorption one. On the contrary, it has many associated detrimental effects. An alternative BS design was proposed to sort out the issues of the initial one, featuring a much better performance in addition to a much cheaper manufacturing cost. It is shown in the next Section.

4.4 Design of the baseline FCC-hh cryogenic beam vacuum chamber

4.4.1 General view

As in the LHC, the cryogenic beam vacuum chamber of the FCC-hh is formed by two elements, the CB and the BS. The CB, smaller than that of the LHC, is inserted in the coils aperture, and separates the 1.9 K superfluid He surrounding the magnet coils from the vacuum in the beam chamber. The BS, at 40–60 K, is inserted inside the CB. The baseline BS for the FCC-hh is shown in Fig. 4.12, showing a drawn 2D cross section and a 3D isometric view. A fast visual comparison between the FCC-hh and the LHC BS is presented in Fig. 4.13 and also in Fig. 4.14.

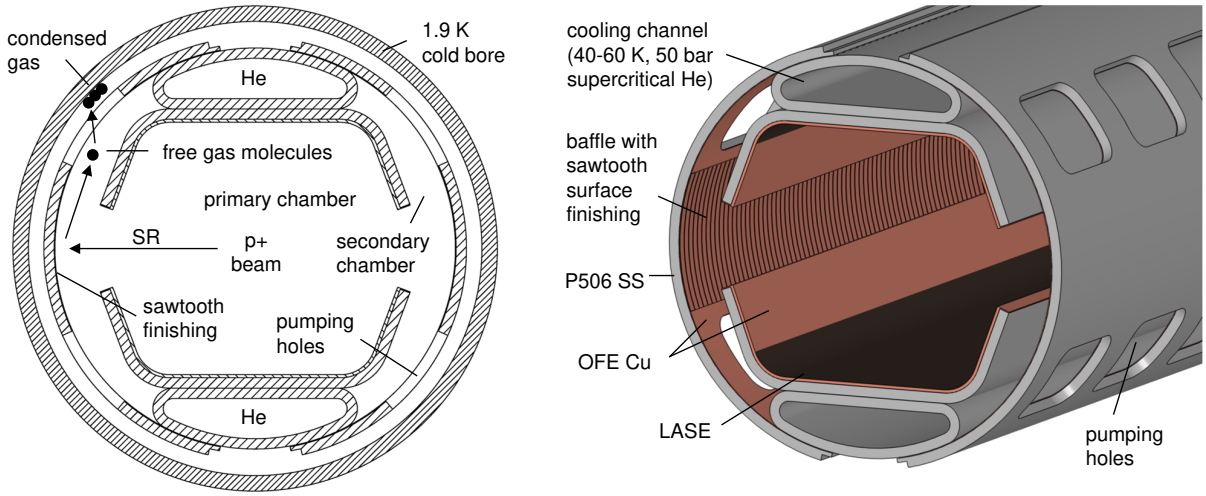

FIGURE 4.12: The FCC-hh BS. On the left, the 2D cross section. On the right, a 3D isometric view, drawn with CATIA V5. The LASE treatment layout corresponds to the MB case.

Fig. 4.14 shows a real picture of the LHC BS and the FCC-hh baseline one, mounted in BESTEX. In Fig. 4.13, the two cross section of both BS are represented at the same scale. The basic operation mechanism is also represented. To get an idea of their size, the inner diameter of the cold bore is 50 mm in the LHC and 44 mm in the FCC-hh. In the LHC BS, the SR with a ε_c of 43.8 eV is emitted from the 7 TeV proton beam and impacts against the chamber wall, in which a sawtooth surface profile has been engraved. This treatment lowers the reflectivity, so that the N_e in the chamber is reduced. The generated gas molecules arrive at the CB after randomly bouncing all over the chamber, passing through the pumping slots and through the electron shield. On the CB, they condense, and are considered removed from the system.

The FCC-hh baseline BS has a similar working mechanism. Unlike the initial BS design, the baseline is also based on the absorption maximization as a strategy to handle the SR (with a ε_c of 4286 eV) and to mitigate the detrimental effects arising from its scattering. As in the LHC, it serves several purposes. Among them, the most important one is the improvement of the cooling efficiency, owing to its high temperature. Since the removal of 1 W at 1.9 K (the cold mass temperature) requires around 1 kW of electric power, the absence of the BS would entail 2.3 GW of necessary cooling power (of the order of a nuclear power plant) only to deal with the SR power.

The baseline FCC-hh BS geometry was conceived after a long iterative design process, where its dimensions were optimized to minimize the gas density, the beam impedance, manufacturing costs and the heat leakage to the cold mass, whilst maximizing its pumping speed and mechanical stiffness (analysed by the WP4 collaboration). To minimize the gas density, besides of maximizing the S, the key has been to reduce the gas load, Q. A series of figures of merit have been identified to affect it

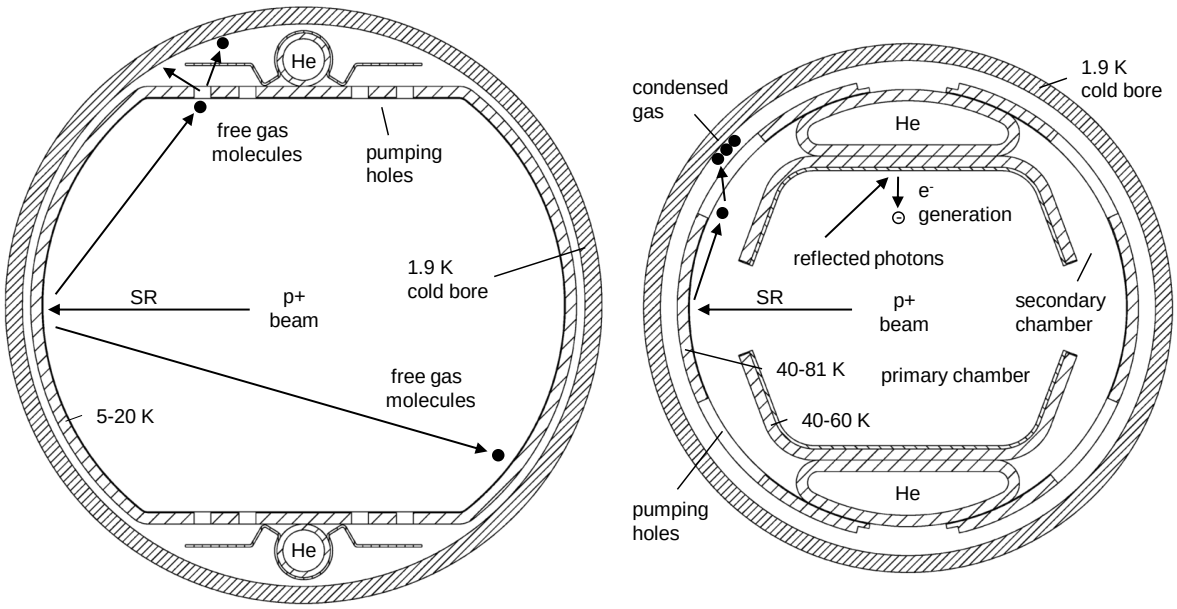

FIGURE 4.13: Comparison of the LHC BS (left), as seen in [30], and the FCC-hh's (right), with both figures being represented at the same scale [74]. The inner diameter of the cold bore is 50 mm in the LHC and 44 mm in the FCC-hh. Drawn with CATIA V5.

directly. Each iteration has tried to minimize them:

- The total area irradiated by the SR.
- The SR reflectivity.
- The SR flux arriving at the CB.
- The SR flux arriving at the inner chamber.
- The SR flux arriving at the SR absorber in the interconnection.
- The length of the magnet interconnections.
- The intrinsic η_{ph} of the irradiated materials. Most difficult to change, nevertheless.

This process was also used to understand the nature of the gas load generation, and its dependence on the design. Initially, the arc layout, represented in Fig. 2.4, was studied to narrow down the region of study. Owing to the long SR travel distance (around 21 m on average), after two MB in a row, the results are the same for the rest of them, before the SSS. Therefore, the model could be simplified studying three MB in a row, followed by the SSS. This model is represented in Figs. 4.5 and 4.15.

Fig. 4.16 shows the H_2 PSD pressure calculation for the model shown in Fig. 4.5, with three MB and SSS in a row (for an old arc cell layout). It can be seen how the

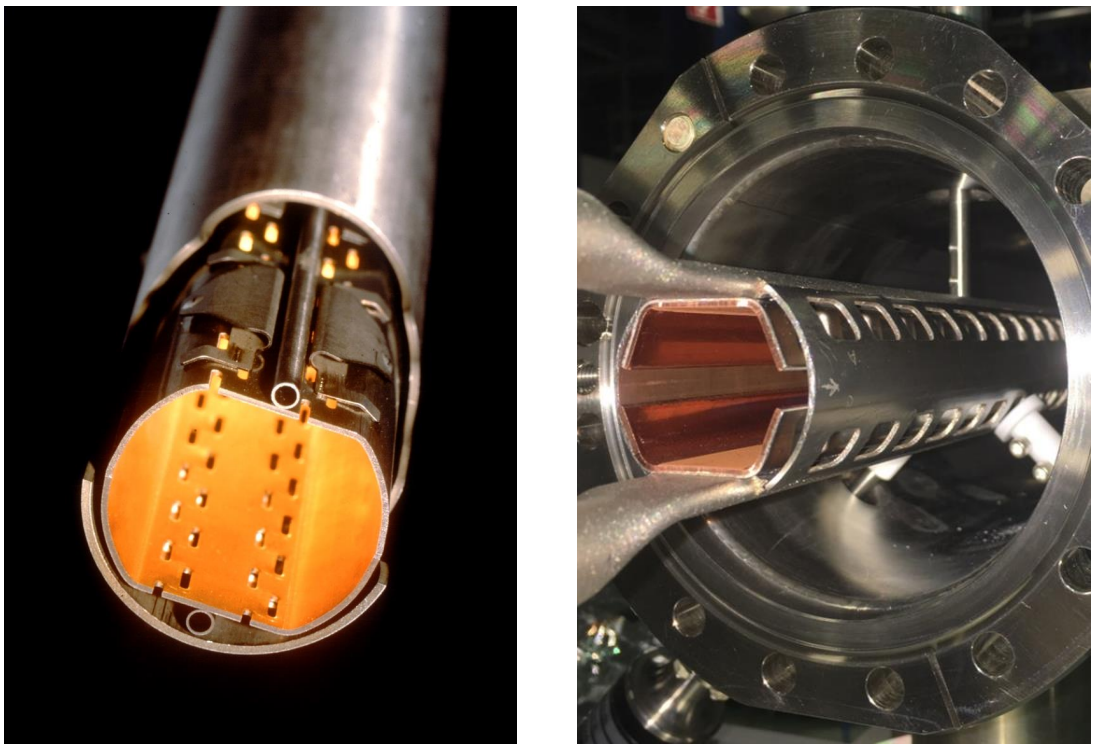

FIGURE 4.14: Photos of the LHC [87] (left) and the FCC-hh (right) BS.

MB with the highest average pressure is the third one, just before the SSS, because of having the highest SR average density. In this initial geometry the SR absorber was designed to intercept a considerable amount of SR power, casting a large shadow forward, easily noticeable in the graph as low pressure regions. No SR emitted in the SSS was considered in this calculation. The decay of pressure along the MB is ascribed to the SR linear density profile, being proportional to it.

In this calculation the only pumping region was the CB, with no pumping present in the interconnection. To run a pessimistic scenario, it is considered to be at the same temperature of the BS, a much higher temperature than the minimum one capable to condense a relevant amount of H_2 [50].

Considering that the SR emitted in the SSS is negligible and that most of the MBs receive the same SR power, the studied geometry was further simplified using a single MB as an infinite structure, representing the most irradiated MBs in the arc cell. This slightly over simplified approach was taken for the sake of simplicity and to increase the security factor of the calculations, with a clear objective of the feasibility evaluation in mind.

As previously explained, the FCC-hh needs around 4668 MB, each one with a B of 15.96 T [14]. This means that each MB needs to bend the beam around 0.077^{o}. Even if not much, it results in a sagitta of around 2.4 mm. It is not much, but it is considerably larger than the chamber's size, whose inner size is around 28.4 mm width. Therefore, it was decided to centre the beam leaving an offset of half of the maximum sagitta (1.2

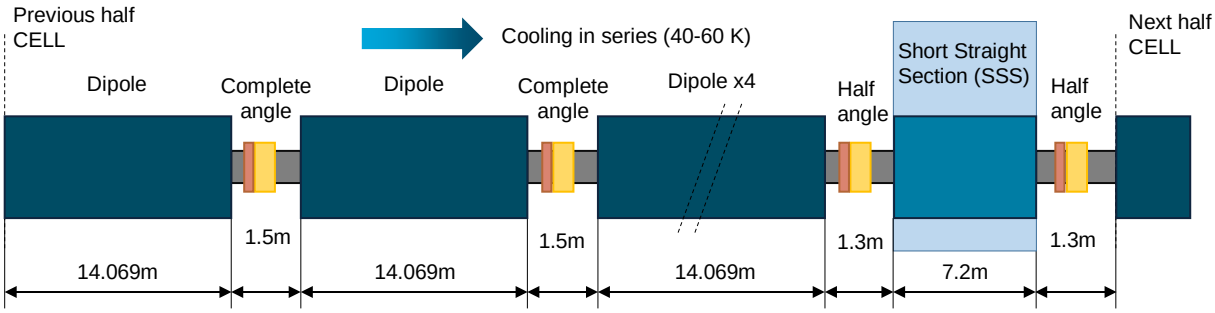

FIGURE 4.15: Schematic of the arc cell layout used in the simulations. The yellow sections represent the RF fingers, protected by the SR absorber, in copper.

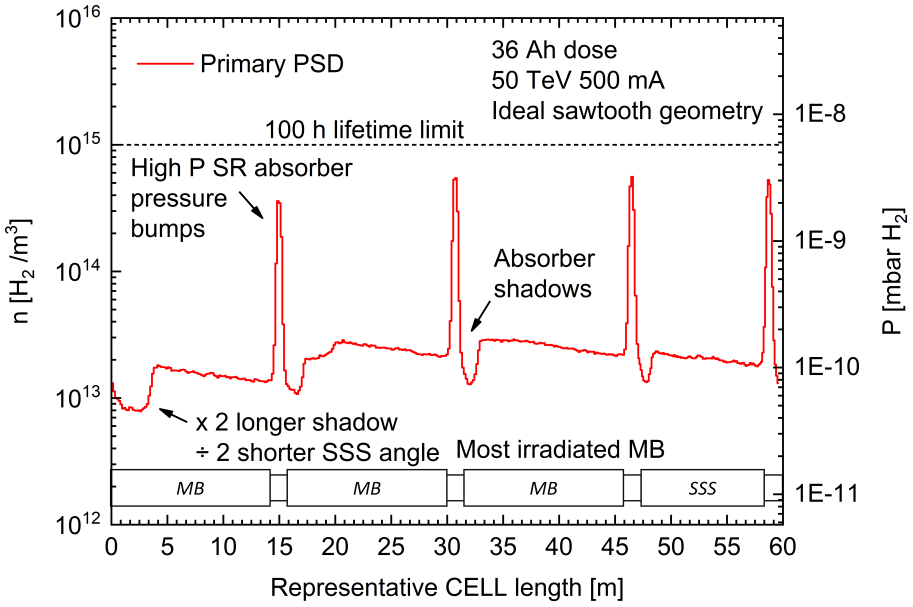

FIGURE 4.16: Pressure profile along a representative arc cell length, for a 50 TeV 500 mA proton beam. The BS geometry and arc cell layout are outdated.

mm) with respect to the chamber axis at the beginning and at the end of each magnetic region. This is represented in Fig. 4.17.

Consequently, the maximum offset with respect to the chamber axis in the middle of the MB BS is 1.2 mm as well. In case of the SSS, it should be misaligned 1.2 mm with respect to the theoretical orbit axis to take into account this misalignment at the exit of each MB.

4.4.2 Elements and functionalities of the beam screen

Besides the improvement of the cooling efficiency, the BS has many other functionalities: preventing wall instabilities, withstanding the generated Lorentz forces during magnet quenches, preserving the magnetic field quality, avoiding the e^- cloud development and ensuring a good vacuum quality. Each of the BS design features is intended

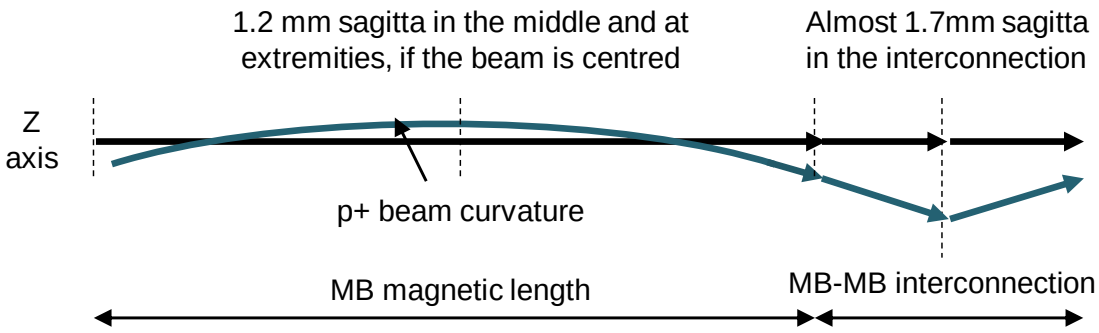

FIGURE 4.17: Scheme of the beam sagitta in the arc dipoles.

to address at least one functionality, with some features addressing many at the same time.

A functional design map of the BS functionalities, the related processes, and the applied design features can be found in Figure 4.18.

In the following pages, each BS element and functionality will be described, emphasizing its impact in the vacuum level and justifying its choice. Note that, even if properly assessed and operational, being part of a Conceptual Design Report, this design could change in the future in later stages of the FCC-hh design process.

4.4.2.1 Primary chamber

The primary chamber, also called inner chamber, is the innermost part of the BS, through which the beam passes. It has to guarantee a clearance large enough to contain a 15.5 σ beam aperture [89]. Its volume is delimited by two OFE Cu co-laminated SS P506 [31] bent sheets. Each bent sheet is 1.3 mm thick. The SS P506 part is 1 mm thick. This steel, developed in the past at CERN, is used to provide the necessary mechanical stiffness while yielding a low magnetic permeability (< 1.005) to preserve the magnetic field quality. The OFE Cu layer is 0.3 mm thick. It has been considerably increased with respect to the LHC BS, which is 0.075 µm [90] to lower the total resistive-wall impedance. It should have a residual resistivity ratio (RRR) of at least 100, and be kept as cold as possible to keep its resistivity low, given its dependence on the temperature [91]. The transverse resistive-wall impedance in the classical regime ($Z_{\perp}^{RW}$), a good approximation in the present case, is given by Eq. 4.14 [90]:

$$Z_{\perp}^{RW}(\omega) = (1+j)\,\frac{L\,Z_0}{\pi\,h^3}\sqrt{\frac{\rho}{2\,\mu_0\,\omega}} \tag{4.14}$$

where j is the imaginary unit, L the longitudinal length of the analysed geometry, Z_0 the free space impedance, h the BS half inner height (the pipe radius in a circular pipe), ρ the electrical resistivity, μ_0 the vacuum permeability and ω the angular frequency. It can be observed how the formula depends on the inverse of h to the power

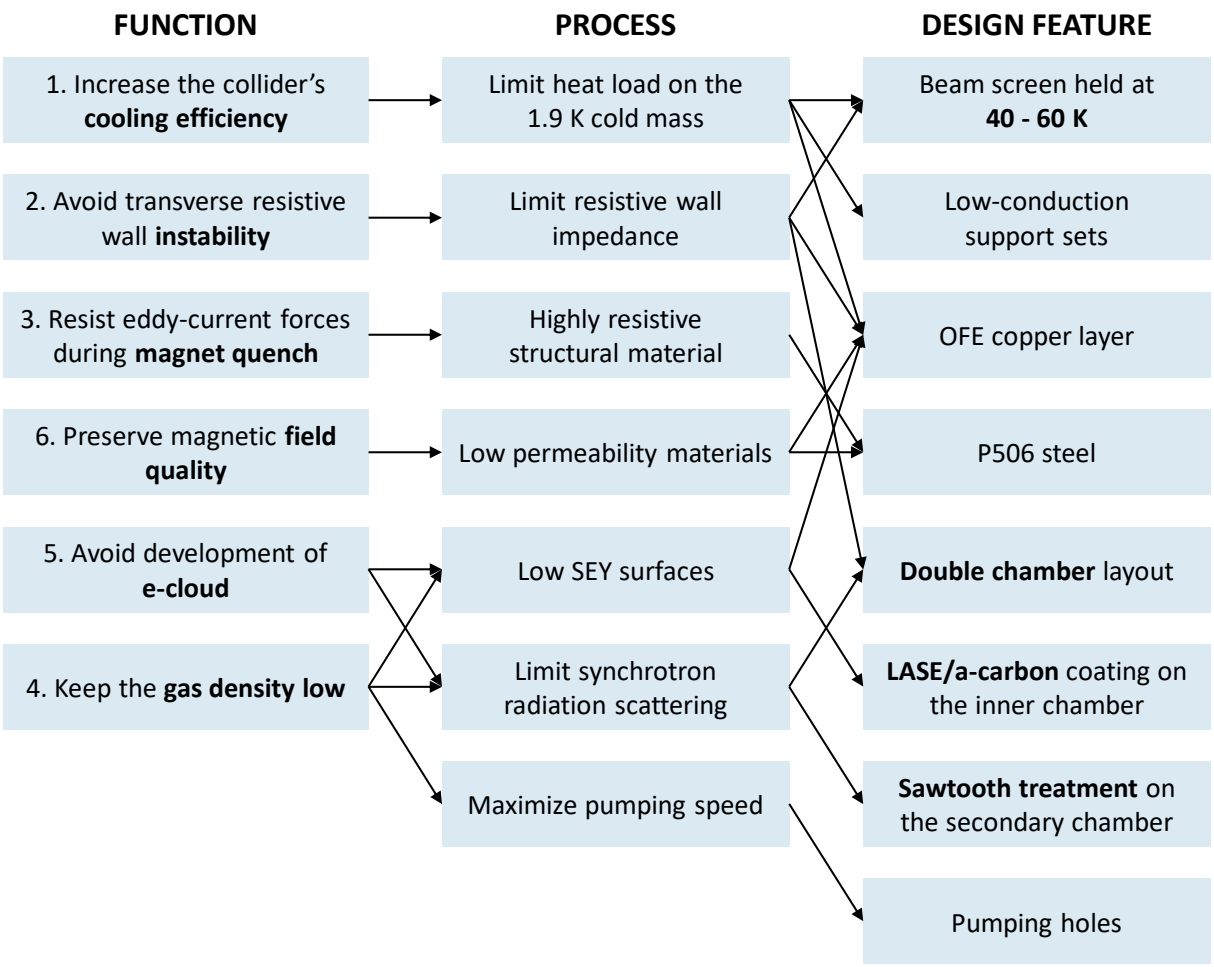

FIGURE 4.18: Functional design map of the FCC-hh BS. Updated from [88].

of three. Given the smaller h in the FCC-hh, and the higher ρ (due to the higher temperature) compared with that of the LHC, the impedance management in the FCC-hh has a considerably higher relevance. The height of the inner aperture has been tentatively maximized, with its main constraint being the size and welding methodology of the cooling channel. Even 1 mm of difference in the height can result in impedance increases of the 25% [92].

Provided that the e^- cloud is effectively suppressed, the primary chamber does not receive any significant heat load besides the beam image currents. Its temperature is directly determined by the coolant's one (the supercritical He). Owing to its good cooling efficiency, less than 0.5 K of temperature difference has been found between the Cu layer and the He in the worst case.

Most of the SR which passes through the longitudinal slot of the primary chamber is absorbed in the secondary chamber, and little SR is reflected back to it. Part of the SR tails touch the inner chamber, but they carry a minimum amount of power. The height of the central slot has an aperture of 7.5 mm. It has been designed in order to

allow a SR power transfer from the primary chamber to the secondary one higher than the 99.9% in all cases, even with the worst expected vertical beam misalignment (2 mm), whilst covering as much area as possible from the beam sight. If the beam didn't pass through the central slot, and touched the Cu layer of the primary chamber, many detrimental effects would happen:

- The temperature of the Cu layer would be considerably increased. This would entail a severe impact on the total impedance.
- The e^- development in the beam's path would be greatly enhanced, easily surpassing the instability threshold (see Subsection 4.4.5).
- The total gas load would rise, because of the higher ESD taking place and because of the SR wider distribution.

It is thus important to prevent this from happening. During the injection at 3.3 TeV, before ramping up the beam energy, the vertical misalignment could go up to 4 mm for a short time [93]. In this case, the SR would hit directly the inner wall of the primary chamber. Nevertheless, the low beam energy would result in a completely harmless SR, with a power emission and an ε_c even lower than those of the LHC (see Figs. 4.2 and 4.3). Consequently, neither of the previously mentioned detrimental effects arisen from this beam misalignment are expected.

To better understand the beam's path, a projection of the SR beam on a perpendicular plane in an old version of the FCC-hh dipole chamber, in arbitrary units, is shown in Figure 4.19. The proton beam is set at nominal beam parameters. The 2 mm misalignment has been applied.

The SR is shown emerging from the beam, which is represented by a yellow curve and it is directed outwards, passing through the central slot and hitting the left side of the chamber. The particle beam has the 2 mm misalignment applied. The SR beam has an approximate height of 2 mm when hitting the baffle with the engraved sawtooth profile. Even if the emission angle is small, the beam size and the length of the fly path until colliding with the baffle enlarge the final cone width.

Fig. 4.20 shows the plot of the SR flux and power distribution passing through the longitudinal slot, also with the 2 mm misalignment. The x axis represents the 7.5 mm height of the slot. It means that the part of the curves out of this plot does not pass through the slot and hits the lateral sides of the inner chamber, on the flat copper.

It can be seen how the SR power is well within the slot edges, meaning that most of the beam power is contained, and that the SR extraction is good enough. The SR flux curve, however, is significantly wider, and part of the right tail of the distribution lays out of the slot. A non-negligible part of the flux would then hit the side wall of the primary chamber. However, and as it can be guessed looking at Figs. 4.19 and 4.20, the outer tails of the SR beam, with a higher emission angle, carry photons with an

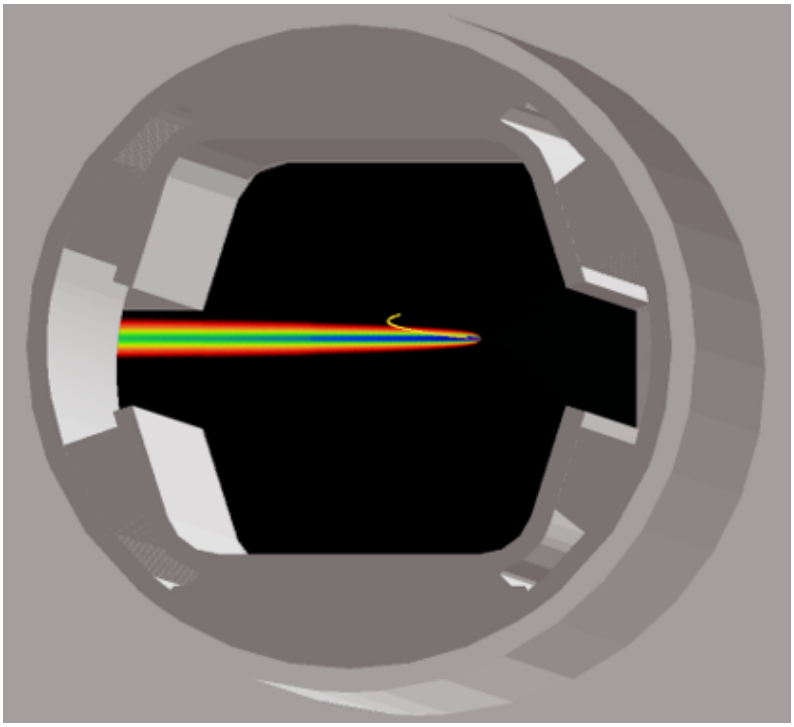

FIGURE 4.19: Projection of the SR beam on the frontal plane in an old BS design. Arbitrary units.

average energy much lower than the central part of the beam. The detrimental effects derived from this flux deposition have been found not to be significant.

During the course of the FCC-hh study it was realized that the edges of the two sheets delimiting the primary chamber will surpass the allocated impedance budget if left untreated, with the highly resistive SS P506 part being exposed to the beam [94]. Since the sheet is co-laminated, any straight cut will always leave the SS bulk visible. At 50 K and 1.06 T, SS is around 1000 times more resistive than Cu [94]. Its ρ is 6×10^{-7} Ω m, while for Cu is 7.88×10^{-10} Ω m. A similar issue exists in the LHC BS due to the longitudinal weld it presents on the opposite side of the sawtooth profile.

The chosen solution is to coat the edge with a 100 µm Cu layer, with electrical continuity with the co-laminated Cu layer. Such coating has to guarantee an electrical conductivity of at least 6.5×10^8 S/m at 50 K [95]. To apply the coating, cold spray and electrodeposition are the initially envisaged options. They should be compatible with the thermomechanical behaviour of the BS. Additional studies are required to fully assess the different technological options and features to produce this copper layer on the edge in a reliable and cost effective way [79]. The final aspect of the edge is shown in Figs. 4.12 and 4.35.

In order to suppress the e^- cloud effect, it is proposed to treat the Cu layer of the primary chamber with a low SEY coating. Between the two contemplated options, LASE [47–49, 96] and a-C [45, 46], the latter being the official baseline for the FCC-hh, owing to the maturity of the technology. Both of these options are able to lower the

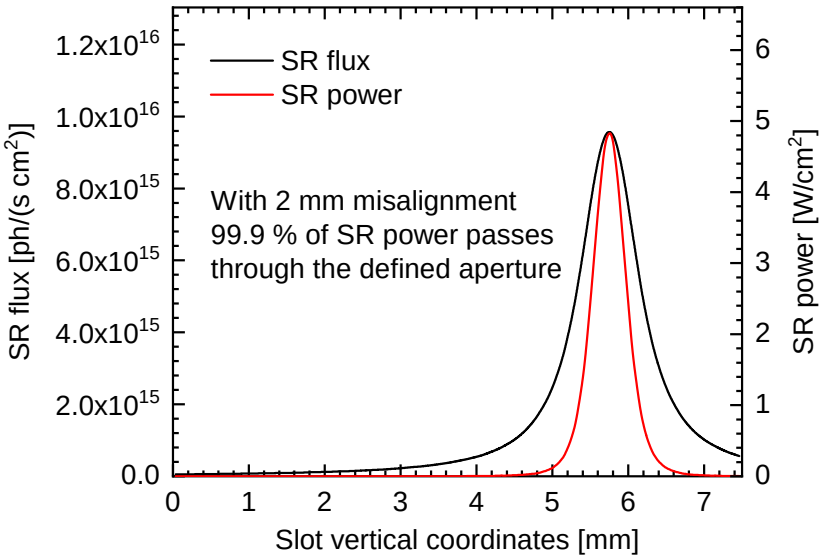

FIGURE 4.20: SR flux and P distribution when passing through the 7.5 mm slot of the primary chamber up to the secondary one, with a vertical misalignment of 2 mm. Baseline beam parameters.

SEY below 1 for the electron energy range of 0–1000 eV. More information on the e^- suppression is given in Subsection 4.4.5.

Both of these solutions have a high specific surface gas adsorption capacity, surpassing by a factor of 100 that of a flat Cu surface. Although during an ideal machine operation, a large gas coverage is not expected to be present on the BS, uncontrolled temperature regulations or magnet quenches could cause a gas redistribution and increase its condensation thickness. A temperature transient could then lead to unwanted gas density peaks, if the desorption temperature interval of the chosen SEY mitigation treatment falls within the temperature variation range [97]. To avoid this, the BS temperature might be adjusted in the future by around $\pm$ 20 K, as it happened to the HL-LHC BS [98]. However, since the exact specifications of the SEY mitigation treatment for the FCC-hh, and thus its desorption window, are not fully defined yet, this issue remains as future work. The impact of this temperature adjustment on the total gas load during steady state operation is expected to be minimal. In a standard dynamic mode, the photon and electron bombardment on the BS surface keep the coverage in equilibrium, within very low values. In static mode, the residual gas density is minimal and not sufficient to grow a significant coverage during turnaround times, so it is not a concern.

a-C is a layer of amorphous (graphitic) carbon, applied by DC magnetron sputtering physical vapour deposition. It has good electrical conductivity and low SEY, and it is widely described in the literature. The surface of the treated structure is homogeneously covered, with its thickness depending on the sputtering time.

LASE consists in the ablation of the surface by means of a high power density laser. This process is illustrated in Fig. 4.21. The diameter of the focused laser beam spot is

very small, and it is thus usually applied drawing a pattern of parallel and adjacent straight, narrow lines. The topology of the surface is dramatically changed, turning a flat and polished surface into a highly rough one, if enough energy is transferred to it. The treated surface can achieve a highly black appearance to the naked eye due to the light being trapped within the surface. It is for this reason that laser ablation treatment is also known as blackening process.

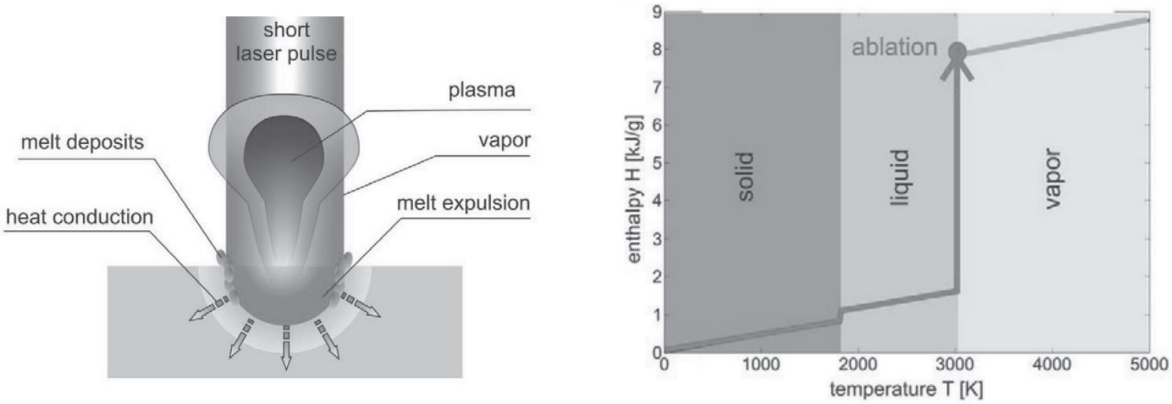

FIGURE 4.21: Classical beam-matter interaction (left) and classical ablation model (right) from [99].

The initial studies on this technology state that LASE's surface resistance is worse than that of a-C. This effect is thought to be ascribed to geometrical reasons, owing the high aspect ratio of its surface. In order to better understand its properties, some LASE samples were analysed with a scanning electron microscope (SEM) at CERN. An example of the taken pictures are shown in Fig. 4.22. The complex nano structure achieved by this treatment can be noticed.

That being said, recent studies have shown that the surface resistance of LASE can be minimized if the ablation ratio, and thus the SEY reduction, are low [100]; and/or if the treatment is applied in parallel to the beam's direction, achieving at cryogenic temperatures surface resistance values quite similar to a-C ones, even for high ablation rates [101]. Another issue of this technology is the dust creation. The ablation process leaves large amounts of micro and nano dust particles within the surface, which could come off during machine operation and fall into the beam's path. This issue is still being studied.

The samples of the LASE baseline variation were provided by the Accelerator Science and Technology Centre (ASTeC, UK), part of the EuroCirCol WP4. The chosen variation was made starting by commercially available rolled, electro-polished oxygen-free copper with high purity. It is produced by pulses of a Coherent Aviva NX laser operating at $\lambda = 355$ nm, $f = 40$ kHz, 75 ns of pulse duration and 3 W of average power [102]. The selected scanning speed was 120 mm/s.

A highly relevant feature of this technology, is that the laser parameters can be easily adjusted to the user preferences, changing in this way the surface ablation ratio and thus its final properties, such as the SEY. A slightly ablated surface would present

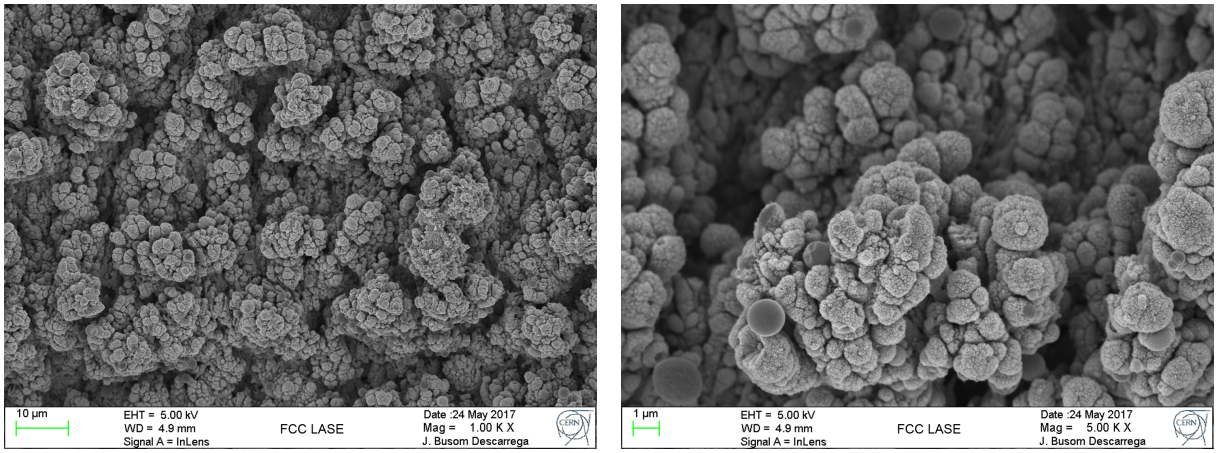

FIGURE 4.22: 1.00 K and 5 K SEM images of a Cu baseline LASE sample. Measured at CERN.

very similar properties as the original one, with little decrease of the SEY and keeping a surface resistance very close to the original one. On the contrary, a highly ablated one (up to a limit) would present a much lower SEY at the expense of a higher surface resistance.

From the manufacturing point of view, LASE is the preferred option. It is possible to apply it during a series production under atmospheric pressure, in addition to being able to select the specific regions to be treated, lowering the total production costs and easily enabling the primary chamber to present regions with different properties. Owing to its potentially lower cost, and the possibility to adapt its properties, this technology has been the preferred one of the EuroCirCol's WP4, and thus will be the one studied in this thesis.

4.4.2.2 Secondary chambers and sawtooth profile

Two lateral curved baffles, which are symmetrically assembled, close horizontally the annular space between the primary chamber and the CB, defining in this way the secondary chambers (see Figs. 4.12 and 4.35, for instance).

These baffles are composed by SS P506, 1 mm thick (all the BS components have the same thickness of SS), and an OFE Cu layer of 75 µm thickness, which acts as a heat carrier. By coincidence, the thickness of the Cu layer is the same as in the LHC BS. It has been optimized in order to minimize the baffle temperature and the stress generated during a magnet quench. The thicker this layer, the higher the heat dissipation, but also the higher the forces generated during a quench, so a compromise was found.

The baffle placed outwards from the ring centre receives the SR beam, with an average power of 29 W/m and an approximate height of 2 mm. This number is lower than the SR average P emission as the SR absorber and other components of the BS also dissipate some of the emitted power. The average grazing angle of the SR is 0.10^{o}, equivalent to approximately 1.8 mrad. It is higher than the angular offset between

magnets (0.077°) because of the long travel path of the SR from its emission until its first hit (around 21 m). This long distance makes that the SR emitted at the end of each MB misses the following one, impacting on the following MB with a doubled angular offset. This fact can be noticed in Fig. 4.5.

In order to evacuate the gas generated by the beam induced vacuum effects, each baffle has a series of periodic perforations, the pumping holes. They are 12 mm long with a 5 mm constant spacing, and they are placed on the farthest point from the beam impact region, to minimize the amount of SR leaked by reflection. In this position, the pumping holes are hidden, shielded from the beam's direct sight by the primary chamber walls, so no direct SR can pass through them, keeping the CB protected. Thanks to the double chamber layout, their size has been greatly enlarged compared to the LHC, and the pumping speed of the BS is maximized.

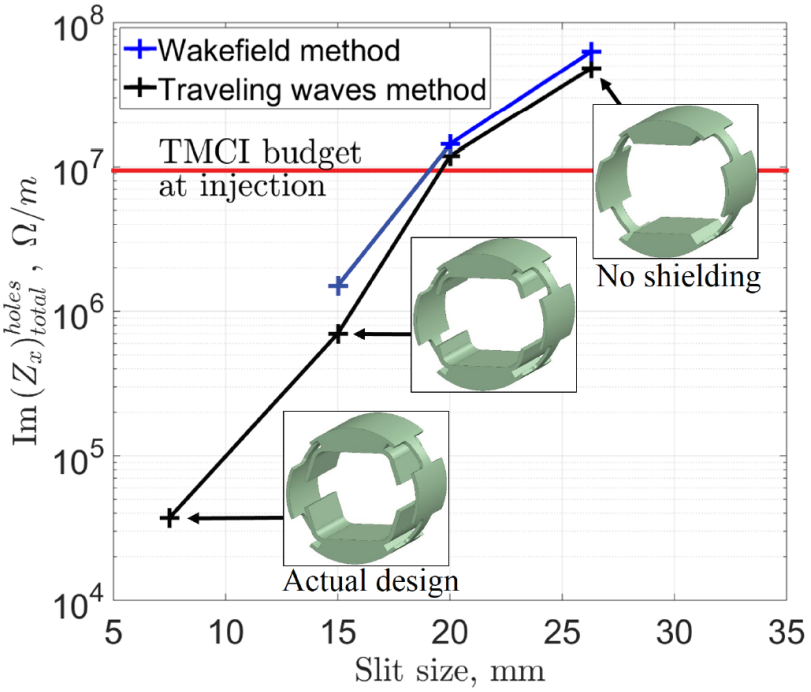

FIGURE 4.23: Horizontal broadband dipolar impedance of the pumping holes as a function of the central slot size. Taken from [103].

This shielding is also required for impedance reasons. Being the pumping holes shielded from the beam's sight, their contribution to the total impedance is very low [103]. Without the double chamber layout, the resulting impedance increase derived from their large size would easily surpass the impedance budget, making the BS unfeasible. This effect is illustrated in Fig. 4.23, taken from [103], where the broadband impedance of the pumping holes is calculated over the slot size. It can be noticed how the impedance grows exponentially the more the central slot is opened, and the more the shielding is lost. A bit before the shielding has completely disappeared, the budget is surpassed.

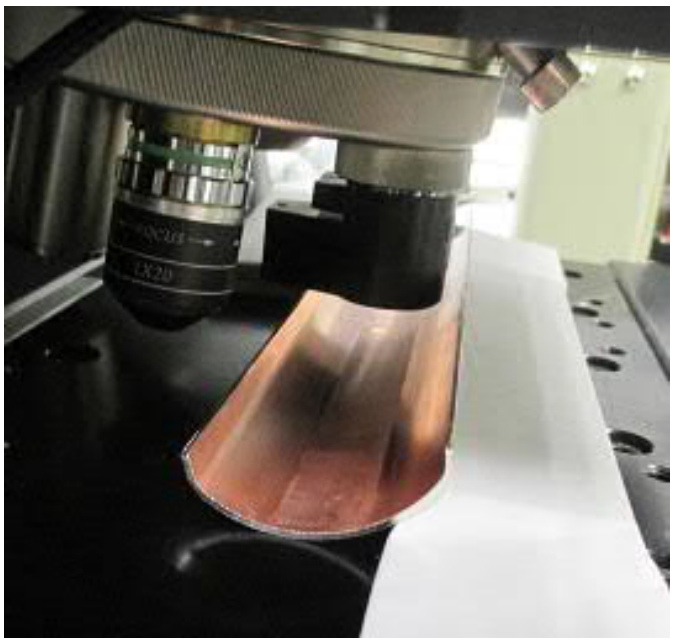

FIGURE 4.24: Measurement of the sawtooth profile with an optical profilometer at CERN.

On the baffle receiving the SR (see Fig. 4.25), a sawtooth pattern is engraved by means of a roller with a jagged relief on its surface. As previously stated, this feature was chosen to be implemented after a long analysis process.

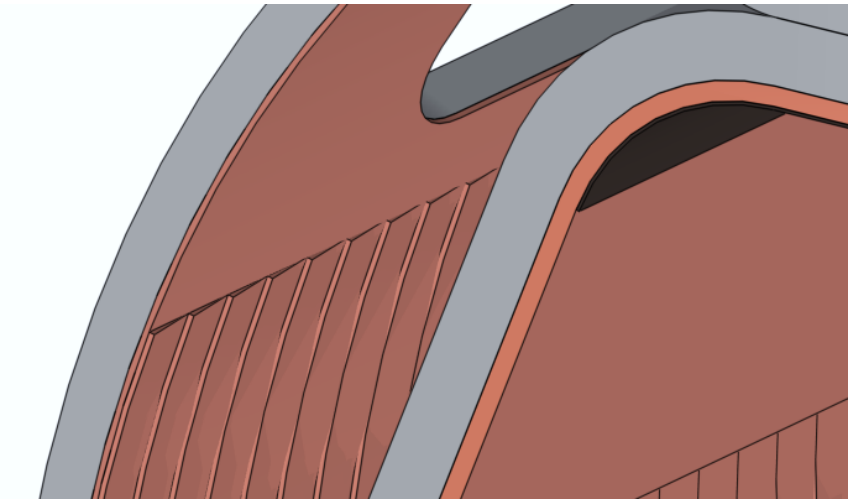

FIGURE 4.25: Schematic representation of the sawtooth pattern engraved on the secondary chamber Cu layer.

Given the hardness of the SS P506, it will be very difficult to engrave this relief on it, so the copper layer is also needed for this reason. As explained in Section 2.4, this treatment changes the grazing angle of incidence of the SR into a perpendicular one, minimizing in this way the SR reflection and scattering, since the photon reflectivity depends directly on the impact angle and the photon energy. Generally, the larger the grazing angle, the higher the absorption, and the same happens for the photon energy.

This is illustrated in Fig. 4.26. It can be seen that for a perpendicular incidence, the reflectivity for photon energies higher than 200 eV is negligible. For grazing angles lower than 0.3º, as the LHC and the FCC-hh cases, the reflectivity seems to be always significant even for photon energies as high as 10000 eV.

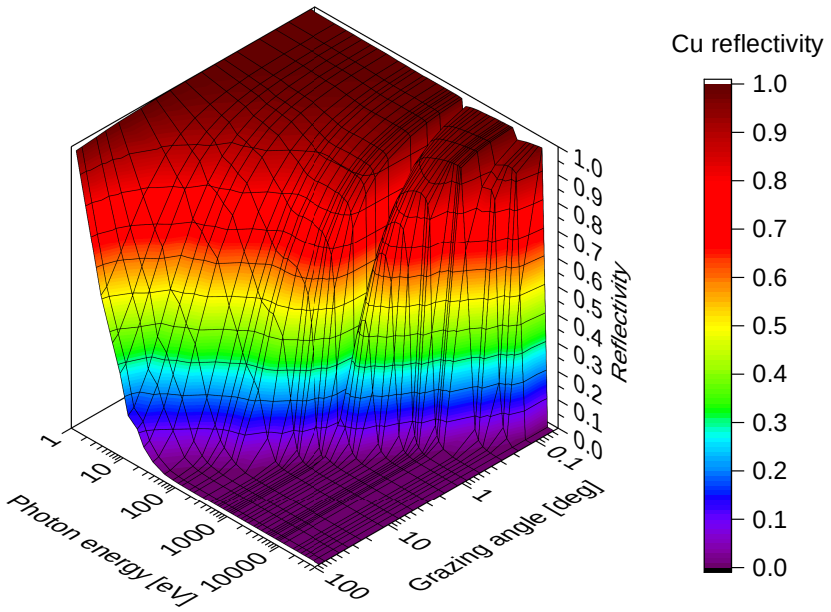

FIGURE 4.26: Copper raw reflectivity vs photon energy and vs grazing angle of incidence [53] used internally by Synrad+. The absorption edge $L_{II\text{-}III}$ at 945–965 eV can be easily noticed. Data for an ideally flat surface.

The only reason this feature is included in the BS design is to maximize the SR absorption on its first hit. However, it is one of the most critical elements of the BS design. According to the calculations, the inclusion of this element entails a series of beneficial effects:

- The total gas load attributed to PSD is greatly reduced, especially for low beam doses.
- The heat load on the CB is minimized. This allows much higher pumping holes, and thus lower gas density. The gas load attributed to PSD', is therefore lowered.
- Owing to the little SR reflected back to the main chamber, N_e and the e^- cloud density are diminished, and thus the beam disturbance. The gas load attributed to ESD is therefore lowered as well.

The generation of photoelectron seeds inside the secondary chambers are not relevant for the e^- cloud development in the beam's path. Being far from the proton beam, the kick that the electrons receive which each bunch passing is minimal, and thus their multiplication is prevented. In addition, being confined by the magnetic field lines,

they cannot reach the main chamber. And, owing to the curvature of the baffles, it is geometrically impossible that the photoelectrons generated on the sawtooth surface could pass through the pumping holes. The electron shield used in the LHC BS to prevent the electron impingement on the CB is thus not needed in the FCC-hh.

Implementing the sawtooth profile in the model has been challenging due to its complexity. First of all, to exactly know the real shape and surface properties of this surface finish, a sample of the sawtooth surface from the BS LHC and analysed at CERN's metrology lab with a Veeco optical profilometer, as shown in Fig. 4.24. The obtained close-up reconstruction of the surface is shown in Fig. 4.27.

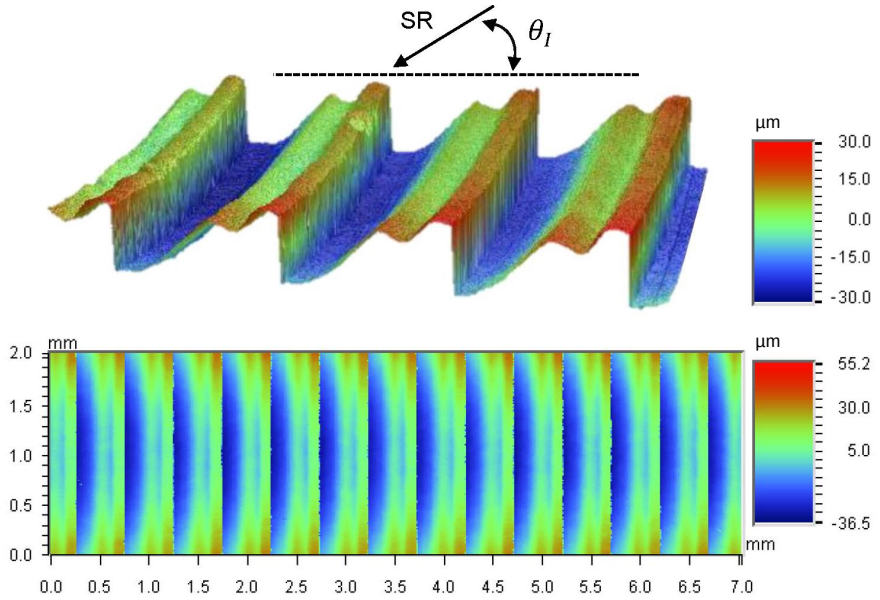

FIGURE 4.27: Close-up representations of the LHC BS sawtooth surface. Isometric view not to scale.

Its dimensions fit well the original specifications. Each tooth has a pitch of 0.5 mm and is around 40 µm high, from peak to valley. The SR impacts against the vertical walls with a grazing angle no lower than 75º, according to the original specifications. Nevertheless, as it can be seen in the Figure, owing to the limitations of the engraving process, each tooth is not as sharp as one might expect, being considerably rounded. The rounded edges causes the SR impinging on these regions to see grazing angles much lower than 1º, losing in this way the natural absorption properties of a pure perpendicular incidence. The shape and dimensions of the rounded areas have been found to be very variable, but they are mostly under 50 µm long and under 2 µm high.

In the LHC, the 0.29º between dipoles is translated in a transverse advance of the SR of 5 mm per m. With 2000 teeth per m, each tooth has around 2.5 µm of its height illuminated. In the FCC-hh, with 0.077º between dipoles, it would mean 1.35 mm/m of SR transverse advance and 0.7 µm of irradiated height per tooth. This means that in the FCC-hh, most part of the SR would end shedding on the rounded, highly reflective area. To make it worse, the lower grazing angle of incidence of the FCC-hh, would

dramatically exacerbate the reflectivity increment (see Fig. 4.26). This means that the LHC sawtooth, if used in the FCC-hh, needs to be properly studied and optimized, to counter the loss of absorption properties caused by the smaller grazing angle.

Drawing the exact shape of the rounded edges and implementing it in the simulation would be computationally and time-wise unfeasible. The high dependence of the reflectivity on the grazing angle also means that a simplified geometry, with a polygonal shape, cannot be used in the simulations either, since it would entail a large error in the results. Therefore, a benchmark study of the LHC sawtooth was carried out, to allow an emulation of the reflectivity properties with a computationally affordable geometry.

In the benchmark, theoretical simulations have been compared with experimental data. After benchmarking this solution, the performance of the sawtooth profile for the FCC-hh case has been calculated. Similar studies were also done recently [104, 105] in a theoretical way.

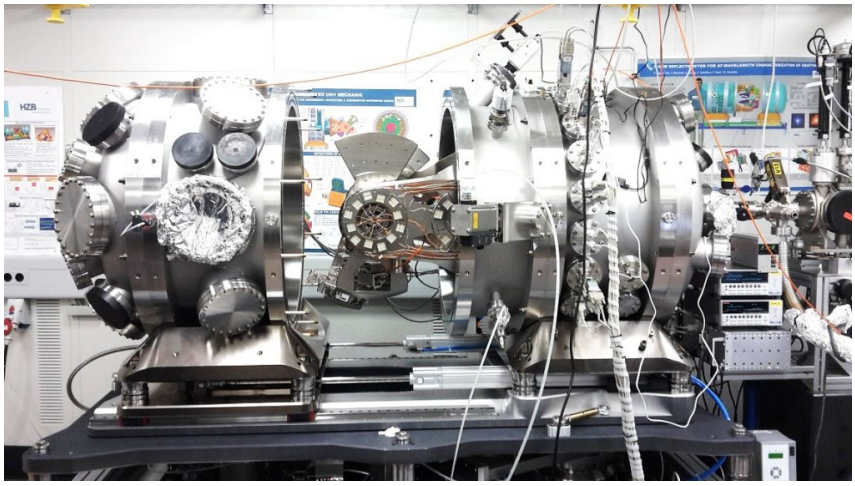

FIGURE 4.28: Reflectometer in BESSY II's beamline [106], showing part of the system used to align samples.

The reflectivity experimental data were acquired in a dedicated optics beamline in BESSY-II synchrotron light source, using a state-of-the-art reflectometer, shown in Fig. 4.28. These data were acquired in the framework of a collaboration between LNF-INFN and CERN. As explained in Chapter 3, this collaboration was arranged after the evaluation of the input data available in the literature which were necessary to study the detrimental effects of the SR in the FCC-hh. After realizing that many of the data were missing, (mainly the SS P506 reflectivity and photoelectron yields of raw Cu, sawtooth Cu, LASE and SS for the range of energies of interest, very difficult to estimate), it was decided to acquire them experimentally. Later on, after discarding the initial FCC-hh BS design and changing the strategy to handle the SR, the granted beam time was exploited to study the LHC sawtooth profile. The acquired data were processed and published by LNF-INFN, and can be found in [107–110].

The performed benchmark study will be described here, along with a brief explanation experimental procedure, for the sake of completion. A complete description of the experimental procedure can be found in [107, 108].

The experiment consisted in irradiating one LHC BS sample with a known flux of monochromatic light and measuring the reflected flux with a well characterized GaAsP photodiode, hence knowing the reflectivity of the sample for the established parameters. A basic schematic of the set-up is depicted in Fig. 4.29.

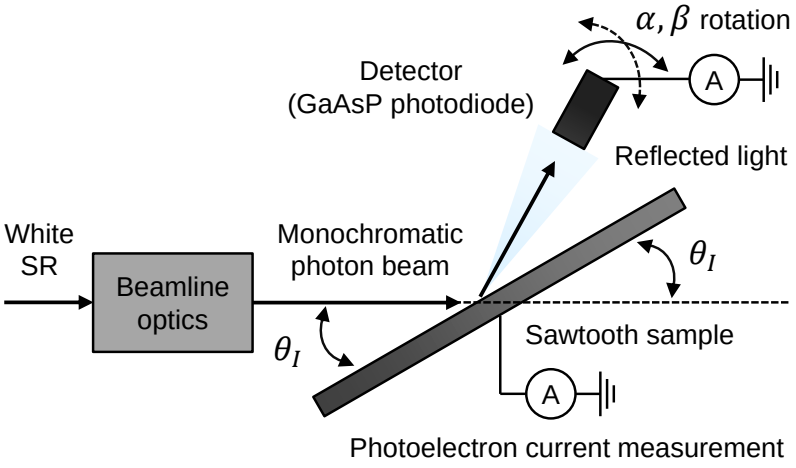

FIGURE 4.29: Schematic description of the set-up in BESSY–I's XUV optics beamline.

The photon energy ($h\nu$), angle of incidence with respect to the plane of the sample (θ), the elevation (α) and the azimuth of the detector (β) can be varied.

An approximate measure of the total reflectivity is obtained with the sum of all light reflected over the angular range which spans 175º in the median plane and 3.5º in the azimuthal one. The photon flux outside of this cone has been found to be low enough to safely discard it aiming to shorten the data acquisition time. The specular reflectivity is defined as the ratio of light measured placing the detector at an angle of 2θ, the natural angle of reflection. The detector counts all photons in its angular acceptance cone $\pm$ 0.35º. The experimental setup allows to measure the photoelectron yield (Y_{ph}) by reading the sample's drain current at the same time of the reflectivity measurement.

The grazing angles chosen for the experiment are 0.25º, 0.5º and 1º. These values, ideal for the LHC's case, are low enough to provide an acceptable extrapolation to the FCC-hh's SR angle. In addition, this angle range allows to observe a variation of the reflectivity of one order of magnitude, increasing the reliability of the performed benchmark. The available energy range in the reflectometer is mostly set in the soft X-ray region, from 35 eV to 1800 eV. For the total reflectivity, the granted beam time allowed to measure at 50 eV, 150 eV, 400 eV, 1200 eV, and 1800 eV for the all the chosen angles. The obtained experimental data are plotted in Fig. 4.32.

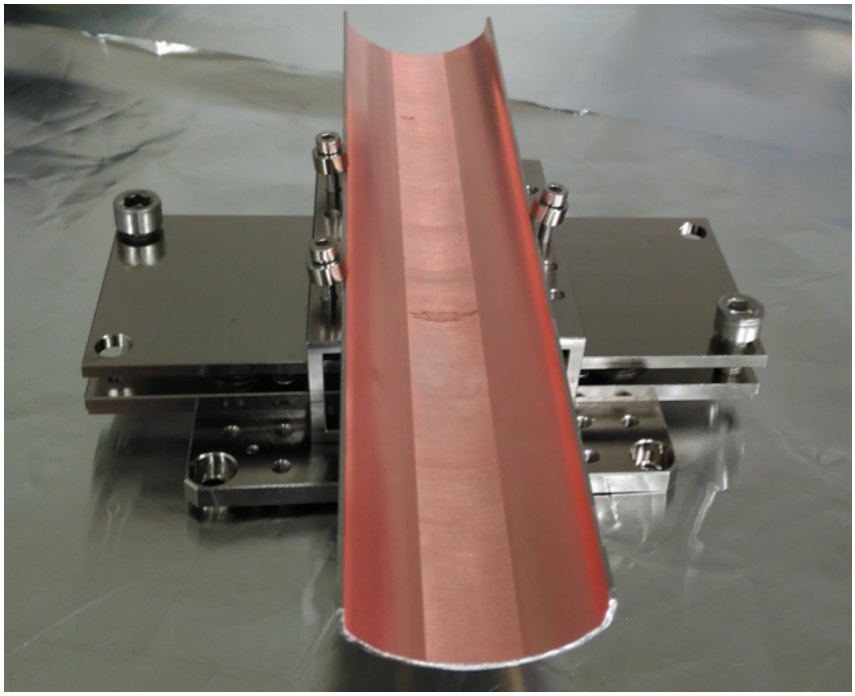

FIGURE 4.30: Clean BS sample mounted in the reflectometer's sample holder. The sawtooth region is clearly visible in the middle.

The main sample is the same one which was previously used to analyse the real dimensions of the sawtooth profile (see Fig. 4.27). It is a 300 mm long section of the actual LHC BS, longitudinally cut in half by laser. It is shown in Fig. 4.30. It is composed of a 1 mm thick bent sheet of SS P506 with a co-laminated OFE copper layer 75 µm thick, RRR=100 [90, 111, 112]. The sawtooth pattern is engraved on the copper layer along all its length with $\pm$ 7.5 mm of vertical extent from the equatorial plane.

The sample was cleaned in a standard degreasing ultrasonic bath for UHV purposes. The thick oxide layer present in the old sample was also removed with a light acid etching, rising the surface purity in exchange for an increase in its roughness. Its surface morphology was then analysed with an optical profilometer at CERN's Metrology Lab and at CSEM, both in Switzerland. The average surface roughness (R_a) out of the engraved region of the studied sample is 0.28 µm, higher than the 0.2 µm R_a of the original manufacturing specifications.

A second sample has also been studied to be compared with the main one. This sample is a longitudinal portion of one of the flat Cu areas of the LHC BS, with neither sawtooth nor etching.

To perform the theoretical calculations, an LHC BS model has been drawn and used to perform ray tracing simulations with Synrad+ according to the metrology surface data of the measured sample. More about these simulations is explained in Subsection 4.4.4. All sawtooth surfaces have been treated as pure Cu. Fig. 4.31 presents the dimensions of the sawtooth pattern used in the benchmark, in black. Being the dimensions of the rounded edges so variable, and since a rounded shape would be computationally

expensive, each rounded edge has been simplified as a flat edge. Its exact length and orientation has been iteratively varied within the measured range of sizes until arriving to an optimal match with the previously acquired experimental data, shown in Fig. 4.32. The roughness ratio $\tau_r = R_q/T_r$ (where R_q is the RMS surface roughness and T_r is the autocorrelation length) of the cleaned sawtooth sample has been set to 0.011 in the simulations, and around 0.007 for the as-received one (see Table 4.2), as found in the metrology studies. The physical interpretation of T_r is that it expresses the minimal distance between two profile points not interrelated, giving information about the surface spatial complexity. For the benchmark of a standard, uncleaned treatment, τ_r has been set to 0.006 as a conservative scenario.

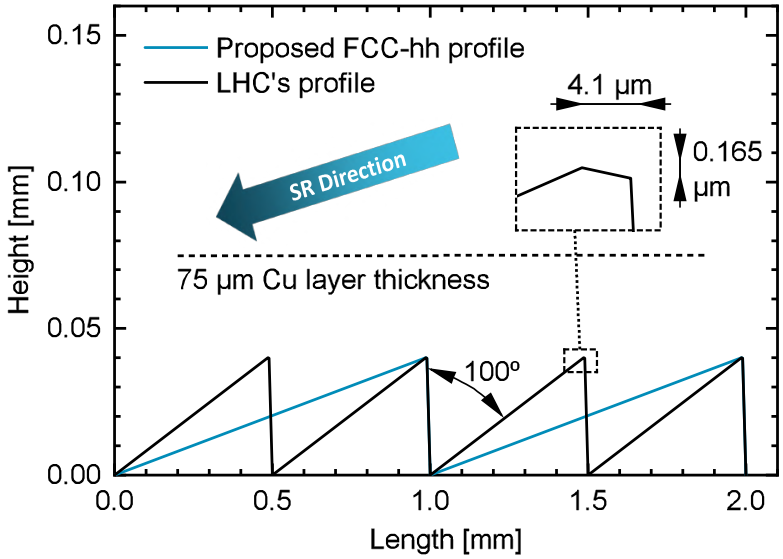

FIGURE 4.31: LHC sawtooth profile used to benchmark the treatment's reflectivity compared with the proposed one for the FCC-hh.

After validating the model and the computing tools with the experimental data, the performance of the sawtooth surface has been analysed for the FCC-hh case, using the latest BS geometry. The power absorption on the first hit, the total photon flux ($\dot{\Gamma}_{ph}$), the equivalent critical energy ($\varepsilon_{c\,eq}$) and the N_e arriving to the inner chamber have been calculated. N_e is calculated with Eq. (4.15). Note that this value can be expressed as total generation rate [electron/s], or more commonly, it can be expressed in area units [electron/(s cm^2)]. In this case, Γ_{ph} is consequently expressed as flux density [photon/(s cm^2)]. Its values are given for an untreated copper surface and a LASE treated one, which has a much lower Y_{ph}.

$$N_e = \int_{E_{min}}^{E_{max}} \dot{\Gamma}_{ph}(E)\; Y_{ph}(E)\; dE \tag{4.15}$$

The Y_{ph} values used are the ones acquired in the experimental run [108]. The values of Γ_{ph} (in [photons/cm^2]), which depend on the photon energy, have been obtained in the ray tracing simulations, separately for each studied region. An example of the

photon spectrum used to calculate N_e is shown in Fig. 4.44. The performance results have been compared against the initially proposed reflecting edge solution, against an untreated surface and against a sawtooth variation, proposed in order to improve the absorption properties. The FCC-hh beam parameters used in this calculations are the design ones, mentioned in Section 3.1.

TABLE 4.2: Relevant surface roughness parameters found in the metrology analyses.

Measured surface	R_q	T_r	τ_r
SS P506 machined	230 nm	34.5 µm	0.0066
LHC BS untreated	226.4 nm	31.2 µm	0.0073
LHC BS cleaned	351.3 nm	33.3 µm	0.011
LASE high ablation grade	11.9 µm	10.8 µm	1.1

The comparison of the measured reflectivity and the simulated one can be found in Fig. 4.32.

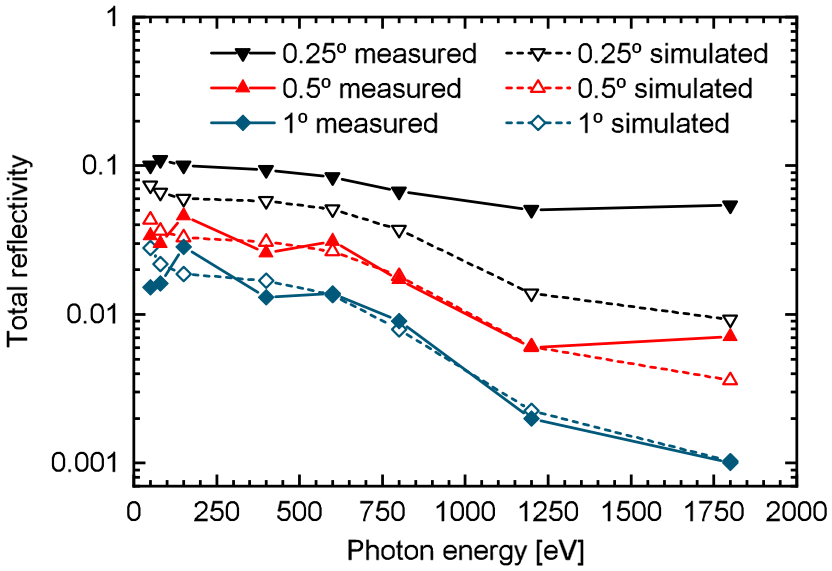

FIGURE 4.32: Comparison between the data experimentally acquired in the optics beamline [108] and the simulated results for the LHC sawtooth cleaned sample.

As it can be seen, for the measurements at 0.5º and 1º the obtained match is quite acceptable, with a coefficient of determination (R^2) of around 0.94 in both cases for photon energies above 400 eV. For both incidences an unexpected increase of reflectivity was measured when raising the photon energies from 80 eV to 150 eV. Being this region out of the main absorption edges of the main elements present in the sample's surface, there is no direct analytic explanation of this behaviour other than the intrinsic error of the measurements. The reflectivity measured for the 0.25º is unexpectedly high, presenting a strong increase from the measurements at 0.5º, much higher than

the observed increase from 1º to 0.5º. This difference is thought to be attributed to the surface contaminants [108], namely oxygen and carbon, (always present in a higher or lower content despite the cleaning processes) which feature a higher reflectivity than copper at high photon energies. This surface layer, not taken into account in the simulations, may have a stronger interaction with the incident photons at lower grazing angles, resulting in an underestimation of the total reflectivity.

For the sake of completion, a comparison of the specular reflectivity of the sawtooth sample and the untreated one is shown in Fig. 4.33, from [108]. The curves belonging to the flat and uncleaned sample show clear absorption edges corresponding to C and O, whilst in the sawtooth sample (cleaned) are not so well distinguished, hinting a lower contaminant content.

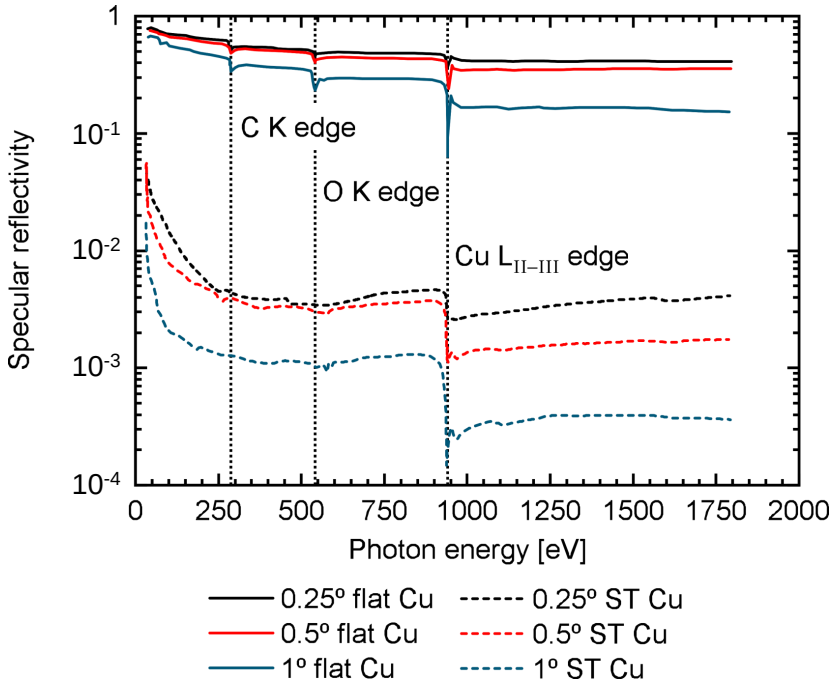

FIGURE 4.33: Comparison of the specular reflectivity measurements of the LHC sawtooth and a flat, untreated LHC BS sample, adapted from [108]. The much higher absorption of the sawtooth treatment can be noticed.

Given the high variability of the sawtooth dimensions and to cover the possible reflectivity underestimation for low grazing angles, a factor of ≈ 2 has been applied to the rounded edge dimensions. This allows us to evaluate a more pessimistic scenario in the calculations of N_e, approximately doubling the intrinsic reflectivity of the modelled sawtooth. Even if the reflectivity underestimation can be larger than 2 for photon energies higher than 750 eV (see Fig. 4.32), it is not highly relevant; the photon energy range contributing the most to the total value of N_e has been found to be in the energy range between 30 eV and 500 eV. The resulting dimensions of the fitted profile (see Fig. 4.31) are 8.5 µm of width and 0.3 µm of height. The total reflectivity of this

LHC studied sawtooth; with the safety factor of 2 already applied, is then plotted in Fig. 4.34 for the calculated FCC-hh average angle of SR incidence.

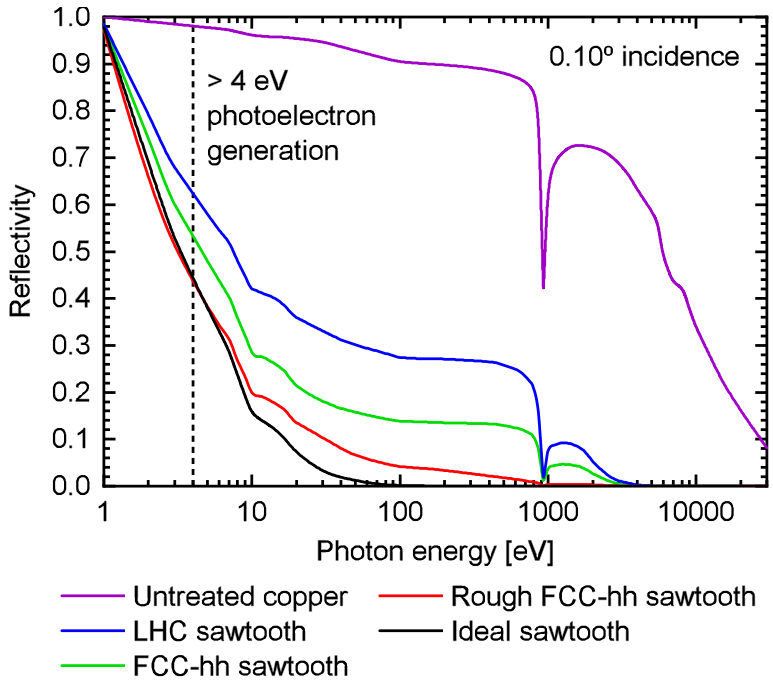

FIGURE 4.34: Comparison of the simulated reflectivity of the LHC and FCC-hh sawtooth profiles against an ideal one and an untreated copper surface, with $\tau = 0.006$ and for the FCC-hh's average grazing angle of SR incidence. The rough sawtooth is calculated with $\tau = 0.3$.

For comparison, the reflectivity of an ideal sawtooth; with perfectly sharp edges, and a flat untreated surface, is also plotted. The efficacy of this treatment in lowering the reflectivity of high energy photons can be clearly noticed, especially for hard X-ray radiation, for which it presents a negligible reflectivity. In the studied scenario, the LHC sawtooth would achieve a 96% of average SR absorption for the FCC-hh baseline beam parameters, while an untreated Cu surface would absorb only a 46%.

As previously stated, the SR grazing angle of the FCC-hh increases the weight of the sawtooth rounded areas in the total SR irradiation and thus decreases the sawtooth effectiveness. These areas are inherent to the manufacturing process and minimizing them is essential to mitigate the detrimental effects of the SR in the beam vacuum system of the FCC-hh.

Therefore, and without breaking down the manufacturing process, two preliminary solutions are proposed in order to further enhance the absorption properties of the sawtooth profile if used for the FCC-hh:

- The first solution is to increase the height of irradiation of each tooth, which decreases the percentage of the SR impinging on the rounded areas. For that, the tooth pitch can be increased, which can be easily done by modifying the geometry of the gear which engraves jagged edges onto the co-laminated sheet. As seen

in Fig. 4.34, this solution decreases by approximately a factor of two the number of reflected photons within a range of energy of 100–800 eV.

- A second solution, complementary to the first one, is to increase the surface roughness, which directly enhances the SR absorption. For that, the surface of the engraving gear can be treated, to directly imprint the enhanced roughness on the Cu sheet, or the sawtooth surface can be treated after the rolling process. LASE could be effectively used to increase the surface roughness of Cu in a series manufacturing process and in a cost effective way. R_q values higher than 10 µm can be achieved, multiplying by more than 40 times the original surface R_q. The reflectivity properties of the FCC-hh baseline LASE treatment have also been analysed at BESSY-II's optics beamline, showing an excellent light absorption, around one order of magnitude higher than that of the studied sawtooth sample [108, 109]. Since it can be applied with high accuracy, it is possible to only treat the rounded edges (less than 10% of the total treated surface) saving costs, with the same reflection properties as a fully treated flat surface.

Another benefit of using LASE to increase the surface roughness is the reduction of the total gas load attributed to primary PSD (besides of ESD because of the lower N_e in the inner chamber), which represents around the 80% of the total one at low beam doses. Such benefit was predicted, since, according to the consulted literature, the SEY, Y_{ph} and η_{ph} are usually related. This theory was experimentally checked at BESTEX [66], where the LASE Cu was found to yield a much lower η_{ph} than the untreated Cu areas. This strategy is therefore recommended as a future R&D subject.

However, considering that the use of LASE in the FCC-hh is not completely validated yet, and lacking data about its impact on the beam impedance, only the first option of pitch increase is covered here. As a safe proposal, it has been doubled, setting it in 1 tooth per mm (see Fig. 4.31). Simply removing 1 tooth every two teeth would approximately yield the same results. This can also be an option if it is preferred from the manufacturing point of view and/or if making longer teeth cannot guarantee a similar total rounded area. Derived from the reduction of teeth number/longer pitch length, a higher SR power would be present on each tooth, increasing the related thermal stress. For the 1 mm option, it is nevertheless safe [79].

The reflectivity results of doubling the tooth length have been computed and added to Fig. 4.34. To the same geometry a roughness ratio of $\tau = 0.3$ has been applied to estimate the effects of surface roughness increase. Such value has been conservatively chosen according to the LASE's metrology results. It can be observed how both curves are substantially lower than the one corresponding to the original LHC sawtooth, reaching photon absorptions higher than 80% even for the UV range.

A final comparison of the FCC-hh proposed sawtooth, LHC sawtooth, an untreated Cu surface and the initially proposed option of a reflecting SS edge has been carried out using Synrad+. It is shown in Tables 4.3 and 4.4. Different performance parameters

TABLE 4.3: Performance summary (I) of all the contemplated options to absorb the SR on the vacuum chamber wall. The shown percentages refer to the fraction of the total SR power generated per FCC-hh bending magnet (498.7 W). N_e represents the photoelectron generation in the flat areas of the inner chamber.

Absorbing surface	Absorbed SR P	SR P on inner Cu	SR P on cold mass	$\varepsilon_{c\ eq}$ on flat areas [eV]
Rounded SS edge	43%	18.7%	7.1×10^{-2} %	3730 eV
Flat OFHC Cu	46%	5.3%	1.8×10^{-3} %	885 eV
LHC sawtooth	96%	0.27%	4.4×10^{-4} %	280 eV
Proposed sawtooth	98%	0.14%	3.4×10^{-4} %	270 eV

TABLE 4.4: Performance summary (II) of all the contemplated options to absorb the SR on the vacuum chamber wall. N_e represents the photoelectron generation in the flat areas of the inner chamber.

Absorbing surface	N_e for Cu [$e^-/(cm^2\,s)$]	N_e for LASE [$e^-/(cm^2\,s)$]	Assessment for the FCC-hh
Rounded SS edge	3.1×10^{13}	1.6×10^{12}	Non-viable
Flat OFHC Cu	3.2×10^{12}	3.7×10^{11}	Non-viable
LHC sawtooth	3.1×10^{11}	7.1×10^{10}	Acceptable
Proposed sawtooth	1.0×10^{11}	2.3×10^{10}	Optimum

have been calculated using an infinite series of FCC-hh dipoles, baseline beam parameters and with the realistic sawtooth model found using BESSY-II's data including a safety factor of 2.

Among the displayed values, we can highlight two main figures of merit: the SR power leaked to the cold bore and the electron generation rate due to the photoelectric effect (N_e) on top and bottom areas of the inner chamber. The minimization of both of them has direct implications for the collider's performance, improving the cooling performance and the beam and vacuum quality. It is advisable to have a N_e much lower than 1×10^{12} $e^-/(cm^2\,s)$ [79].

The FCC-hh sawtooth, with 1 mm pitch, features the best performance, reflecting the least amount of SR power towards the cold bore and the inner chamber, guaranteeing then the lowest gas load inside the BS among all the displayed options. The LHC sawtooth would perform well but below the modified one. Thanks to the near-perpendicular angle of SR incidence, only low energy photons are reflected. In these cases, the equivalent critical energy ($\varepsilon_{c\ eq}$) of the SR arriving to the inner chamber is kept below 300 eV, much lower than the FCC-hh's one, 4286 eV. As seen previously, a flat, untreated beam screen wall, and the initially proposed reflecting edge are not recommended options for the FCC-hh. The N_e values for this cases are too high even with a LASE treatment, and the amount of SR power redirected towards the cold mass would make the total thermal budget of the cold mass to be surpassed [79] in the case

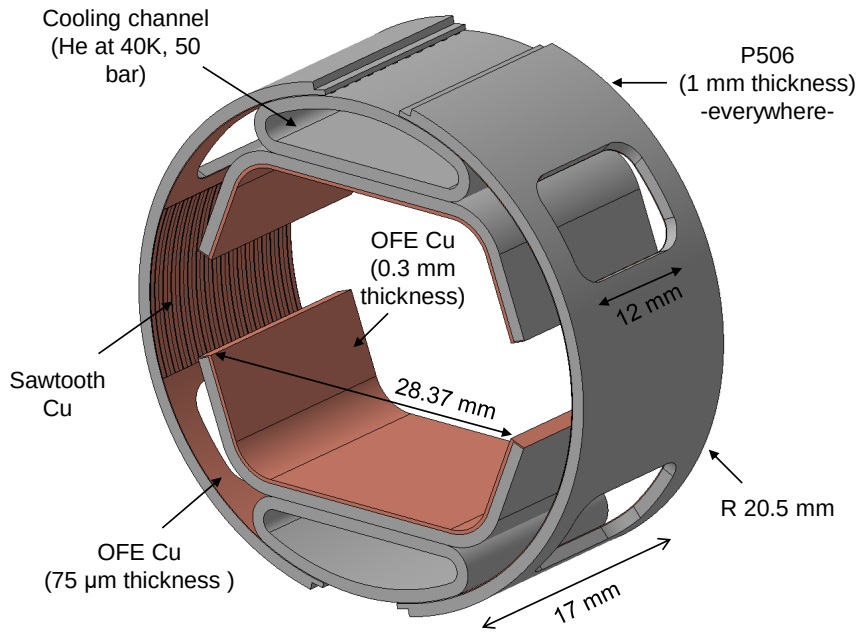

FIGURE 4.35: A representative periodic unit of the FCC-hh, of 17 mm long.

of the reflecting strategy.

4.4.2.3 Cooling channels

Two SS P506 cooling channels are placed top and bottom of the BS (see Fig. 4.35). They are welded on top of the two bent pieces giving shape to the primary chamber and welded to the two lateral baffles. Supercritical He flows through them and takes away the generated heat inside the BS, originated on its largest extent by the SR. Every half cell ($\approx$ 107 m, see Fig. 2.4) is separately cooled, in parallel. At nominal beam parameters, the He would be at 40 K and 50 bar in the inlet and at 57 K at the outlet [113] (it is approximated as 60 K in this thesis and most of the literature, for the sake of simplicity). These cooling channels have a considerably larger cross section than those of the LHC BS in order to dissipate the higher SR power (35.4 W/m vs 0.22 W/m). They have a heat transfer coefficient of 5000 W/(K m^2) [114], and would be manufactured by extrusion.

4.4.2.4 Cold bore and supporting system

The CB is a SS 316 LN pipe, 1.5 mm thick and with an outer diameter of 47 mm. It can be seen in Figs. 2.12 and 4.14. It is kept at 1.9 K, and has the same functionalities as in the LHC. It separates the superfluid 1.9 K He that surrounds the magnet coils from the beam vacuum. This low temperature, needed to achieve high current densities in the coils, is exploited also to turn it into a highly efficient cryopump. It provides the only means of pumping during normal operation. The BS is inserted inside and supported by periodic SS P506 spring sets (see Fig. 4.36) placed every 750 mm [79]. They have

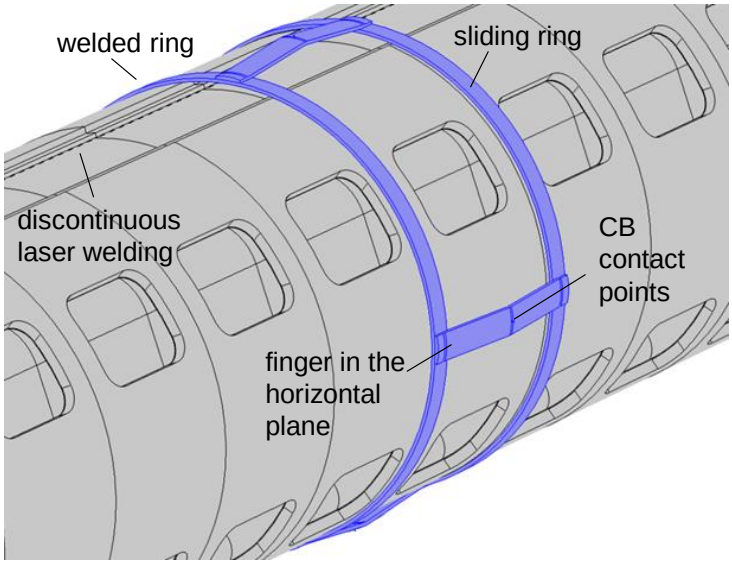

FIGURE 4.36: Supporting system of the FCC-hh BS [79].

been designed to ease the insertion of the BS in the CB, to minimize the heat transfer from the BS to the CB and to withstand the forces generated during a magnet quench.

The supporting solution used in the LHC, short bi-metallic rings with an inner SS layer and outer bronze one [115, 116], has been discarded for the FCC-hh due to its higher heat conduction, an issue which would be exacerbated in the FCC-hh BS due to its higher temperature.

4.4.2.5 Interconnections

The continuity of the beam pipe in the arcs is broken at the magnet interconnections. An example of a MB-MB interconnection of the LHC is shown in Fig. 4.37.

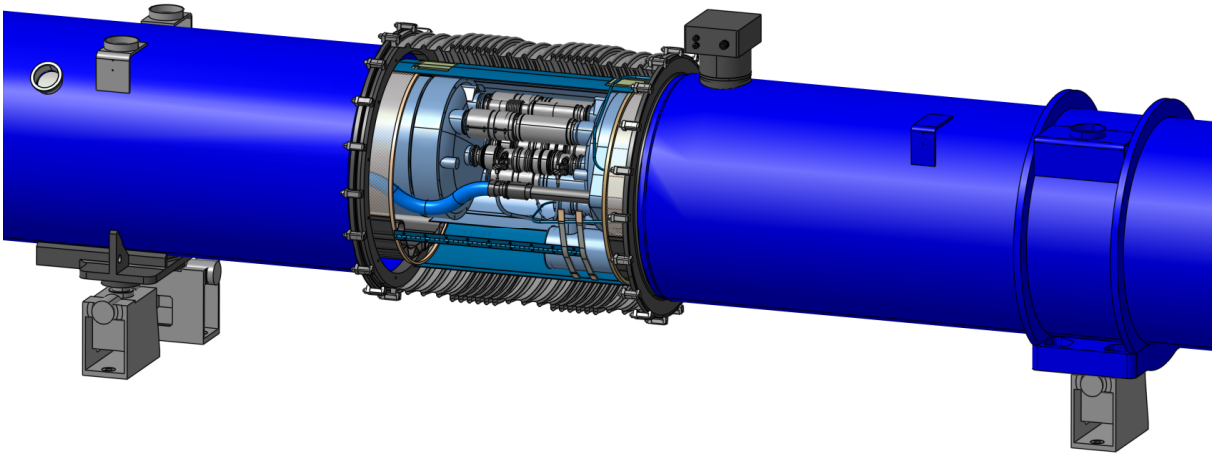

FIGURE 4.37: LHC's BM-BM interconnection. CERN CAD Database.

In the interconnections, the RF fingers and the SS bellows absorb the offset angle between the arc elements, the displacements caused by thermal variations and the dimensional variations attributed to manufacturing tolerances. The RF fingers are not directly cooled by the He, and thus, are very sensible to heat loads. Less than 1 W should be absorbed by them. In order to protect them from the SR, it has been suggested to implement a small SR absorber working at cryogenic temperatures.

The designed SR absorber is shown in Fig. 4.38. It is made of Cu to minimize its surface resistance and maximize the heat conduction. It is mounted after the BS, before the RF fingers, and cooled in series by the same cooling channel as the BS. On its left side a continuous slope coming from the sawtooth region can be seen. Such slope progressively shortens the horizontal distance between the baffle surface and the beam axis, effectively stopping the SR which would hit 1.2 m downwards. In total, 41 W of SR impact onto it. The angle of this slope has been chosen finding a compromise between the space occupied and the resulting SR power density and its contribution to the impedance, which should be minimized. At the end of the SR absorber, a smooth transition connects the profile with the shape of the BS with the RF fingers, with a round profile. The smoother the transition, the lower its impedance.

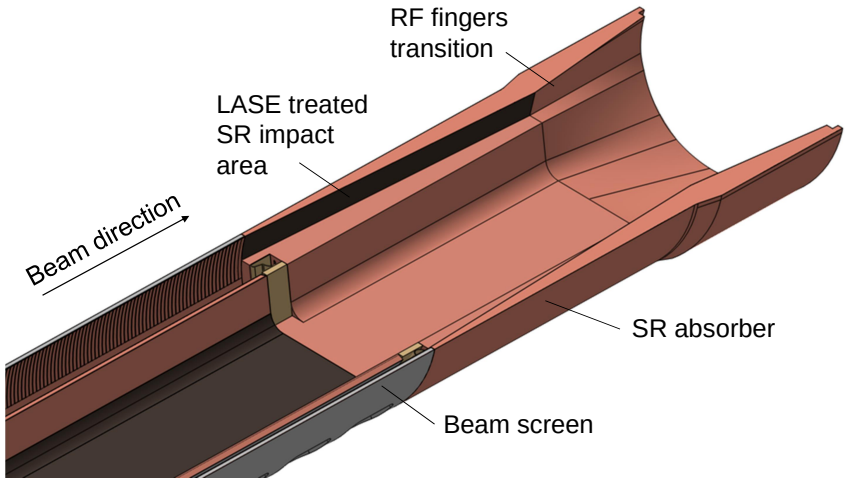

FIGURE 4.38: FCC-hh photon absorber conceptual representation [79].

The slope stopping the SR is proposed to be treated with LASE, to minimize the SR reflection and, most importantly, the photoelectron generation. In this way, the resulting SR power on both the RF fingers and SS bellows is less than 0.2 W, effectively exempting this region of requiring a dedicated cooling system and minimizing the PSD gas load.

Owing to the small diameter of the BS, the longitudinal conductance of the BS is extremely low. Along with the lack of direct pumping in this interconnection region, this translates into a very low S in the middle of the interconnection. The high outgassing value in this region generated by the high SR power on the absorber results in a very high gas density. Triggering the same amount of outgassing in areas with a

much higher pumping speed, lowers the average gas density in the arcs. Therefore, the SR power on the absorber should be kept as low as possible.

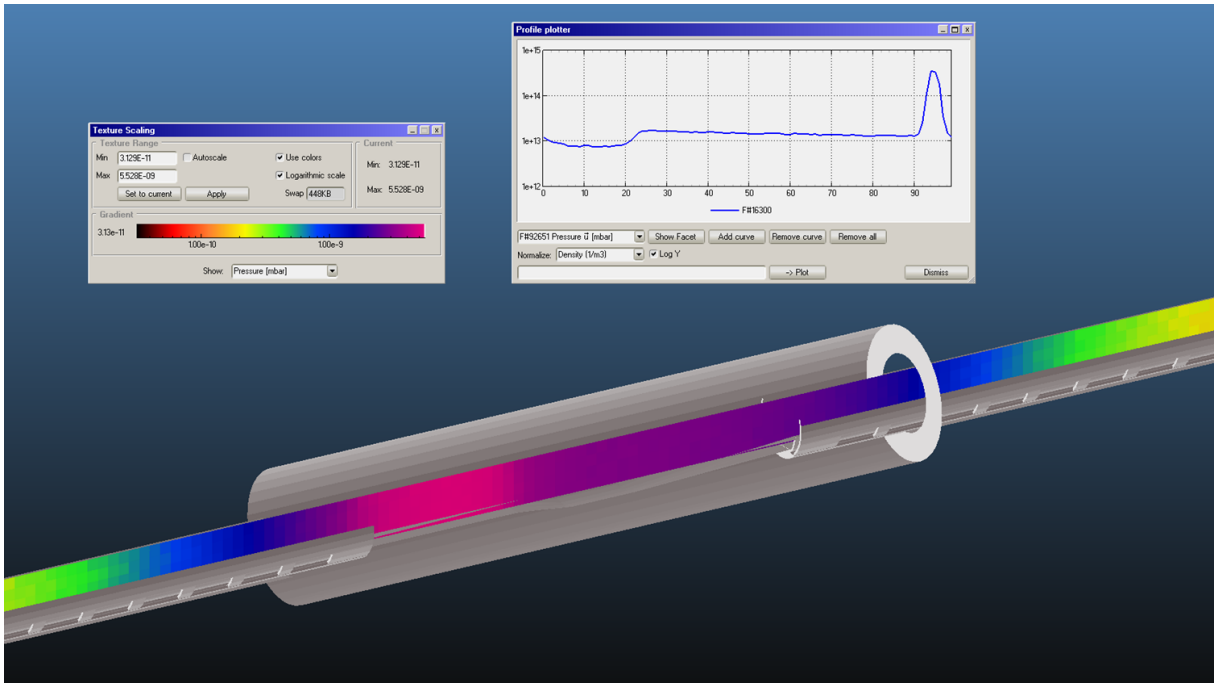

FIGURE 4.39: Gas density calculation in one of the first versions of the MB-MB interconnection.

A Molflow+ simulation of the gas density in the interconnection for one of the first design iterations is shown in Fig. 4.39. The gas density profile of the whole MB BS can also be seen. In this design, the SR absorber was stopping a considerably higher amount of SR power, resulting in a very high outgassing. A high pressure peak can be noticed, more than 20 times higher than the average pressure inside the rest of the beam pipe.

However, the proposed SR absorber can be considered as a first, conservative approach to assess the viability of the cryogenic vacuum system from a technical point of view. The 1.2 m long shadow it delivers downstream is a very conservative value. After checking the final manufacturing and alignment tolerances, this value could be decreased by lowering the height of the absorber slope. This would lower the SR power stopped, lowering the PSD gas load and the e^- cloud development in the interconnection as well.

Another cost-friendly solution would be to not use a SR absorber at all. This is possible if the pipe diameter from the end of the BS until the RF fingers-BS end transition (shown in Fig. 4.40) are larger than that of the BS, and if the alignment tolerances are low enough. The SR beam point of incidence would then jump from the end of the BS up to the second transition, which would have a decreasing diameter, missing in this way the RF fingers. The irradiated region of the transition should be treated with

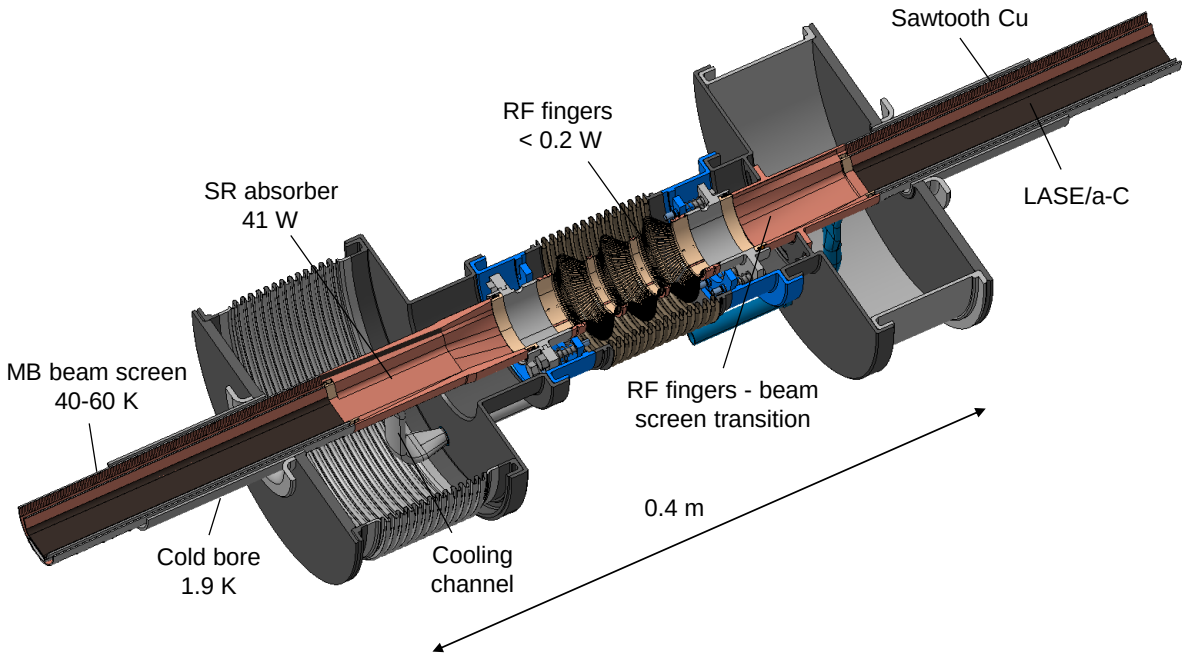

FIGURE 4.40: Conceptual design of the MB-MB interconnection for the FCC-hh, with a new design of the RF fingers. Designed by CERN TE-VSC-DLM.

LASE to avoid excessive e^- cloud development and PSD outgassing. We recommend to consider future studies on this promising approach.

4.4.3 Pumping performance

As the gas load in the FCC-hh cryogenic beam vacuum system is expected to be much higher than in the LHC, an effort has been made to maximize the pumping speed. Since the sticking probability of the CB is the same, the only means of achieving that is maximizing the conductance from the beam's path up to the CB. This has been achieved thanks to the double chamber layout of the BS, which allows a low SR and electron flux leakage through the pumping holes, and thus a larger size of them.

The resulting pumping speed is considerably higher, surpassing the LHC's even at the same temperature. It has been calculated using Molflow+. Setting an arbitrary outgassing (Q) in the studied region and reading the simulated n in the same spot, the pumping speed S is straightforward to calculate, as represented with Eq. 1.1. A detail of the run simulations are shown in Fig.4.41, for the FCC-hh and for the LHC BS.

In each image, it is shown how a particle is generated from the outgassing region (represented by a small blue dot) and bounces all over the chamber until randomly arriving to the CB, where it is pumped (represented by a red dot). The molecule trajectories are represented by the green lines. The geometry used in each case is a representative periodic length of each BS. In the transversal planes at both extremes of the structure a boundary condition is set, so that the molecules crossing the plane are

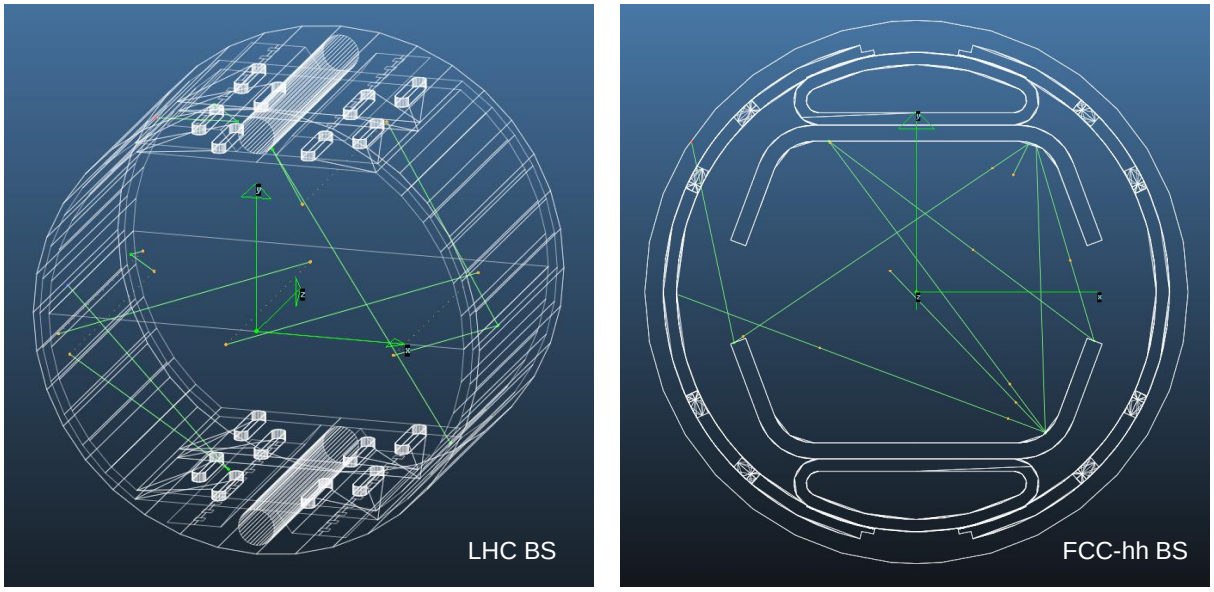

FIGURE 4.41: Detail of the Molflow+ simulations run to calculate the pumping speed of the LHC (left) and FCC-hh BS (right).

automatically teleported to the opposite plane keeping its original trajectory. These teleports are represented by the orange dots. Over the tracing millions of molecule trajectories, the program converges up to the value of S. The calculated S values are shown in Table 4.5 for different temperatures and BS regions.

TABLE 4.5: Comparison of the LHC's and the FCC-hh's pumping speeds for H_2. Calculated at the beam's path, with Molflow+ [53, 55, 56], for an infinite pipe and different outgassing (Q) sources.

	LHC	FCC-hh
Temperature window [K]	5–20	40–60
Nominal (5/40 K). Q on inner ch. [l/(s m)]	173	898
40 K. Q applied on inner chamber [l/(s m)]	489	898
40 K. Q applied on sawtooth [l/(s m)]	493	1125

The calculation done with Q applied on the sawtooth region, represents the closest case to the reality, where PSD dominates the total gas load. When Q is applied on the primary chamber, it represents a pessimistic calculation, resulting in the lowest S attainable. This would be the case in which all the gas desorption happens on the copper layer of the primary chamber, caused either by electrons or reflected photons.

At the lowest nominal temperature conditions (5 K and 40 K), the FCC-hh has a $S >$ 5 times higher than the LHC BS. At the same temperature, S is around 1.8 times higher. It is important to compare both BS at the same temperature since the gas molecules speed, and thus the pumping speed, depend on the temperature. The higher the temperature, the higher their speed, and the faster they can be evacuated from the system. Therefore, it is concluded that the new BS effectively increases the S, helping to counter

the higher residual gas density derived from the higher beam energy. Even if the resulting complexity of the FCC-hh BS is much higher than that of the LHC, it is also compatible with large scale production technologies [117] and affordable from the economic point of view, representing a very small fraction of the collider's cost [118].

4.4.4 Synchrotron radiation ray tracing

In order to assess the feasibility of the proposed BS, it is necessary to calculate among other things the thermomechanical stability and the gas density evolution. Both of these calculations need the results of the SR ray tracing in the vacuum chamber. For the thermomechanical calculations, the power map is needed. In the case of the vacuum calculations, the SR flux map is used.

A ray tracing was then performed with Synrad+ with the latest BS design. The run simulation gives as results both the flux and SR power map in all the chamber, and the spectrum of the photons arriving to the user-defined facets. A whole structure of a MB BS + a MB-MB interconnection was drawn, applying the continuous boundary conditions to emulate an infinite series of MB. No beam misalignment was taken into account. The sawtooth profile used is the one proposed for the FCC-hh, shown in Figure 4.31, with a factor of two applied in the fitted sawtooth profile to take into account the benchmark uncertainties. The beam parameters have been set to nominal.

The resulting geometrical model has 161768 vertices and 66842 facets. With this configuration, the software is able to trace the trajectories of around 10^3 photons per second, including their reflection and equivalent energy deposition in each region. All facets in the model were meshed, to be divided in different independent regions whose SR flux and power can be separately calculated. The mesh density is variable, ranging from 5 divisions per cm up to 100, applied to the facets where the SR directly impacts. This is translated into around 3.3×10^6 total cells. For Cu and SS a roughness ratio of $\tau = S_q/T = 0.006$ were assigned, according to the metrology studies on the performed samples.

The colour-coded SR power map obtained in the simulations is shown in Fig. 4.42. A similar map has also been obtained for the SR flux.

In the Figure, the photon beam trajectory is represented by the yellow line in the middle, curved owing to the magnetic field effect. Photons are emitted tangentially from it, in a forward direction. The trajectories are represented by the green lines. It can be seen how the sawtooth region, on the left baffle, and the SR absorber at the end of the structure (the protruding region) are directly irradiated, being these regions the ones with higher SR power density. The CB receives an almost negligible amount of SR, as intended by the design, and is therefore effectively protected and does not trigger a magnet quench due to the excessive heat load and prevents the condensed gas from being recycled back into the system in large amounts.

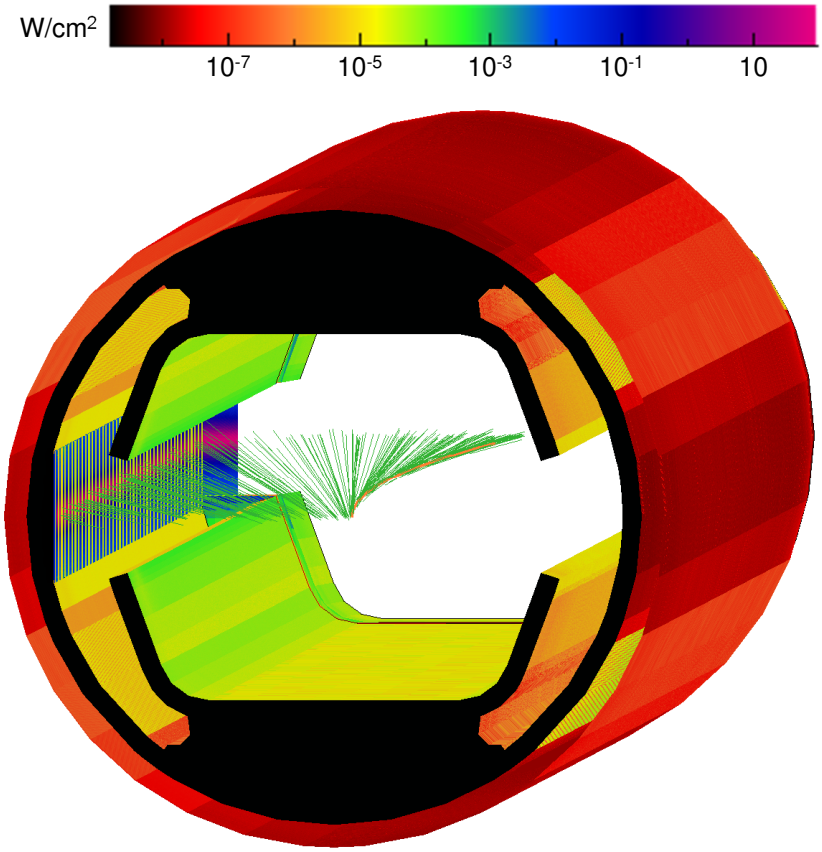

FIGURE 4.42: Absorbed SR power map in the FCC-hh BS at nominal beam parameters.

Increasing the mesh density in the regions directly hit by the SR yields better precision in the results, reaching higher power density values than the ones shown. Nevertheless, the simulation would be considerably slower and the increase in accuracy in the vacuum simulations is minimum, so a compromise was found. Other simulations were run with a higher mesh density, but only in some specific areas of the geometry (like one single tooth in the baffle or the SR absorber) since they were required for the thermomechanical simulations.

A linear power density calculation along the MB BS has also been done. It is shown in Fig. 4.43.

The highest linear power density, around 40 W/m appears at the beginning of the BS, after the initial region of shadow produced by the SR absorber. From this maximum, it decreases progressively along the BS following the beam direction until finding the SR absorber, with the exception of one small jump after the first 5 m attributed to the change of the magnetic region and corresponding angular tilt. The decay is due to the fact that a curved orbit shines its SR against a straight segment. Along the LHC BS, which is bent parallel to the beam orbit, there is a flat linear power profile (at the end of the MB).

The average power density along all the BS was found to be 29 W/m, and the length

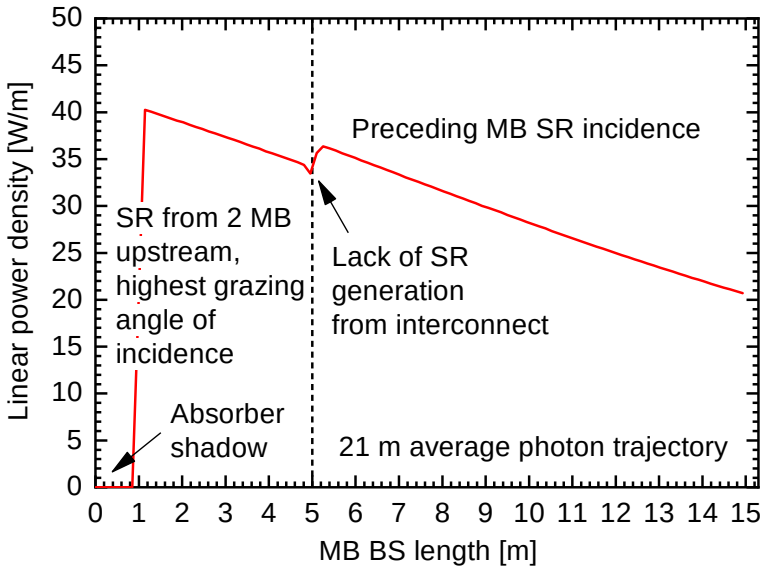

FIGURE 4.43: Linear power density of SR impinging the BS sawtooth surface, for the most irradiated MB. Nominal beam parameters.

of the average trajectory of each photon until hitting the chamber wall was found to be 21 m.

In Table 4.6 the distribution of the total SR dissipated on each MB is shown, expressing with practical numbers the same information of Fig. 4.42.

TABLE 4.6: SR power distribution per MB. The shown structure is around 15.57 m long.

Area	Power	% of total SR
Irradiated baffle	439 *W*	88 %
End absorber	50.5 *W*	10.1 %
Non-irradiated baffle	6.5 *W*	1.3 %
Inner copper primary chamber	0.6 *W*	0.1 %
Interconnection	0.1 *W*	0.02 %
Cold bore	< 0.01 *W*	< 0.01 %
Other BS areas	< 0.01 *W*	< 0.01 %
Total per arc dipole	498.7 *W*	100 %

In the simulations, the spectrum of the photons arriving to some critical regions has also been calculated. This feature is especially useful to determine the photoelectron generation (N_e) on such regions, since it depends on the photon energy, as shown with Eq. 4.15. Integrating the obtained spectrum in absolute units (not expressed in 0.1% BW) along with the photoelectron yield $Y_{ph}(E)$ would give N_e. The spectra are also useful to assess the photon energy arriving to the different areas of the BS, and estimate the $\eta_{ph}(E)$ that these photons would generate.

An example of the obtained spectra is shown in Fig. 4.44. The photon spectrum arriving to the flat, parallel Cu regions of the primary chamber (the regions between

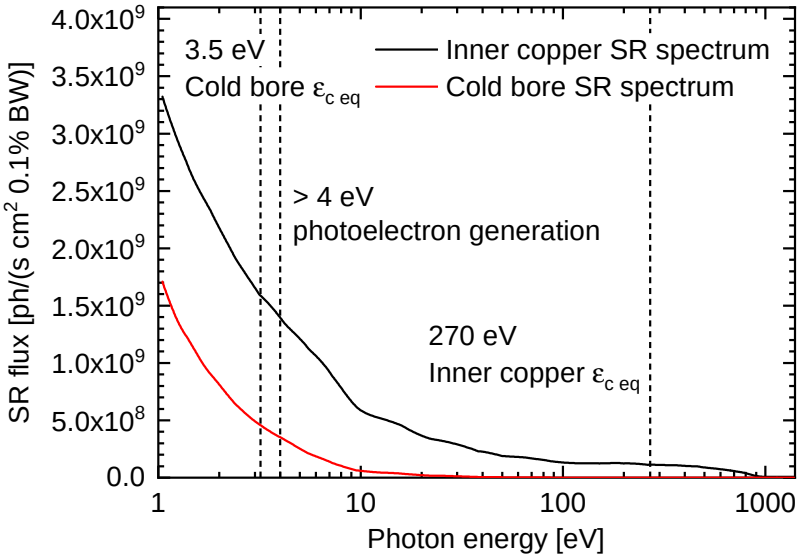

FIGURE 4.44: Spectrum of the SR arriving to the CB and to the inner chamber [79], with most part of their photon flux below Cu's work function. Calculated with Synrad+.

which the e^- cloud is developed) and arriving to the CB is shown. Both curves have been cut at 1 eV. It can be noticed how a large part of the photon flux arriving to the primary chamber carries an energy well below SS and Cu work functions, effectively keeping the e^- development and the gas desorption due to PSD and ESD within relatively low values. Its equivalent critical energy ($\varepsilon_{c\,eq}$), has been calculated to be 270 eV, much lower than the original one emitted by the proton beam. The photons hitting the CB have a $\varepsilon_{c\,eq}$ even lower, around 3.5 eV, less than the work function of SS. Therefore, this low photon energy is expected to entail negligible levels of gas load ascribed to PSD.

4.4.5 e^- cloud mitigation

As explained in Subsection 2.3.2, the secondary electron emission taking place in the BS can drive an avalanche multiplication effect, filling the BS with a cloud of electrons, the e^- cloud. The e^- cloud presence leads to a series of detrimental effects proportional to its density, such as emittance growth, transverse instabilities, heat load on the beam chamber, and a degradation of the vacuum quality. The designed BS has therefore to ensure that the e^- cloud is kept under control in order to minimize its impact on the collider's performance. To this end, the BS has to comply with two established constraints: (i) to be under the SEY multipacting threshold (a fast, general constraint, as a function of the SEY and beam parameters), and (ii) to be under the transverse instability electron density threshold (a more specific and demanding one, depending mostly on the N_e).

The multipacting threshold is the maximum value of SEY above which, independently from the value of N_e, the exponential electron multiplication starts. There are different threshold values depending on the beam parameters. The threshold values have been estimated by the EuroCirCol's WP2 team for the different bunch spacing options proposed for the FCC-hh, and for the injection and baseline beam energy. The estimations have been done with simulation studies of e^- cloud build-up with the PyECLOUD code [119, 120], using a secondary emission model [121–123] based on measurements on samples of the LHC BS [124–126]. The estimated values can be found in Table 4.7.

TABLE 4.7: SEY multipacting thresholds for build-up [127].

Bunch spacing	25 ns		12.5 ns		5 ns	
Beam energy [TeV]	3.3	50	3.3	50	3.3	50
Dipole	1.5	1.5	1.1	1.1	1.5	1.5
Quadrupole	1.1	1.2	1.0	1.0	1.1	1.0
Drift space	2.0	2.0	1.3	1.3	1.6	1.6

As shown in the table, the baseline bunch spacing, is the least demanding option, while 12.5 ns is the most demanding one. Conditioned (also called scrubbed) Cu can reach around 1.2–1.4 SEY, as displayed in Fig. 4.45. The expected range of most common electron energies, 0–485 eV [79], is also shown.

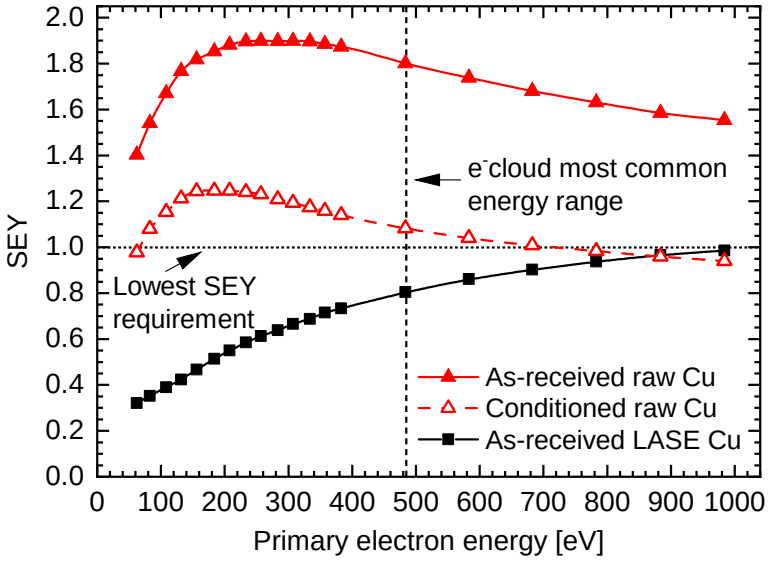

FIGURE 4.45: Comparison of the SEY of LASE [96] and of raw Cu [49].

The lowest SEY requirement for the baseline option is 1.1, in quadrupoles. It is below the lowest attainable SEY of Cu, so it is necessary to use a SEY mitigation solution. It is important to clarify that, when analysing the SEY curve, the reference value taken is the maximum of the curve within the displayed range of energy. When saying the

lowest, it means the maximum value of the lowest, most conditioned curve. For the dipole magnets, the MB, if the 12.5 ns option was discarded, scrubbed Cu could be used, without any SEY mitigation treatment. As for the SEY values of the drift space, the calculation is indicative, since many simplifications were considered in its calculation and no magnetic field was taken into account at all [85]. As shown in Fig. 4.45, LASE can achieve SEY values under 1 even without surface conditioning, and well below 1 with it. In this case, its properties are above specification. Lowering the LASE ablation rate, would still meet the SEY requirements while featuring a better surface conductivity. It is therefore relevant to adjust the properties of this treatment to match optimally the SEY with a reasonable margin of security, not too high. a-C, the baseline mitigation solution for the FCC-hh, can also lower the SEY below one with a layer of just 6 nm thickness [128].

Transverse instabilities can happen if the electron density in the chamber is high enough. The maximum allowable electron density ($\rho_{e,th}$) can be estimated using Eqs. 4.16–4.19 [26, 129]:

$$\rho_{e,th} = \frac{2\,\gamma\,\nu_s\,\omega_e\,\sigma_z/c}{\sqrt{3}\,K\,Q\,r_p\,\beta_{x,y}\,L} \tag{4.16}$$

where γ is the Lorentz factor, ν_s is the synchrotron tune, $\sigma_{x,y,z}$ are the RMS transverse beam sizes and bunch length, c is the speed of light, r_p and r_e are the classical proton and electron radii, $\beta_{x,y}$ are the beta functions and L is the length of the machine along which the e^- cloud extends. ω_e, K and Q are defined as:

$$\omega_e = \sqrt{\frac{\lambda_p\,r_e\,c^2}{\sigma_y\,(\sigma_x+\sigma_y)}} \tag{4.17}$$

$$K = \omega_e\,\sigma_z/c \tag{4.18}$$

$$Q = min(\omega_e\,\sigma_z/c, 7) \tag{4.19}$$

where λ_p is the bunch line density. In the FCC-hh, the threshold electron density results in 6×10^{10} e^-/m^3 at 3.3 TeV (injection) and 3.6×10^{11} e^-/m^3 at 50 TeV (collision energy) [79].

Below the multipacting threshold, the electron density in the chamber is approximately proportional to the N_e on the areas where the e^- cloud build-up happens. Figure 4.46, an example of the calculated electron density vs N_e, illustrates this dependence. It has been calculated by the WP2.To prevent surpassing the threshold, it is advisable to keep N_e in the inner chamber well below 1×10^{12} $e^-/(cm^2\,s)$.

N_e can be calculated using Eq. 4.15, using as inputs the ray tracing results and the measured experimental data in BESSY-II's. The maximum values calculated at nominal beam parameters, if LASE is applied, are 2.3×10^{10} $e^-/(cm^2\,s)$ for dipoles (on the critical

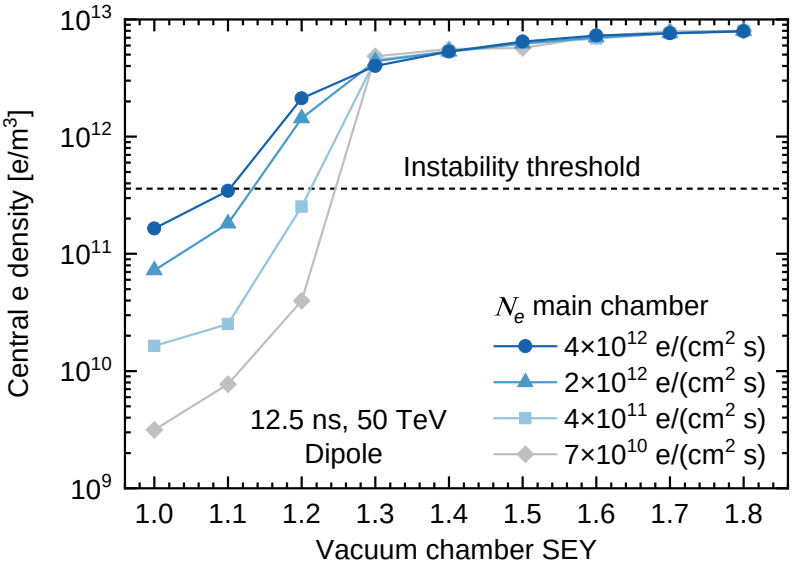

FIGURE 4.46: Calculated electron density in the beam region depending on photoelectron generation rate and SEY, in a dipole chamber with 12.5 ns 50 TeV beam. Taken from [79].

build-up areas, top and bottom of the BS) and 1.6×10^{11} e$^-$/(cm^2 s) for quadrupoles (on the rounded corners of the primary chamber). If untreated copper is used, the calculated values are 1×10^{11} e$^-$/(cm^2 s) and 6×10^{11} e$^-$/(cm^2 s), respectively (see Table 4.4). In all cases N_e has an associated electron density under the instability thresholds calculated by the WP2 [85, 127, 130].

This low value is achieved thanks to the high SR absorption properties of the sawtooth profile, which lower considerably the number of photons reaching the critical areas, and most importantly, their $\varepsilon_{c\,eq}$. This good performance would be impossible with the other contemplated options to handle the SR (see Table 4.3). During the beam's injection, the lower photon flux (15 times lower, see Eq 4.2) and lower ε_c (1.23 eV, much lower than copper's work function) entail negligible N_e values when compared with the collision energy mode, rendering it the only concern. The suggested option of treating the rounded edges of the sawtooth pattern with LASE, or using a sawtooth profile not only on the irradiated baffle, but also on the other side, would further lower N_e.

Electron density plots in an LHC like BS can be found in Fig. 4.47. It can be seen how the electron trajectories follow the magnetic field lines. In the drift space case, no magnetic field has been taken into account. The double strip shape in the dipole case is explained with the point where the energy gain by the bunch pass coincides with the highest SEY of the material. Knowing the regions where the electrons will impinge, it is possible to design the BS region to be treated with LASE. These regions are shown in Fig. 4.47, as well. In this way, the treated region, and thus the impact on the impedance budget, is minimized.

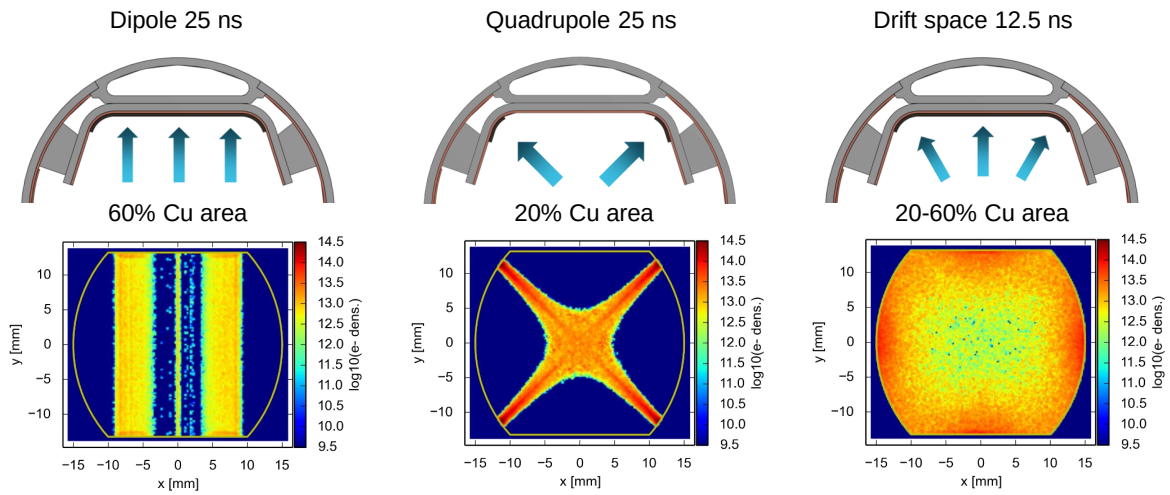

FIGURE 4.47: Proposed layout of the LASE coating in an old version of the FCC-hh BS according to the magnetic field. The thickness of the LASE regions has been magnified. Electron density plots courtesy of L. Mether.

4.4.6 Heat load on the cold bore

40% of the cold mass thermal budget of each magnet is allocated to the heat load coming from inside the CB, i.e. 0.3 W/m per aperture [75]. From this percentage, most of it corresponds to the nuclear scattering power, calculated with Eq. 4.13. The other heat sources are the heat conduction through the BS-CB supports (proportional to the BS temperature), the BS thermal radiation, and the SR leaked power. To calculate the contribution from the conduction and thermal radiation sources, a thermal analysis was done by the WP4 mechanical design team, using the *Heat Transfer in Solids* and the *Heat Transfer with Surface-to-Surface Radiation* modules of COMSOL Multiphysics [131]. The complete analysis can be found in [79, 132]. An example of the obtained results is presented in Fig. 4.48.

The fraction of SR power leaking into the BS inner part has been found via Monte Carlo ray tracing simulations (see Fig. 4.42). Thanks to the sawtooth on the baffle, the leaked power is even lower than that of the thermal radiation at cryogenic temperatures. All the found heat loads are displayed in Table 4.8.

TABLE 4.8: Estimated heat loads on the cold mass per beam aperture in the hotter section of the BS. Nuclear scattering calculated as an average along the arc cell. Nominal beam parameters.

Heat source	Value	Percentage
Nuclear scattering	178 mW/m	69.8 %
Conduction through BS supports	67.7 mW/m	26.5 %
BS thermal radiation	8.9 mW/m	3.5 %
Leaked SR power	0.5 mW/m	0.2 %
Total	255.1 mW/m	100 %

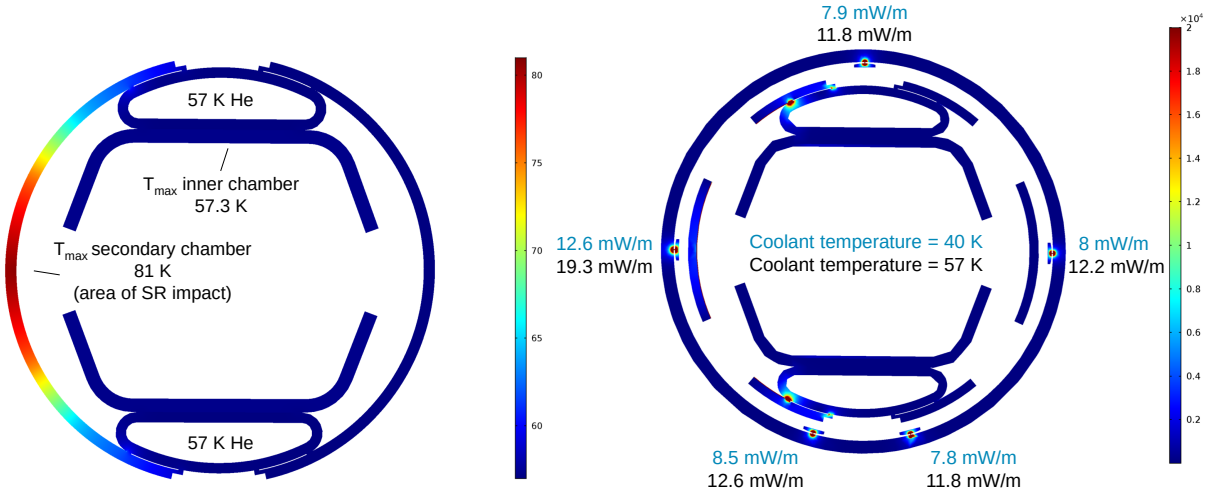

FIGURE 4.48: Left- BS temperature map for nominal beam parameters and a He temperature of 57 K, the maximum expected one. Right - Heat conduction through the BS supports to the CB, for an He temperature of 40 K (light blue) and 57 K (black). Taken from [74].

It can be seen that the total heat load is situated well within the budget, as intended. The shown conduction and thermal radiation are the ones belonging to the section of the BS with the highest heat load, close to the beginning of the MB. The nuclear scattering has been calculated as an average, for all the arcs, and for the maximum gas density allowed. Over time, the cryogenic beam vacuum density is expected to be much lower than the maximum one, so in average, this value will decrease. Nevertheless, the heat load budget is expected to be surpassed at some particular points owing to the high variability of the nuclear scattering power deposition along the cell elements. Considering only the nuclear scattering, the cold mass of the most impacted dipole can receive up to 278 mW/m [78].

4.5 Analysis of the beam induced vacuum effects

This section details the generation process of each beam induced vacuum effect and all the steps taken to calculate their partial gas density. The gas density results are shown at the end, in Section 4.6. All the calculations have been carried out for the baseline chamber design.

For the sake of clarity, Eq. 2.4 is represented here in a simpler way, with Eq. 4.20:

$$n_j = \frac{\overbrace{\dot{\Gamma}_{ph}\left(\eta_{ph,j}+\eta'_{ph,j}\right)}^{\substack{photon\text{-}stimulated\\ desorption}} + \overbrace{\dot{\Gamma}_{e}\left(\eta_{e,j}+\eta'_{e,j}\right)}^{\substack{electron\text{-}stimulated\\ desorption}} + \overbrace{\sum_k\left\{\left(\eta_{i,k,j}+\eta'_{i,k,j}\right)\sigma_{i,k}\left(I/e\right)n_j\right\}}^{\substack{ion\text{-}stimulated\\ desorption}} + \overbrace{Aq_j}^{\substack{thermal\\ outgassing}}}{S_j} \tag{4.20}$$

This equation summarizes in a conceptual way the generation process of the beam induced effects along with the thermal outgassing, which does not depend directly on the beam's presence. The terms appear ordered according to their impact on the beam's lifetime. Each effect can be divided into two different terms, the primary and secondary. The primary term represents the gas desorption from the material and its primary adsorbed layer of contaminants. The secondary term, noted with a ', represents the desorption of the gas molecules condensed on the surface, also called recycling effect. At RT, or for surfaces being constantly cleaned by the SR or electrons, only the primary term applies.

4.5.1 Primary photon stimulated desorption (PSD)

This effect is the one with the largest impact on the beam lifetime. It is also the most studied one, as it is the only effect occurring in electron synchrotrons. Knowing the $\dot{\Gamma}_{ph}$ map along the vacuum chamber (in area units), and knowing the η_{ph} of the irradiated material, the gas load due to PSD can be easily calculated for any required photon dose. The $\dot{\Gamma}_{ph}$ map has been calculated using Synrad+. It is directly obtained in photons per cm^2 and per second, as explained in [79]. Synrad+ supports the exportation of the obtained data to Molflow+, allowing a direct calculation of the resulting gas density in the modelled vacuum chamber using a $\eta_{ph,j}$ added by the user as an input, for any specified beam dose. For the η_{ph} of Cu and SS P506 [31] (the BS's materials) at the FCC-hh BS conditions, 40–60 K and for a SR with ε_c of 4.3 keV, there is neither exact nor similar experimental data available. Close values of η_{ph} are expected to be acquired at BESTEX in the future, but for a bit higher temperature (77 K, using liquid N_2) and higher ε_c, around 6.2 keV. Lacking for the time being the necessary data, η_{ph} has been numerically estimated starting from the closest published values and then scaling them according to the variation in critical energy and/or temperature. For Cu, data from the LHC PSD experiments have been chosen [133], taken at 77 K and with a SR ε_c of approximately 50 eV. For P506 SS, lacking suitable cryogenic experiments, data at 3.75 keV ε_c and RT [134] has been chosen. It has been done so because of the lack of bake-out and because of the closeness of its ε_c to the FCC-hh's one (4.3 keV). That being said, the lack of suitable cryogenic data for SS is not an issue. Being Cu the directly irradiated material, the molecular yield of SS is not expected to contribute much to the total gas load in the chamber. The complete process used to convert these chosen yields to the theoretical ones for the FCC-hh conditions is hereunder detailed.

For the most common materials used in vacuum technology, η_{ph} spans the range of 10^{-3}–10^{-5} molecules/photon, with H_2 usually featuring the highest values. η_{ph} decreases over the photon and electron dose that the surface receives. It is usually plotted separately for each species on a log-log scale, starting with a high and flat region until a cut-off value of about 10^{19}–10^{20} ph/m, corresponding to the time when the chemical transformation of the surface starts (see Fig. 4.51). After this initial plateau, the curve

continues with a straight line on the log-log plot, described by the power law shown in Eq. 4.21 [27, 56]. No change of slope is usually observed for doses up to 1×10^{23} ph/m.

$$\eta_{ph}(D) = \eta_0 \, D^a \tag{4.21}$$

η_0 is defined as the initial yield, D is the integrated photon dose, expressed usually in ph/m, and a is the decaying slope (in log-log scale), with values usually ranged between -0.6 and -1.

The standard units of photon dose, in ph/m, even if useful for quick approximations, are nonetheless not valid as an input for Molflow+. They also have little physical meaning since PSD is a surface effect and should be expressed in flux/area units instead of flux/length. As such, the chosen η_{ph} values have been first of all converted from ph/m to ph/cm^2.

The conversion methodology was initially proposed in [56], where an original experiment built to acquire the η_{ph} values of the irradiated sample was recreated in Synrad+ to know the proportion of irradiated sample area per sample length. With this proportion, one can easily convert the available η_{ph} values into the needed ones. A similar process has been followed in this study for the Cu and SS P506 chosen data. The original experiments from which these data were taken have been recreated in Synrad+ and the area of irradiation has been measured. The recreation of the original experiment to acquire the SS η_{ph} data is shown as an example in Fig. 4.49.

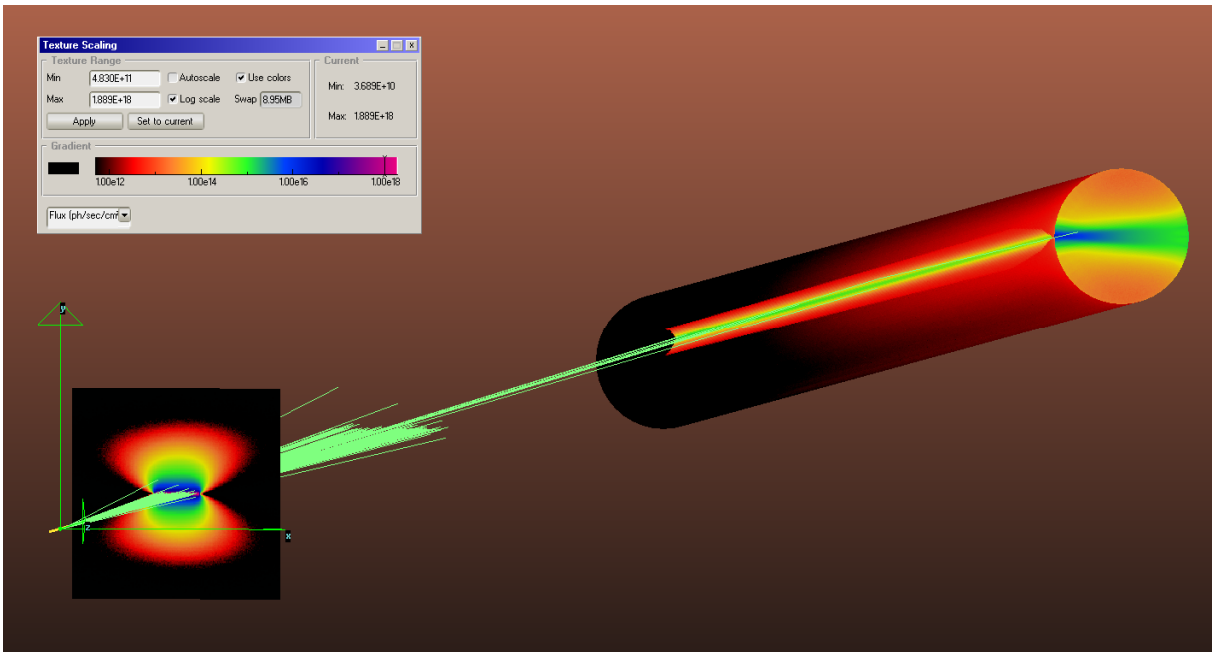

FIGURE 4.49: Recreation in Synrad+ of the DCI PSD experimental setup [134].

SR reflection has also been taken into account, filtering out the areas receiving small amounts of SR power. For SS [134] it has been found that around 70 ph/m linear dose

of the published data correspond to 1 ph/cm^2 of surface dose, the same value as [56]. For Cu, this factor has been found to be much larger due to a higher SR beam height of the original experiment and consequently a larger irradiated chamber area. However, it has been decided to take the same factor as SS as a conservative approach. That said, despite of the little accuracy that this approach might entail, it is relevant to highlight the fact that for high photon doses the error in the estimations is minimized due to the general convergence of η_{ph} in common technical materials.

Next, the base values of the selected data have been increased to match the higher ε_c of the FCC-hh SR (see Fig. 4.4). η_{ph} increases along with ε_c because, on one hand, a larger percentage of the SR is emitted with an energy higher than the work function of the material (≈ 4 eV for Cu), being able to trigger a larger photoelectron emission in the surface. On the other hand, and for the studied energy range, higher photon energies mean higher photoelectron energies, more chances to interact with the contaminant molecules present on the surface and a higher number of secondary electrons, which in turn can desorb larger amounts of gas.

The dependence of η_{ph} on ε_c was found in the past to fit the following empirical expression [135]:

$$\eta_{ph} = C\,{\varepsilon_c}^b \tag{4.22}$$

where C and b are positive constants different for each gas species and material. b is usually between 0.7 and 1.2.

Fig. 4.50 shows an example of the dependence of η_{ph} on ε_c using experimental data from the literature [135, 136] for baked Cu measured at RT. The shown proportions have been used to match the η_{ph} of the chosen sources to the ε_c of the FCC-hh.

The chosen experimental data correspond to samples irradiated with glancing SR incidence, yielding outgassing rates much higher than with a perpendicular incidence (as it happens for the Y_{ph}), which is the case of the baseline FCC-hh BS. The real η_{ph} is expected to be lower, then, making this approach even more conservative.

For the SS data the dependence of η_{ph} over the temperature published in [137] has been used to convert them to η_{ph} at 77 K, as a conservative estimation.

Next, the obtained η_{ph} for each gas species were exported to Moflow+ along with the calculated SR flux map to obtain the partial gas densities.

By combining Eqs. 2.3–2.5 one can rewrite Eq. 4.20 for primary PSD in a more compact form:

$$n_{H_2\,eq} = \frac{\dot{\Gamma}_{ph}}{S_{H_2}}\,\eta_{ph,H_2\,eq} \tag{4.23}$$

where

$$\eta_{ph,H_2\,eq} = \eta_{ph,H_2} \sum_j \left(\frac{\eta_{ph,j}}{\eta_{ph,H_2}} \frac{\sigma_j}{\sigma_{H_2}} \sqrt{\frac{M_j}{M_{H_2}}} \right) \tag{4.24}$$

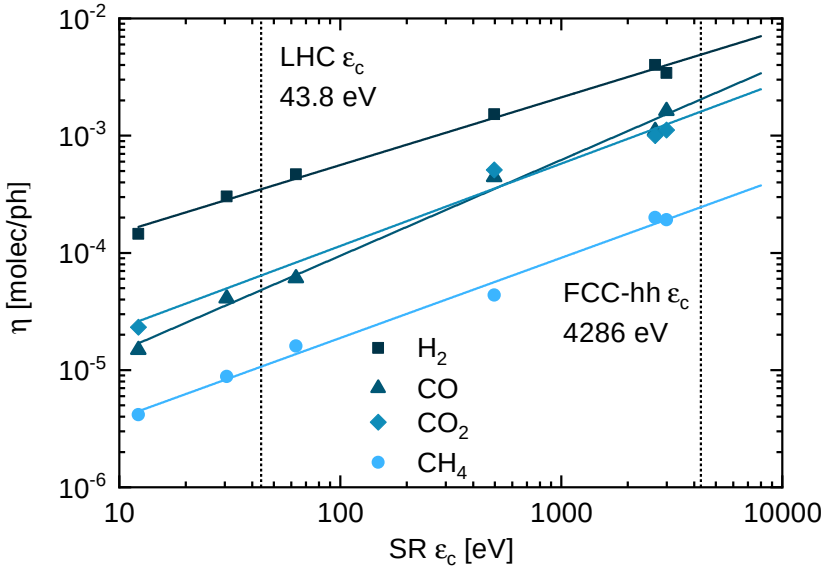

FIGURE 4.50: η_{ph} dependence on ε_c for RT baked Cu measured at a common dose of 2.5 $\times 10^{20}$ ph/m [135, 136].

and, simplifying:

$$\eta_{ph,H_2\,eq} = \eta_{ph,H_2}\, K_{\eta_{ph}} \tag{4.25}$$

Using Eq. 4.24, the estimated $\eta_{ph,j}$ values have been converted to $H_{2\,eq}$ units ($\eta_{ph,H_2\,eq}$) to allow a direct assessment of the properties of each material with regard to their impact on the beam lifetime. $\eta_{ph,H_2\,eq}$ can also be understood as a conversion of all different molecules into H_2 ones (see Table 4.9) which allows to approximately obtain the same value of $n_{H_2\,eq}$ as if we separately added together all the partial n_j, following Eq. 2.3.

The coefficient $K_{\eta_{ph}}$ varies with the photon dose, choice of material, applied treatments, etc. For example, with the photon dose its variation is: from 8 to 5 for Cu irradiated with ε_c = 50 eV at 77 K [133], from 50 to 30 for baked Cu irradiated with ε_c = 3.75 keV at RT [138], and from 50 to 20 for non-baked SS irradiated with ε_c = 3.75 keV at RT [134] (approximated values). This shows that the weight of H_2 in the total beam-gas interaction ratio can be insignificant compared to the other gas species such as CO_2 and CO.

The calculated $\eta_{ph,H_2\,eq}$ values for Cu and SS have been plotted in Fig. 4.51 and compared with other $\eta_{ph,H_2\,eq}$ in the literature.

The resulting curves are quite similar for both Cu and SS, being placed between the data taken at RT with a high ε_c and at 77 K with a low ε_c, as expected. Even if η_{ph,H_2} does not decrease much when lowering the temperature (by a factor of two, for 45.3 eV ε_c and normal incidence [137]), η_{ph,CO_2} can be lowered by a factor of 30. Being each CO_2 molecule equivalent to $\approx$ 65 molecules of H_2 (see Table 4.9), $\eta_{ph,H_{2\,eq}}$ is dramatically lowered.

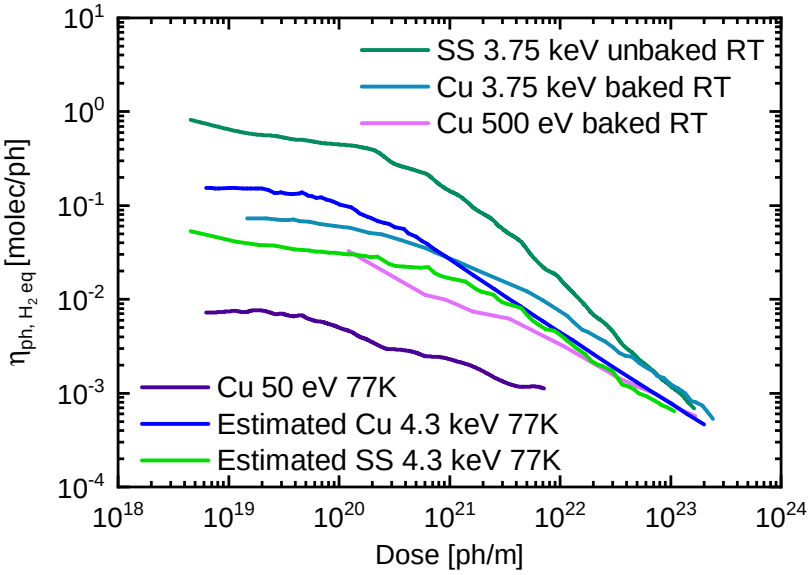

FIGURE 4.51: η_{ph,H_2eq} values for common vacuum chamber materials [133, 134, 138, 139] compared with those of the FCC-hh at 77 K and for a ε_c = 4.3 keV.

TABLE 4.9: Equivalences of the different gas species to H_2 .

Gas species (j)	σ_j/σ_{H_2} [28]	S_{H_2}/S_j	Total $H_{2\,eq}$
H_2	1	1	1
CH_4	6.0	2.8	16.8
CO	9.0	3.7	33.5
CO_2	13.9	4.7	64.9

It can also be observed how most of the RT curves end up converging to the same yield after reaching a dose of approximately 1×10^{23} ph/m, when the surface is traditionally considered conditioned. This is thought to be ascribed to the gas/chemical contaminants depletion and to the growth of a sp^2 carbon layer on the surface [140, 141], resulting in a lower photoelectron emission. The growth of the sp^2 carbon layer would be translated into similar values of Y_{ph} at the original surfaces.

4.5.2 Secondary photon stimulated desorption (PSD')

It is known that the total PSD molecular yield increases along with the gas coverage present on the irradiated surfaces. The gas molecules condensed on a surface are released back into the system when high energy photons impact onto it, presenting desorption rates much higher than those of a bare surface. When the condensed layer disappears, the PSD molecular yield goes back to its original value η'_{ph}. Such desorption, called recycling, is represented by the secondary molecular yield (η'_{ph}). It should always be taken into account during the design of a cryogenic vacuum system. Besides the interception of the heat load at higher temperatures, the recycling effect is another

reason for using a beam screen, since the continuous electron and photon impacts on the 1.9 K pumping surfaces would remove the gas being condensed, not allowing the coverage to grow and rising the gas density in the system over time until eventually surpassing the established limit of gas density.

In the calculations only the η'_{ph} of the CB, at 1.9 K, has been taken into account. The gas coverage in the primary chamber has been considered to be in equilibrium, with a coverage under the monolayer, balanced by the constant removal of adsorbed gas by the scattered SR, impinging electrons and ions and by the sticking probability that the surface presents at the defined range of temperatures [51].

In the proposed design of the vacuum chamber, the CB never gets directly irradiated by the SR beam. However, around 1 % of the total emitted photon flux emitted above 1 eV succeeds in reaching the CB through the pumping holes. However, since high energy photons have a very low reflection probability for a perpendicular incidence, the equivalent critical energy ($\varepsilon_{c\,eq}$) of the photon flux reaching the cold mass is extraordinarily low, less than 3.5 eV. Fig. 4.44 shows the calculated energy spectrum of the SR arriving to the LASE regions of the primary chamber and to the CB, cropped at 1 eV, where it is possible to see the low energy of the SR arriving to the bore, mostly in the range of visible and UV. In terms of SR power, the simulations show that less than 0.01 % of the total would arrive to the CB.

To calculate the gas load associated to PSD', the evolution of the surface coverage has been first estimated for a period of two years. This is the established time in the LHC between cold mass warm-ups, used to regenerate the CB. As a conservative estimation, and to simplify the calculations, it has been considered that all the gas desorbed inside the BS due to PSD and ESD is uniformly accumulated on four CB strips next to the pumping holes. Each one of this defined regions is around 10 mm wide with a sticking probability of 1. In reality, the gas desorbed from the CB could be distributed all over its surface, so we can consider that the followed approach is a worst case one. The calculated gas coverages are shown in Fig. 4.52.

To each gas coverage value a η'_{ph} has been assigned using experimental data from the literature [143]. These values are shown in Table 4.10 for a particular time frame. It can be noticed that H_2 is the gas most easily desorbed, presenting a η'_{ph} almost 3 orders of magnitude higher than its η_{ph}. Its η'_{ph} does not vary in excess after reaching the monolayer ($\approx 3 \times 10^{15}$ molecules/cm^2 [144]). The rest of the gas species have a more variable η'_{ph}, but even after two years of operation, they are not expected to reach a η'_{ph} of 10^{-3} molecules/photon. Therefore, the composition of the recycled gas would be mainly H_2 for more than a 90 %.

With the calculated yields and the $\dot{\Gamma}_{ph}$ found in the ray tracing simulations, the recycling gas load can be easily calculated, as shown in Eq. 4.20. It is concluded that, thanks to the sawtooth profile applied on the SR impact region, the SR power reaching the CB is kept within safe values and does not imply an excessive desorption of the condensed gas.

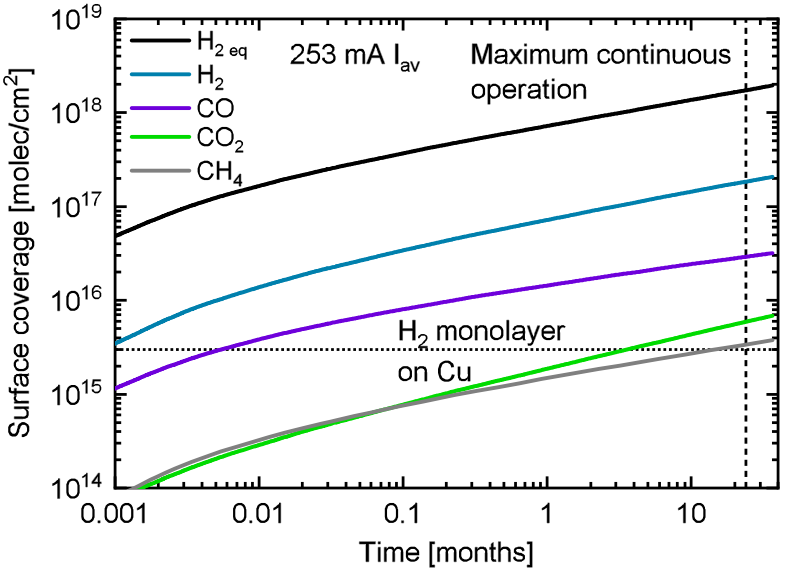

FIGURE 4.52: Worst case gas coverages on the CB areas next to the pumping holes, plotted over time for a continuous operation with nominal beam parameters during Phase 1 [142].

TABLE 4.10: η'_{ph} for different time intervals, as interpolated from the experimental data published in [143] and calculated for the coverage values shown in Fig. 4.52.

Gas species (g)	1 week	1 month	1 year	2 years
H_{2eq}	0.53	0.54	0.60	0.61
H_2	0.51	0.51	0.55	0.56
CO	3.3×10^{-4}	3.7×10^{-4}	5.2×10^{-4}	5.9×10^{-4}
CO_2	1.3×10^{-4}	1.6×10^{-4}	3.2×10^{-4}	4.2×10^{-4}
CH_4	3.4×10^{-4}	3.8×10^{-4}	5.3×10^{-4}	6.2×10^{-4}

It is also relevant to highlight that the experiment from which the η'_{ph} data are taken was performed with a ε_c of 284 eV, far higher than the $\varepsilon_{c\,eq}$ of the photons arriving to the CB. Such data have been chosen since no data for a lower ε_c are available in the literature. To be conservative, these data have not been reduced to match the $\varepsilon_{c\,eq}$ of the SR arriving to the CB. Future experiments will be necessary to properly asses the stability of the condensed gas at the energy range of the leaked SR.

As for the photocracking effect [145, 146], process where the adsorbed CO_2 and CH_4 dissociate into CO + O_2 and C + H_2 due to their interaction with the SR, it has not been taken into account in the calculations. Most of the photons arriving to the CB have an energy lower than the necessary value to break the chemical bonds, so this effect is not expected to influence the gas composition in a high extent. Moreover, part of the C present in the dissociated molecules is not expected to be released as a gas, lowering the total H_2 equivalence of the released species. Not taking this effect into account consequently results in a more conservative scenario.

Another effect which would take place is the gas recycling by means of the thermal radiation coming from the BS. This phenomenon was reported to prevent the saturated vapour pressure to go below 10^{-10}–10^{-11} mbar, without any observed dependence on the BS temperature within 20–100 K [147]. However, such behaviour was ascribed to the surfaces held at RT, not to the sample. Therefore, since the warmest region in the vacuum chamber with direct line of sight of the CB is not expected to go above 81 K (see Fig. 4.48), this effect is not expected to entail a significant impact on the beam lifetime.

4.5.3 Electron stimulated desorption (ESD)

As previously seen, the e$^-$ cloud effect is expected to be suppressed in the FCC-hh thanks to the application of LASE (the preferred and hereby studied option) and/or a-C on the BS.

Even if the electron impingement rate ($\dot{\Gamma}_e$) on Cu layer of the primary chamber is considerably low, it can still trigger some non-negligible gas desorption through ESD. The ESD contribution to the total gas load must then be taken into account when calculating the gas density.

The ESD gas load can be calculated multiplying η_e by $\dot{\Gamma}_e$ (see Eq. 4.20). An estimation of η_e for Cu at cryogenic temperature and with electron energy of 300 eV can be found in [148]. Lacking data for Cu LASE, such values have been conservatively chosen. η_e depends on the electron energy [149] following the same empirical expression as η_{ph} (Eq. 4.22). η_e is usually proportional to η_{ph} and Y_{ph}. LASE's η_{ph} has been found to be much lower than untreated Cu during the latest runs in BESTEX [66], as well as its Y_{ph} [108–110]. Consequently, LASE's η_e is expected to be lower than Cu's, making safe to use the data found in [148].

TABLE 4.11: Worst case of $\dot{\Gamma}_{ph}$ (calculated using pessimistic sawtooth reflectivity properties) above 4 eV and subsequent N_e on different BS regions. 50 TeV, 500 mA beam. Inner chamber e$^-$ cloud build-up areas and photon absorber are considered to be treated with LASE. Rest of the showed regions are OFE Cu.

Beam screen area	Γ_{ph} [ph/(cm^2 s)]	N_e [e$^-$/(cm^2 s)]
SR absorber central region	4.0×10^{16}	5.9×10^{15}
Sawtooth stopping facets	1.8×10^{16}	2.4×10^{15}
SR beam tails screen	1.6×10^{13}	8.7×10^{11}
Interconnection non-SR areas	1.2×10^{13}	5.0×10^{11}
Quad e^- impact regions	9.4×10^{12}	1.6×10^{11}
Dip e^- impact regions	1.9×10^{12}	2.3×10^{10}

$\dot{\Gamma}_e$ on the primary chamber was calculated by the WP2 with the PyECLOUD code [119, 120] for 1–1.8 SEY and different bunch spacing options, and nominal beam parameters. $\dot{\Gamma}_e$ depends directly on the photoelectron generation rate, N_e, which is directly calculated with $\dot{\Gamma}_{ph}$ and Y_{ph}, using Eq. 4.15. The N_e results for some representative BS areas are shown in Table 4.11.

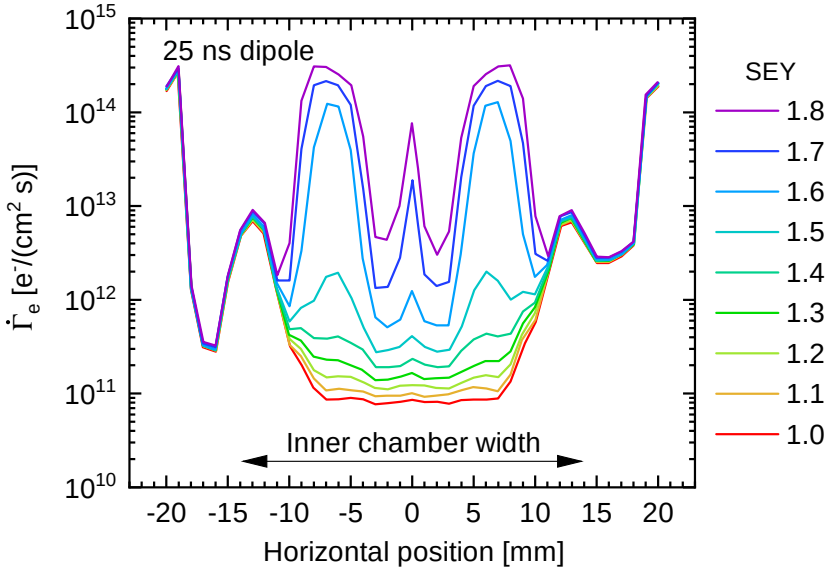

FIGURE 4.53: Horizontal projection of $\dot{\Gamma}_e$ in a dipole FCC-hh BS with a 16 T magnetic field, as a function of the SEY. Nominal beam parameters. Taken from [74].

The areas which influence the most the magnitude of $\dot{\Gamma}_e$ are the regions close to the beam which delimit the magnetic field lines [150]. The N_e triggered on these areas dictates the value of $\dot{\Gamma}_e$, so they should be the ones treated for SEY mitigation and protected the most from SR incidence.

The found $\dot{\Gamma}_e$ values are presented in Figs. 4.53, 4.54 and 4.55, for dipoles, quadrupoles and drift spaces between dipoles, respectively.

These Figures show $\dot{\Gamma}_e$ projected on the horizontal plane of the BS. The abscissa axis represents the horizontal width of the BS, whose inner radius, measured in the secondary chamber, is 19.425 mm. The point x = 0 mm represents the vertical plane where the proton beam is positioned. These data have been used in Eq. 4.20 to calculate the ESD gas load for 25 ns.

For dipoles and quadrupoles, a SEY = 1 and the Y_{ph} of LASE found at BESSY-II [108] have been used. For the drift spaces between dipoles, the SEY has been set to 1.4. The Y_{ph} data used were also obtained from BESSY-II's experimental run. No magnetic field has been considered in the drifts as a conservative scenario, even if the magnetic field in the magnets interconnections is far from being negligible. $\dot{\Gamma}_e$ has been generally found to be considerably low in dipoles and quadrupoles for a SEY $\leq$ 1.0, the maximum

values of the proposed LASE option for the FCC-hh BS [102] with the 0–1000 eV range of electron energy.

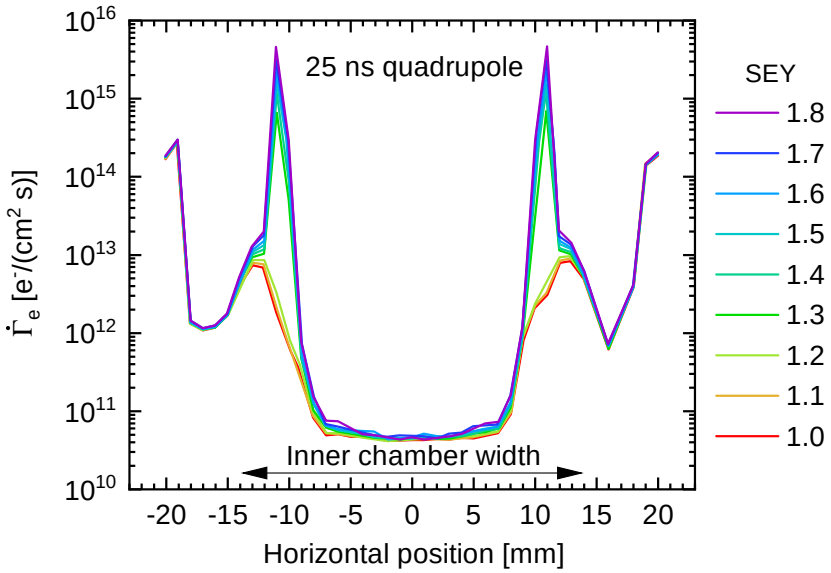

FIGURE 4.54: Horizontal projection of $\dot{\Gamma}_e$ in a quadrupole FCC-hh BS with a 360 T/m magnetic field, as a function of the SEY. Nominal beam parameters. Taken from [74].

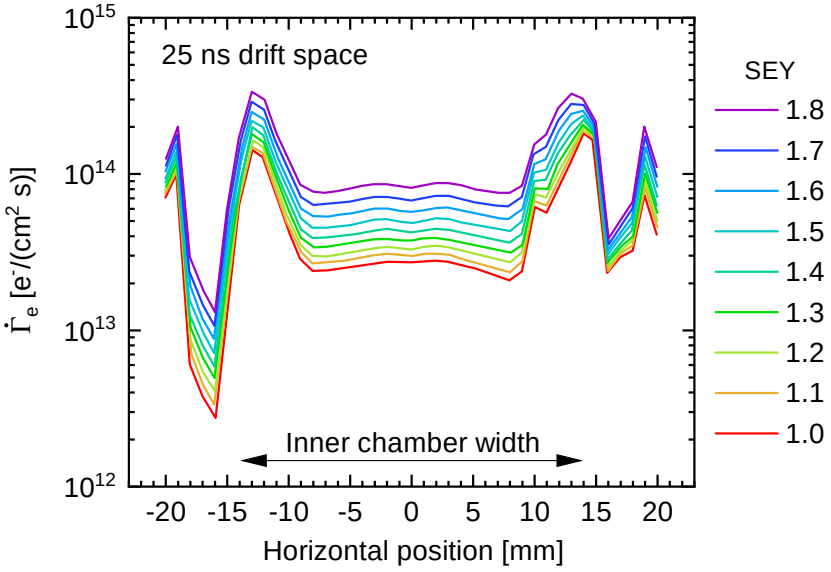

FIGURE 4.55: Horizontal projection of $\dot{\Gamma}_e$ in the FCC-hh BS in the interconnection area, with no magnetic field, as a function of the SEY. Nominal beam parameters. Absorber slope treated with LASE. Taken from [74].

In the drifts, however, $\dot{\Gamma}_e$ is much higher than in the magnets owing to the high N_e on the SR absorber and to the absence of a SEY mitigation treatment in this region apart from the slope of the SR absorber. Provided that the SEY is set under the multipacting threshold, the $\dot{\Gamma}_e$ in this region entails a considerably small rise in the gas density for all

the possible bunch spacing options (25 ns, 12.5 ns, 5 ns). For the 25 ns the performed calculations show that it can represent around 10 % of the total gas density in the arcs.

As previously discussed, not using a SEY mitigation treatment and relying only on scrubbed Cu is only possible in dipoles and drifts for 25 ns and 5 ns [79]. In dipoles, for a scrubbed Cu with a SEY = 1.4, the ESD gas load has been estimated to be two times higher than that of LASE treated Cu. This option would require a further conditioning of the BS until being able to reach vacuum specifications with nominal beam parameters, adding approximately 20 Ah of necessary dose.

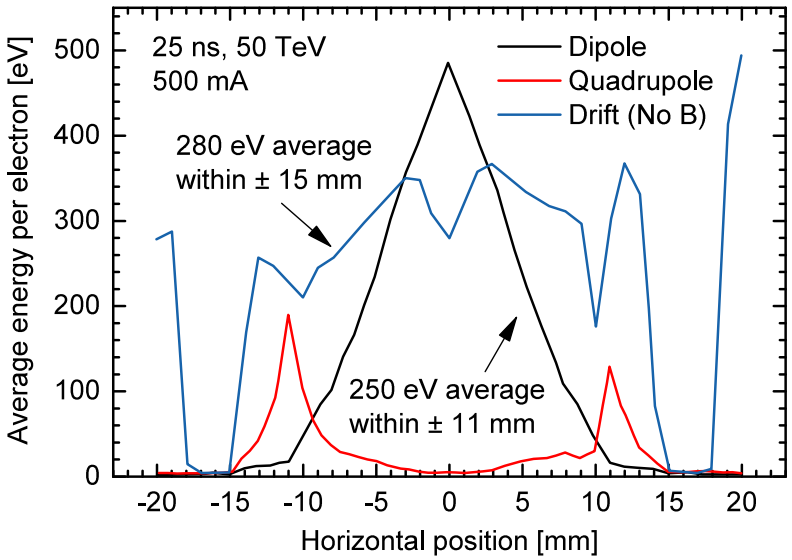

FIGURE 4.56: Average electron impact energy in a dipole with SEY=1.4, in a MB-MB drift space with SEY=1.4 and no magnetic field, and in a quadrupole with SEY=1.1. Nominal beam parameters. Taken from [74].

The average electron impact energies were also calculated by the WP2. An example for the 25 ns baseline is displayed in Fig. 4.56, plotting the values as a horizontal projection. In all the three studied magnetic field variations the electron energy remains always under 300 eV, making the chosen η_e data [148], for an electron energy of 300 eV, a conservative choice.

In this Figure it is also possible to notice the low energy of the electrons in the secondary chamber of the BS in the dipoles and quadrupoles, starting at around $\pm$ 14 mm in the horizontal length, owing to the low energy gain they receive in this region.

In the drifts, the 1.9 K cold bore is not present. Therefore, the power which is leaked through the BS pumping holes is not as dangerous as if it were inside the magnets. Additionally, the simulations with PyECLOUD have been performed considering a BS profile without pumping holes, with an effective N_e on their otherwise empty volume. The shown $\dot{\Gamma}_e$ can be thus considered overestimated.

Thanks to the low energy carried by the electrons leaked through the BS pumping holes, the recycling effect ascribed to ESD has not been taken into account in the gas density calculation, neglecting the value of η'_e in Eq. 4.20.

4.5.4 Ion stimulated desorption (ISD)

In proton colliders the maximum beam current is limited among other things by the ISD. The proton beam ionizes residual gas molecules in its path and repels them due to its positive space-charge potential. Ions are then accelerated towards the BS walls and cause gas desorption upon impacting onto them. As the resulting increase in the gas density exacerbates the ionization rate, an avalanche process may then occur, triggering a gas density overrun if the beam current is high enough [27]. Such beam current value is defined as the critical current (I_c).

To calculate (I_c) a simple approach found in [151] for a two gases system has been followed. Two representative areas of the arc cell have been studied: the BS length inside the MBs, where a constant and distributed pumping speed is present; and the magnets interconnections, where no active pumping is present and the low pipe conductance plays a major role. Since (I_c) depends on the capacity of the studied area to evacuate the generated gas, the interconnections result to be the bottleneck of the system.

With regard to the gas mixtures studied, the combination of CO and CO_2 has been found to be the worst one owing to the large cross section and molecular yields of these species. The mixture of the most common species, H_2 and CO, have also been studied for the sake of comparison.

$$I_c(j,k) = \frac{\alpha_j \, e}{\eta_{i,k,j} \, \sigma_{i,k}} \tag{4.26}$$

Eq. 4.26 represents the partial critical current for a region with a constant distributed pumping (α_j). The complete formulas used for both areas can be found in [151]. $\eta_{i,k,j}$ depends on the ion impact energy. The procedures for calculating the ion energy of round and flat beams are described in [152, 153] and [154], respectively.

TABLE 4.12: Average ion energies for different beam sizes, from [74].

Ion species	Arcs ($\beta_{x,y}$ = 225 m)	IP ($\beta_{x,y}$ = 1.1 m)
H_2^+	185 eV	16 keV
CO^+	142 eV	5.2 keV
CO_2^+	141 eV	3.7 keV

The results of the calculation, taken from [74], are displayed in Table 4.12 including the results for the interaction points as well, for comparison. For each set of beam parameters, the ion energy was calculated for different initial positions of the ion across

and along the beam, according to the distribution of protons within the bunch, and without magnetic field presence. The calculations were performed for H_2^+, CO^+, and CO_2^+. No difference was found between them.

The average ion impact energy results in around 185 eV for H_2 and 142 eV for CO and CO_2. In the presence of a dipole magnetic field, an energy increase by a factor of 1.05–1.15 was estimated for the LHC for H_2. For CO [153], no noticeable change was found. For quadrupoles, a factor of 1.3–1.7 was found for H_2 only.

The $\eta_{i,k,j}$ data estimated during the LHC studies [151] have been chosen as an input for the calculations, with 500 eV for H_2 and 300 eV for the other gas species. This approach should be safe enough as the real $\eta_{i,k,j}$ for the most dangerous species (CO_2 and CO) are expected to be lower because of the lower ion energies. The recycling effect has not been considered in the calculations since ions are not expected to reach the 1.9 K CB, and the interconnection regions is assumed to be clean, with a gas coverage under the monolayer. It is nevertheless worth mentioning the importance of keeping at all times a low gas coverage in the interconnection, especially during the pumping/cooling down process. η_i values grow considerably fast along with the coverage, being I_c lowered in the same proportion. High coverages could result in undesired pressure pikes owing to ISD, among other effects.

TABLE 4.13: Comparison of the ionization cross sections of the FCC-hh and the previous proton accelerators [155]. A clear dependence on the beam energy can be observed.

Beam ionization cross section (σ_i) 10^{-22} m^2			
Gas species	SPS 0.45 TeV	LHC 7 TeV	FCC-hh 50 TeV
H_2	0.36	0.45	0.51
CO	2.2	2.7	3.3
CO_2	3.4	4.3	5.1
CH_4	2.5	3.2	3.7

As for the ionization cross section, the values estimated for the different gas species in the FCC-hh are displayed in Table 4.13. They are compared with the ones for previous colliders. They are around a 15 % higher than the values found for the LHC due to the higher beam energy.

The calculated I_c values are displayed in Tables 4.14 and 4.15. Due to the uncertainties of the input data a safety factor of 3 is suggested to be applied (as recommended in [151]).

In order to prevent a pressure overrun, the beam current in the FCC-hh arcs would then be limited to 6.8 A, around 2.2 A if taking into account the safety factor. Being the FCC-hh designed for 0.5 A, it is concluded that the design is safe. However, a slight

TABLE 4.14: Results of I_c and related gas density increment in the arc magnets.

Arc BS	H_2 + CO	CO + CO_2
I_c	37 A	19 A
Related $\Delta n_{H_2\,eq}$	1.4 %	2.7 %

TABLE 4.15: Results of I_c and related gas density increment in the MB-MB interconnection.

MB-MB interconnection	H_2 + CO	CO + CO_2
I_c	12.8 A	6.8 A
Related $\Delta n_{H_2\,eq}$	4.1 %	7.9 %

rise in the gas density is expected because of ISD. It can be easily calculated using Eq. 4.27.

$$\Delta n_{H_2\,eq}(\%) = \frac{100 \times I}{I_c - I} \tag{4.27}$$

In the worst case, for a gas mixture composed entirely of CO and CO_2, $n_{H_2\,eq}$ would be increased by about 2.7 % in the magnets and a 7.9 % in the middle of the interconnections. In a more realistic case (see expected composition in Table 4.18) the increment would be a 1.4 % in the magnets and a 4.1 % in the middle of the interconnections. Taking a look at these numbers, ISD is concluded to be the beam induced vacuum effect with the smallest contribution to the total gas load in the FCC-hh.

Derived from the same results, it is possible to calculate the critical length of the interconnection. It is the length at which the pumping speed at its middle point is so low that the beam current reaches its critical value. Eqs. 4.28 and 4.29 have been used to calculate these values for different gas species, as single gases. The results are shown in Table 4.16.

$$L_{max}(j) \approx \pi \sqrt{\frac{u_j\, e}{\eta_{i,j}\, I\, \sigma_{i,j}}} \tag{4.28}$$

$$u_j \approx \frac{d^3}{3} \sqrt{\frac{\pi\, R\, T}{2\, M_j}} \tag{4.29}$$

where u is the specific conductance of the interconnection pipe, d the pipe diameter, R the ideal gas constant and T the system's temperature. The calculations show that the pipe length would be limited to 0.68 m, taking into account a safety factor of 3 and without considering any pumping in this region. Being 0.4 m the proposed length of the interconnection (measured between CB extremes), the design should be safe.

TABLE 4.16: Maximum length between CB at the MB-MB interconnection, for different gas species and at 40 K.

Gas	H_2	CO	CO_2	CH_4
Max length	18.6 m	2.0 m	2.2 m	9.0 m
Safety factor 3	6.2 m	0.68 m	0.73 m	3.0 m

4.6 Gas density evolution in the arcs

For the periodic arc length studied (see Fig. 4.42), all the average gas densities for all beam induced effects, and for all the studied gas species, have been converted to $H_{2\,eq}$ units (see Eq. 2.3) and added together over a series of arbitrary photon doses. The results are plotted in Fig. 4.57.

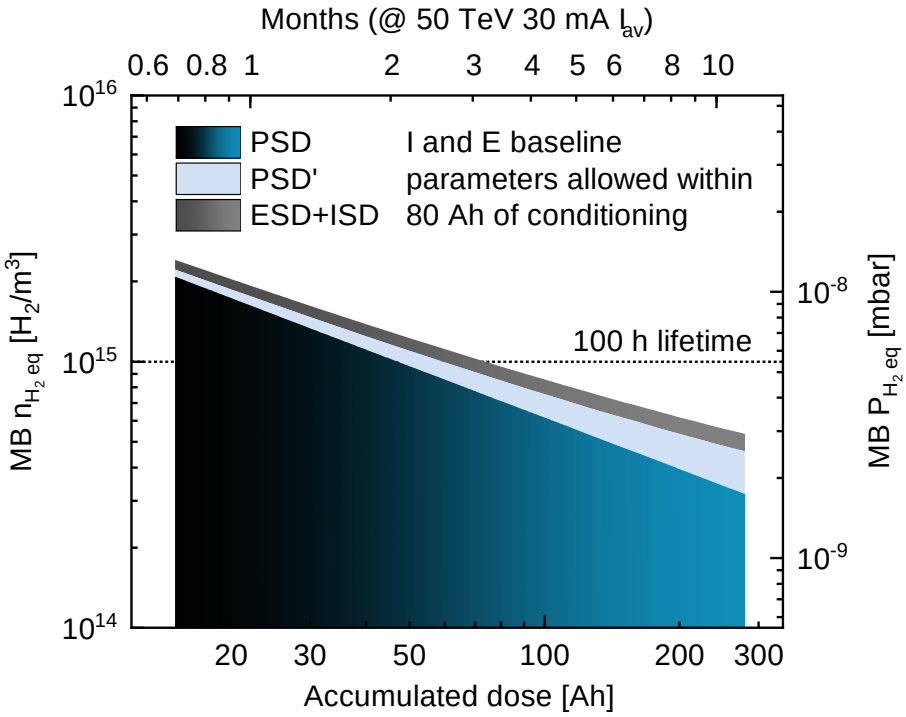

FIGURE 4.57: Average H_2 equivalent gas density over the accumulated beam dose in the arcs, taken into account all the beam induced vacuum effects. Nominal beam parameters.

A curve has been adjusted to the points found and extrapolated, resulting in a continuous plot. The calculation has been done for a 40 K He MB BS and a 500 mA, 50 TeV, 25 ns beam, with SEY = 1. It has been calculated in a pessimistic way, taking the average $n_{H_2\,eq}$ along the most irradiated MBs of the arc cell as if it was the same for all the arc magnets.

According to the obtained results, the goal of 100 h nuclear scattering lifetime using nominal beam parameters would be achieved within a dose of 80 Ah. It is equivalent

to around 4 months of continuous operation with an average current of 30 mA, value similar to that of the first years of the LHC commissioning, with around 300 Ah per year. Running at 50 TeV is still possible before reaching this level of conditioning, but with beam current limitations. Ultimate beam parameters are usually reached only after some years of conditioning, so vacuum is not expected to be a bottleneck in the FCC-hh commissioning out of the initial pump downs. For comparison, after two years of commissioning of the LHC the maximum beam energy achieved was still at 50% of the nominal one, while the beam current reached 62% of the nominal value. After five years, the maximum energy reached around 93% of its nominal value and the beam current the 77% [156].

As expected, the effect with the highest partial gas density is PSD, with the other effects playing a minor role. ESD and ISD would be efficiently suppressed thanks to the SEY mitigation and to the high pumping speed of the BS, respectively. PSD' may account for a significant gas load after some months of use. However, as previously discussed, its $H_{2\,eq}$ η'_{ph} does not vary much for the gas coverage which the cold mass is expected to reach (see Table 4.10). Therefore, a point in which the $n_{H_2\,eq}$ starts growing and the 100 h lifetime limit is surpassed due to the high recycling effect is not expected to happen during 2 years of continuous operation. Nevertheless, because of this effect it would be difficult to go under 2×10^{14} $H_{2\,eq}/m^3$ in the presented conservative scenario. Future measurements of η'_{ph} for a lower ε_c value than the one related to the used data will lower this estimated value.

Table 4.17 shows the calculated ratio of gas load of each studied effect with respect to the total value, for two different arbitrary beam doses. Being both PSD and PSD' conservatively overestimated, the error with respect to the real phenomena may be large. Even so, the shown data are useful in an indicative way, highlighting PSD as the effect with the highest impact on the beam lifetime.

TABLE 4.17: Gas load ratios of the beam vacuum induced effects for two different arbitrary doses.

Dose	PSD	PSD'	ESD	ISD
36 Ah	80 %	10 %	8 %	< 3 %
120 Ah	70 %	18 %	11 %	< 3 %

The gas density profile along the most irradiated MB in the arcs was also calculated. It is shown in Fig. 4.58. The first two MB after the SSS would have a lower gas density owing to the negligible SR emission from the SSS magnets. Along each magnet the gas density does not vary considerably thanks to the distributed cryopumping. A gas density bump can be observed on the right side of the plot. As seen previously, it is ascribed to the absence of pumping in the interconnection region, to the high SR power density on the photon absorber present at the end of each MB, and to the high ESD gas load in this region. This bump was considerably diminished after lowering

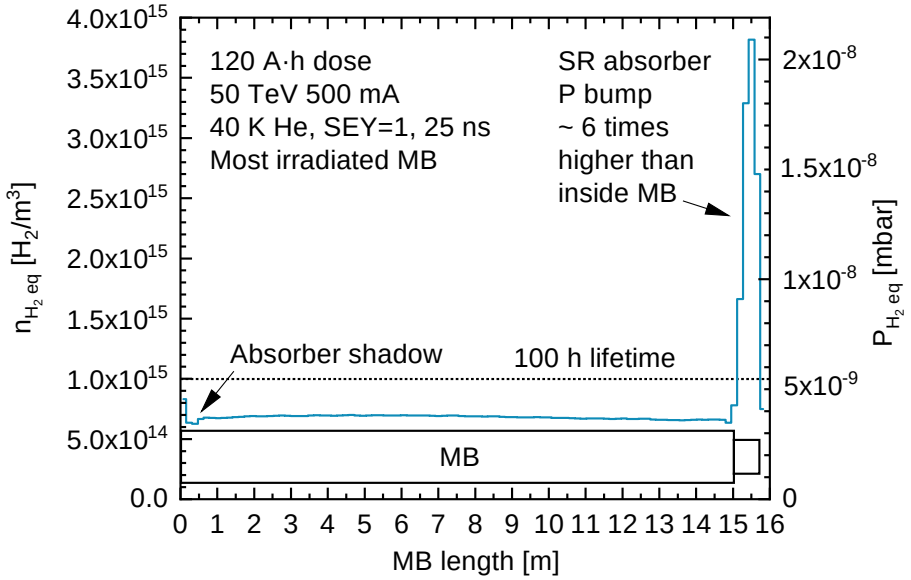

FIGURE 4.58: H_2 equivalent gas density profile of the most irradiated MB in the arcs, for a 120 Ah beam dose. Calculated for a 50 TeV, 25 ns, non ideal proton beam.

the SR power on the SR absorber, and could be further lowered if continuing doing so or if the SR was removed. This would be possible at the expense of lower tolerance margins.

TABLE 4.18: Gas composition ratios of the main four species for an arbitrary dose of 120 Ah.

Gas	H_2	CO	CO_2	CH_4
Total $H_{2\,eq}$	29 %	57 %	12 %	2 %
Absolute	79 %	17 %	2 %	1 %
Abs w/o recycling	63 %	31 %	4 %	2 %

The calculated gas composition is shown in Table 4.18 for the chosen beam doses. In absolute units, H_2 is the predominant species. Nonetheless, after converting all the species to $H_{2\,eq}$ units, CO becomes clearly the most relevant one, featuring the highest impact on the beam lifetime. Even if CO_2 has the highest cross section, its η_{ph} is expected to be considerably low at the studied range of temperatures due to the chemical nature of this species, lowering therefore its resulting impact on the beam lifetime.

4.7 Evaluation of the experimental results at BESTEX

4.7.1 Computer model

In order to enhance the validity of the performed vacuum simulations, the pressure measurements of the first experimental run at BESTEX were compared with the theoretical predictions of the same measurements. The simulations were performed with Molflow+, using as an input the ray tracing results obtained with Synrad+.

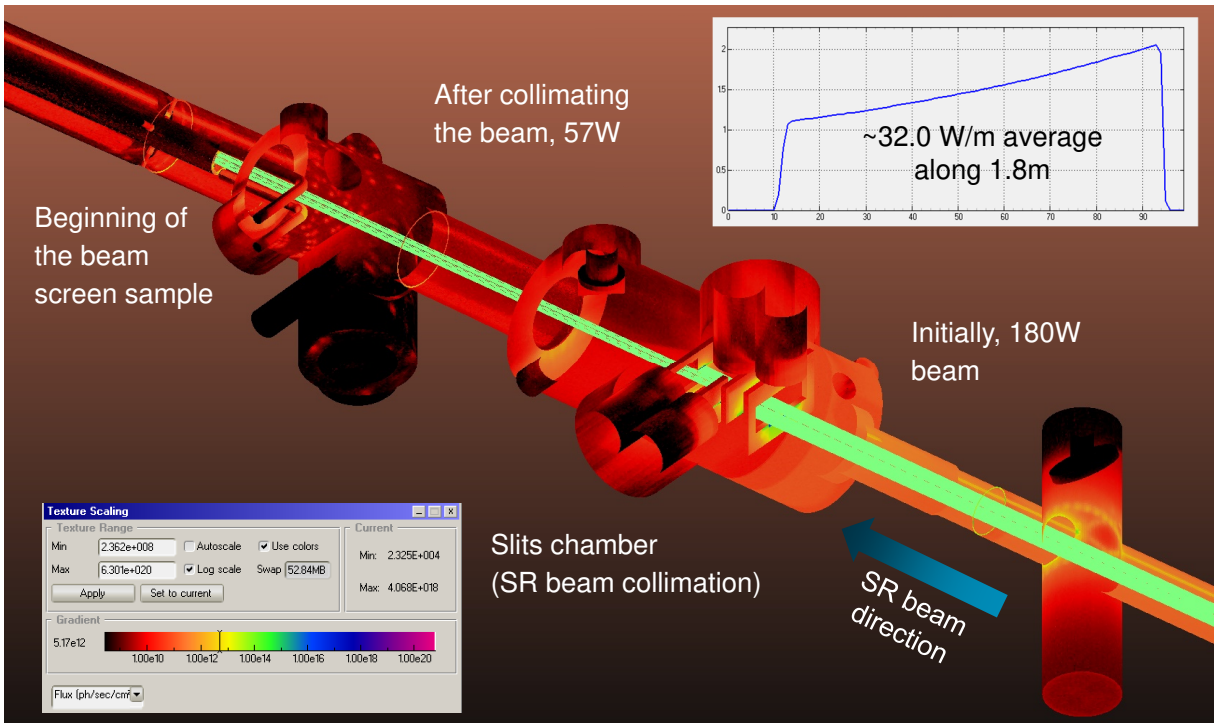

FIGURE 4.59: Ray tracing simulation in BESTEX, showing the photon flux distribution map. 2.5 GeV, 130 mA beam.

The CAD model of BESTEX was first of all simplified to easily export it to Synrad+. The original model had to many elements and complexity to be used efficiently, slowing down the simulation and its practical optimization. The ray tracing simulations with Synrad+ were also used to guide the alignment of the samples and to calculate the movement of the slits in order to obtain a SR beam with the desired flux and power. These data were used to carry out all the experiments. Owing to the complex power distribution of the SR beam, such calculation would have been very complex to perform analytically. Using the CAD model, the calculation of the movement of the supports to obtain the chosen angle of irradiation was also done. The drawings of KARA's light source were studied to properly place the electron beam path, the crotch absorber and collimation stations in the Synrad+ model. This model is shown in Fig. 4.59, displaying the ray tracing results of one of the first performed simulations. The SR beam, coming from KARA's storage ring, is displayed in green. It can be seen how its size

and power are reduced after passing through the slits. The power profile along the 2 m long sample is also shown on the upper right.

The ray tracing results were then exported to Molflow+, in order to calculate the gas density for the four studied gas species. H_2O was not considered in this case, either, since a bake-out was done before each experimental run, so H_2O was not expected nor read in the RGA.

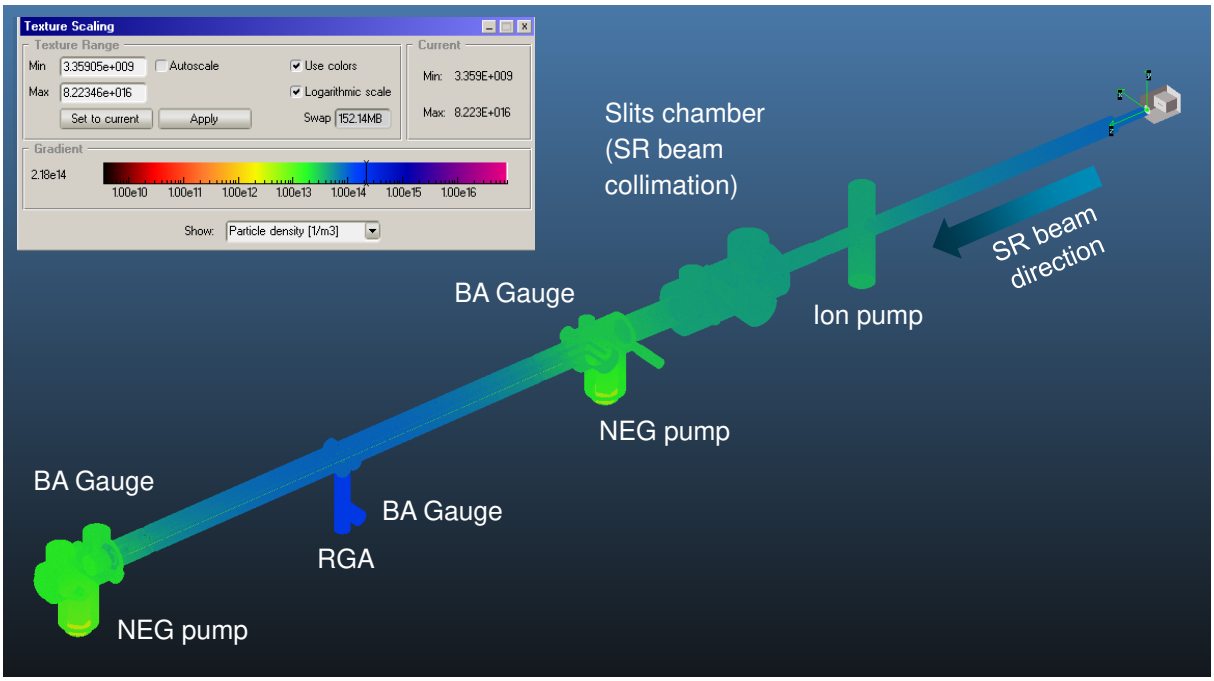

FIGURE 4.60: Simulation of H_2 molecular density map in BESTEX, after 24 h of beam dose. Arbitrary yield data.

The total pressure is calculated as the sum of the static pressure and the dynamic one. The static pressure was calculated from the outgassing values (q) found in [157]. The dynamic pressure was calculated for two arbitrary doses, 3 Ah and 9.5 Ah. In BESTEX case, it is only caused by PSD. The slits cut the tails of the SR beam, with a lower average energy than the centre of the beam, increasing the average photon energy. The $\varepsilon_{c\,eq}$ of the cropped SR beam is then around 7.8 keV, higher than the initial SR produced by the beam, around 6.2 keV. On the contrary, the areas of the studied sample receiving radiation from reflection, have a much lower $\varepsilon_{c\,eq}$, since only low energy photons are reflected.

The calculation process was performed as accurately as possible, using different values of η_{ph} according to the ε_c of the SR arriving to the different areas of the chamber. Different sets of η_{ph} were estimated for different regions of the geometry, in the same way as the one explained in Subsection 4.5.1. The estimation was done extrapolating in this case the η_{ph} of Cu from [138] and the η_{ph} of SS from [56]. The NEXTorr pumps of 2000 l/s and the ion pump placed before the slits chamber where taken into account in the simulation, setting a proper sticking probability of the pump surfaces

to emulate the total pumping speed for each gas. Since the pumping speed is different for each gas, the technical specifications of the pumps supplied by the manufacturer where checked in order to obtain them. A small outgassing and pumping speed were considered for the BA gauges as well, obtained from the literature [158]. An example of the simulation results for H_2 is presented in Fig. 4.60.

At a quick glance it is possible to see that the regions with the lowest pressure are those next to the NEXTorr pumps. The region with the highest pressure is the RGA chamber, since it is the furthest point from the pumps.

4.7.2 Lessons learned from the experimental results

A comparison between the experimental results of the first run and the calculations is presented in Table 4.19. The pressure is read in three different points of the chamber: in the middle of the sample and at the two extremes. These locations are indicated in Fig. 4.61. More information about the data acquisition procedure can be found in [64].

	3 Ah		9.5 Ah	
	Calculation	Experiment	Calculation	Experiment
Front [mbar]	2.9×10^{-9}	2.9×10^{-9}	1.6×10^{-9}	$2.0 \times 10^{-}9$
Middle [mbar]	6.3×10^{-9}	5.7×10^{-9}	3.3×10^{-9}	$3.0 \times 10^{-}9$
Back [mbar]	2.8×10^{-9}	2.0×10^{-9}	1.4×10^{-9}	$1.0 \times 10^{-}9$

TABLE 4.19: Comparison between experimental results and theoretical calculations during the irradiation of the 1st BS prototype.

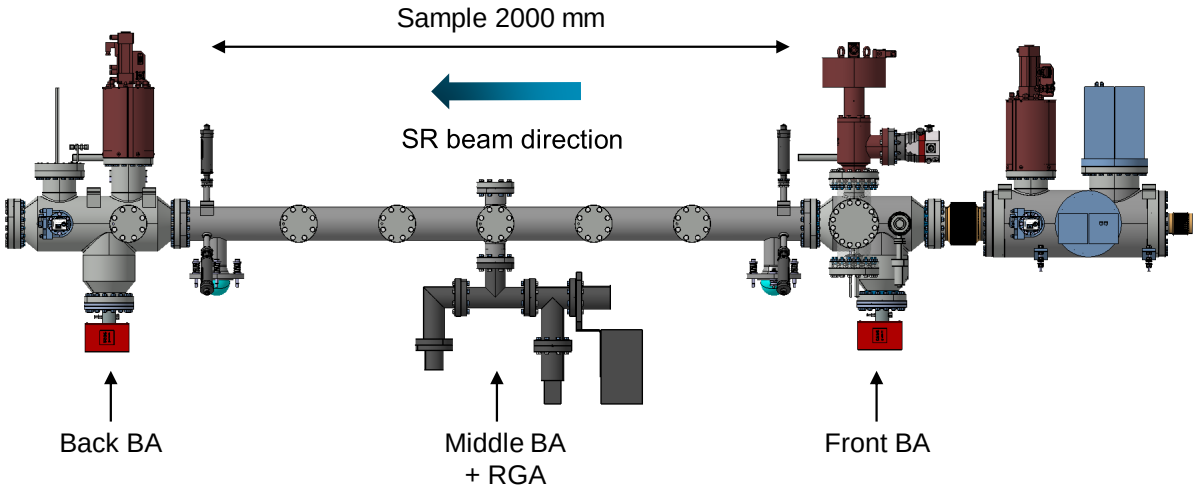

FIGURE 4.61: Location of the pressure measurement points in BESTEX.

The match between the calculated and experimental data is fairly good for these kind of calculations. The relative discrepancy remains in all cases below 30 %. Generally, in the literature it can be found that the same material, with the same treatment

and under the same conditions, can present completely different values of q and η_{ph}. Discrepancies between the predictions and experimental data of a factor of two or more are usual. It is important to highlight, besides, that the measurement error of the BA gauges can go up to the 15%. The reasonably good match between measurements and calculations gives confidence when using the same methodologies as a guide for the whole FCC-hh design.

Another performed experiment was the comparison of the relative reflectivity of one of the BS prototypes equipped with the reflecting edge and the prototype equipped with the LHC sawtooth profile.

The relative reflectivity measurements were performed measuring the SR-induced photoelectron current at the end of the setup, placed next to the Cu photon cup (see Fig. 3.5). After impacting onto the sample, some photons are reflected downstream and end impacting onto the Cu photon cup, placed at the end of the setup. The generated photoelectrons are then collected by the electrode applying a bias voltage on it. Normalizing this current with respect to the current read when directly irradiating the photon cup, it is possible to obtain a relative reflectivity. The relative reflectivity comparison is presented in Fig. 4.62, plotted with respect to the applied bias. As expected, the sample equipped with the LHC sawtooth performs much better, confirming the assumptions taken in the BS design and the performed calculations.

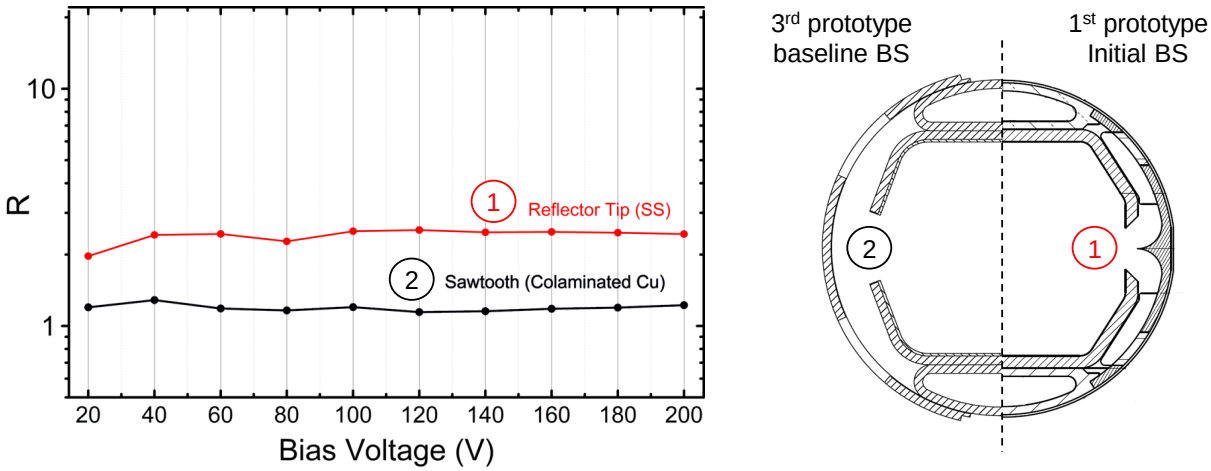

FIGURE 4.62: Relative reflectivity comparison between a prototype equipped with reflecting edge and the prototype equipped with the LHC sawtooth profile. Adapted from [66].

Another important performed experiment was the assessment of the PSD performance of a normally oriented sawtooth profile and an inverted one, to see the gain of the normal incidence [65]. This experiment was done in the 3^{rd} experimental run, with the latest BS prototype. The sample (see Fig. 4.14, on the right) was built using the LHC sawtooth on both lateral baffles, but intentionally mounting one the other way around. Irradiating the sample with a mirrored angle, the opposite baffle was irradiated, making it possible to get data from a differently oriented surface without

changing the inserted sample. The results of this experiment are displayed in Fig. 4.63. In the Figure, the dynamic pressure in mbar/mA units is plotted over the accumulated photon dose.

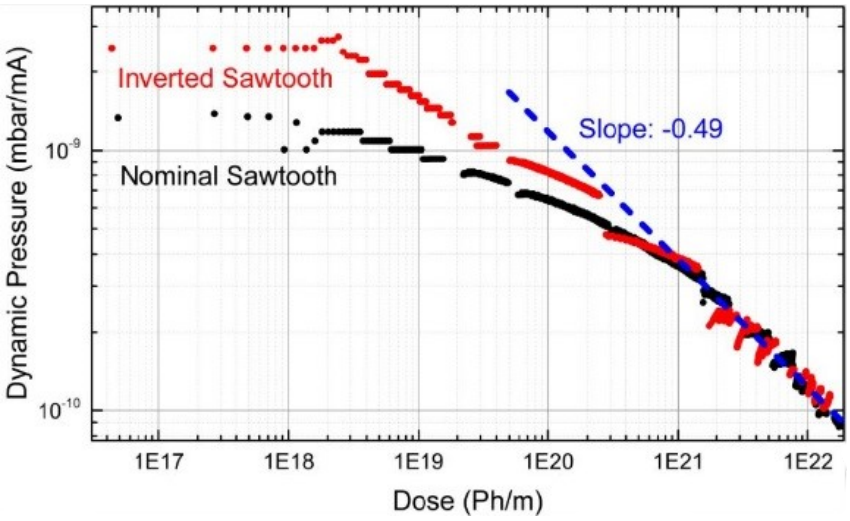

FIGURE 4.63: Comparison of the relative gas load of a normally irradiated Cu sawtooth profile and an inverted one. Taken from [65].

It can be seen how the gas load is clearly lower in the case of the nominal sawtooth, especially for low photon doses, up to a factor of 2. At high doses, as most PSD curves, both values converge to the same yield. Since the material is exactly the same, these results prove that absorbing the SR with normal incidence reduces effectively the gas load in the system due to PSD.

The pressure data of the nominal sawtooth (used in the 3^{rd} prototype) was then converted to absolute η_{ph} data, in molecules/photon, adding all the η_{ph} values of all the read gases [159]. It was then plotted and compared to the absolute η_{ph} of the other surfaces irradiated in the experimental runs (see Table 3.2). These irradiated surfaces are: the sharp reflecting edge of the 1^{st} prototype, the sharp reflecting edge of the 2^{nd} prototype (mounted in a different sample, with cold spray coating), and the sawtooth and LASE surfaces of the sharp reflecting edge of the 3^{rd} prototype. The results can be found in Fig. 4.64.

This figure summarizes the most relevant outputs from BESTEX during EuroCirCol's timeline. Much information can be extracted from the shown data:

- The most important conclusion, is that the η_{ph} and thus the corresponding PSD gas load of the sawtooth Cu (plotted in red) is much lower than that of the SS reflecting edge of the 1^{st} prototype (in blue). At lower doses, using a SS reflecting edge, as in the initially proposed BS design (see Fig. 4.65), would entail a gas density at least one order of magnitude above. The greater N_e would raise this difference even further. This proves that the proposed strategy of maximizing the SR absorption will improve the vacuum level of the FCC-hh. The green line corresponds to a reflecting edge, as well, but mounted in the 2^{nd} prototype instead of

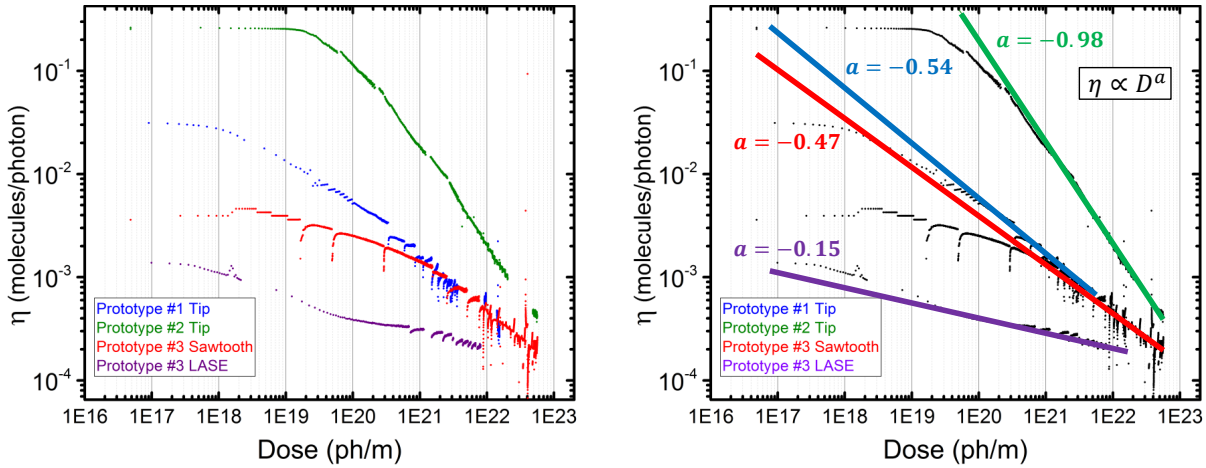

FIGURE 4.64: Total η_{ph} estimated for the different tested configurations in BESTEX. On the left, raw data acquired. On the right, different curves have been adjusted to the continuous part of the data, and the slope has been calculated. Adapted from [66].

the 1st. As it can be observed, η_{ph} in this case is generally much higher, well above the blue curve. These higher values are ascribed to the presence of the ceramic layer on the primary chamber, and thus they are deemed not to be representative. Ceramic materials are known to possess large values of η_{ph} and q compared to metallic materials, and should never be irradiated by SR. In this case, the rounded edge scatters a significant amount of SR flux towards the ceramic layer, resulting in a high η_{ph}. This was also proved by a high current reading in the electrode [159].

- The convergence of all the data into a common value can also be observed, happening after a photon dose of 1×10^{23} photons/m. The decay slope is also found to be dependent on the initial yield. This fits very well with the assumptions taken in the estimation of η_{ph} for the FCC-hh conditions, enhancing their validity.

- Additionally, LASE has been found to present an extremely good performance, much better even than sawtooth Cu. Its η_{ph} is the lowest, starting at a very low value and decaying slowly. This proves the hypothesis that predicted the low η_{ph} expected for this treatment, stated after evaluating its SEY and Y_{ph}. This also validates the idea of using LASE in the lateral baffles of the BS, as an addition or replacement of the sawtooth profile. Its use, not only would lower the gas load ascribed to PSD, but also ESD, since the number of photons reflected back to the primary chamber would be lower.

As critical future work, it remains the acquisition of η_{ph} at cryogenic temperatures. The setup is prepared to use liquid N_2 as a coolant for the samples, and the first tests carried out without SR showed a good static pressure [159], so for the time being no

FIGURE 4.65: First prototypes of the FCC-hh BS. Manufactured by CERN.

technical showstoppers have been identified. The acquisition of these data will validate the estimated values for the FCC-hh conditions. Since the estimation was done in a conservative way, the real experimental values are expected to be lower.

Chapter 5

Summary and conclusions

The main objective of this thesis, titled *Study of the beam induced vacuum effects in the cryogenic beam vacuum chamber of the Future Circular Hadron Collider*, has been the feasibility assessment of the cryogenic beam vacuum system of the FCC-hh, a hadron collider expected to be the LHC's successor reaching unprecedented levels of beam energy. To this end, the main task has been divided in two co-dependent parts: (i) the preliminary design of the FCC-hh beam screen has been updated and validated [79], and (ii) the whole cryogenic beam vacuum system has been modelled, studying the gas generation mechanisms taking place inside the beam chamber and calculating the gas density over time, assessing the feasibility of the conditioning time [74].

After the performed study, a series of conclusions can be extracted, and are hereby detailed.

5.1 Conclusions from the beam screen design study

- The suitability of the initial beam screen design for the FCC-hh was assessed. It was based on a strategy of maximizing the reflectivity in order to handle the synchrotron radiation. Owing to the excessive electron cloud build up, gas generation, heat transferred to the cold mass and little margin on misalignment, it was deemed non-viable.

- In order to sort out the issues of the initial FCC-hh beam screen design, a new one has been proposed. The new design allows the magnet aperture to be reduced from 56 mm to 50 mm and still provides good conditions for the beam, i.e. good vacuum, low impedance and suppression of electron cloud effects. It is intended to mitigate the detrimental effects arisen from the beam energy increase (from the 7 TeV of the LHC up to the 50 TeV of the FCC-hh) which increases the synchrotron radiation (SR) linear power density from 0.22 W/m up to 35.4 W/m. At the same temperature, it is able to provide 80% more pumping speed than that of the LHC, around 900 l/(m s) at 40 K, at the expense of a higher manufacturing cost. That said, the increased cost is expected to be nevertheless negligible compared to the whole machine.

- Laser Ablation Surface Engineering (LASE) has been studied in a theoretical way as a solution to lower the e^- cloud density, and thus the ESD. From a vacuum point of view, the baseline variation is expected to work considerably well in steady-state operation.

- From the vacuum point of view, it is possible to use scrubbed copper without any further SEY reduction treatment in the dipoles at 25 ns of bunch spacing. It entails a higher beam dose before reaching 100 h of nuclear scattering lifetime using design beam parameters.

- Nevertheless, LASE is observed to trade off the original surface conductivity for the good SEY properties, the more extreme the trade off, the higher the ablation rate chosen. Since ESD is expected to be significantly low, the ablation rate of the chosen LASE variation can be lowered, to reach a better compromise between surface resistance and SEY, in case that a reduction of the beam screen impedance was required.

- A new cryogenically cooled photon absorber has been proposed for the FCC-hh bending magnets. It aims to protect the magnet interconnections from direct SR irradiation, whilst minimizing the SR scattering and taking into account large misalignment errors. Further studies can still improve its performance, by changing its position and/or reducing the amount of absorbed power, providing that smaller alignment and tolerance errors can be assumed.

- Owing to the double chamber layout of the FCC-hh beam screen, the electron shield used in the LHC to protect the cold bore from electron impingement is no longer required.

- Thanks to the copper layer applied on the lateral baffles, the initially proposed copper rings applied on the outer surface of the initial FCC-hh beam screen are no longer necessary, reducing considerably the manufacturing costs.

- A sawtooth profile has been found to be the most efficient way, for the time being, to cope with the high levels of SR in the FCC-hh vacuum chamber. Using the experimental data acquired at BESSY-II's optics beamline, the performance of the LHC sawtooth was benchmarked and used to improve a computer model. This model has been used to extrapolate the measurements to the FCC-hh case, and compared against different strategies to mitigate the synchrotron radiation. Like for the LHC, a strategy minimizing the amount of scattered SR has turned out to be the one maximizing the vacuum and machine performance of the FCC-hh.

- Since, compared to the LHC, the FCC-hh has a much lower grazing angle of SR incidence against the vacuum chamber wall, it is recommended to adapt the

current features of the sawtooth profile to overcome the proportionally higher reflectivity. A simple and effective solution consists in enlarging the pitch between edges, increasing the performance of the former sawtooth without any derived detrimental effects, provided that the enhanced thermal stress is kept below the limits. If in the future, further SR absorption is required for instance to lower the e^- cloud density or the gas load due to recycling, LASE could be used from the vacuum point of view in addition to or as an alternative to sawtooth, but implying higher manufacturing costs.

- Even though the beam screen temperature of the FCC-hh is higher than in the LHC, 40–60 K against 5–20 K, the heat load on the cold bore is kept within specifications, thanks to a much higher heat budget. This is achieved mainly due to the specifically designed SS P506 beam screen-cold bore supports, which minimize the leaked heat through conduction, and thanks to the sawtooth profile, which minimizes the scattered synchrotron radiation.

5.2 Conclusions from the vacuum study

- A thorough study of the beam induced vacuum effects in the FCC-hh has been carried out. The vacuum chamber geometry has been iteratively designed according to the performed gas density calculations. The studied effects are photon stimulated desorption (PSD), electron stimulated desorption (ESD) and ion stimulated desorption (ISD). Due to the high SR flux and power, PSD is expected to be the vacuum effect representing the highest gas load in the vacuum chamber, more than 80%. Thanks to the secondary electron yield (SEY) mitigation of the beam screen inner surfaces, ESD would be relegated to a minor role. This will be the opposite case than in the LHC, where the low SR power and the absence of SEY mitigation cause ESD to be the predominant vacuum effect.

- The secondary PSD is especially challenging to estimate due to the lack of accurate data in the literature. Even if overestimating its contribution, the obtained gas load seems to be safe. Future experiments will have to measure the PSD secondary molecular desorption yield over a broad range of gas coverage values and low SR critical energies.

- ISD is not expected to be a major concern. The critical current (6.8 A) at the worst region, the magnets interconnections, is well above the design one (0.5 A), resulting in very small gas density increments due to this effect.

- H_2 is found to be the most abundant gas species, specially if taking into account the recycling effect of the gas condensed on the cold bore. The species with the highest impact on the beam lifetime is expected to be CO.

- The experimental data acquired in the BESTEX setup has been useful to confirm the validity of the hypotheses and computing tools used to design the FCC-hh vacuum system. Among others, it has proved the theorized higher vacuum performance of the sawtooth profile compared with the sharp edge solution, the good vacuum performance predicted for LASE and its low reflectivity. In the future, it is expected to measure the PSD yield of sawtooth Cu at cryogenic temperatures, the most important missing data.

- Despite the much worse synchrotron radiation power conditions, it is concluded that the vacuum system of the FCC-hh should be feasible. The conditioning time needed to run the collider with baseline beam parameters and above 100 h of nuclear scattering lifetime is acceptable, i.e. lower than 80 Ah, equivalent to around 4 months of staged commissioning. Since design parameters are usually reached after years of operation owing to other reasons, vacuum is not expected to be the bottleneck in the machine commissioning. That being said, and despite the good forecasts, to fully assess the viability of the proposed FCC-hh vacuum system and lower the high uncertainty of the performed estimations, dedicated experiments will have to be carried out in the future to acquire the missing data.

Chapter 6

Publications related to the thesis work

6.1 Peer-reviewed publications

Two peer-reviewed publications have been written with the thesis author as the main one, summarizing the most important accomplishments of this thesis. They represent the work carried out not only by the author but also by many participants of the EuroCirCol collaboration. Both have been published in the *Physical Review - Accelerators and Beams* (PRAB) journal [160].

- **Design of the FCC-hh beam vacuum chamber. I. Bellafont *et al.* [79]. DOI = 10.1103/PhysRevAccelBeams.23.033201**: This publication presents the FCC-hh beam vacuum chamber designed within EuroCirCol's framework. The elements and functionalities of the beam screen (BS) are thoroughly explained, emphasizing their role in the beam induced effects mitigation, specially the electron cloud's (e^- cloud). Being the SR the main source of residual gas in the vacuum chamber, it has been studied in detail and compared with that of the LHC. A photon ray tracing is performed with Synrad+ [53, 56] and used as an input (among others) to calculate the thermo-mechanical behaviour of the BS in steady state dynamic mode and during a magnet quench. The e^- cloud generation and features inside the BS are studied, including the BS secondary electron yield (SEY) specifications and the derived transverse beam instabilities. The e^- studies were carried out in collaboration with the WP2. The total heat load on the cold bore from the BS is also analysed.

  The presented BS is then found to perform well in all the studied areas and it is established as the FCC-hh baseline.

- **Study of the beam induced vacuum effects in the FCC-hh vacuum chamber I. Bellafont *et al.* [74]. DOI = 10.1103/PhysRevAccelBeams.23.043201**: In this publication the detrimental impact of the beam induced vacuum effects in the vacuum level is thoroughly assessed, in the context of the beam vacuum chamber design presented in the previous publication. Along with their nature, each effect is separately studied, determining the causes of their origin and the most

important parameters contributing to their development. Owing to the lack of experimental data, many estimations have been carried out and the followed procedure is explained. The data acquired with the BESSY-II collaboration is used here to increase the accuracy in the calculation of the e^- cloud density and thus the ESD. Adding all the partial contributions, the resulting gas density evolution inside the vacuum chamber is obtained. The vacuum specifications are found to be achievable within reasonable conditioning times.

All the calculations are carried out with the clear aim in mind of studying the FCC-hh feasibility, choosing always the most pessimistic scenario.

Within the project frame two additional peer-reviewed articles were written. Their contents are highly relevant for this thesis.

- **Commissioning of a beam screen test bench experiment with a future circular hadron collider type synchrotron radiation beam. L. A. González *et al.* [67]. DOI = 10.1103/PhysRevAccelBeams.22.083201**: This paper addresses the motivation, commissioning, elements and the functionalities of BESTEX, including a detailed description of the mounted diagnostics. Preliminary data acquired with the setup is shown. The commissioning and setup design is proved successfully. It was written by the BESTEX WP4 team.

- **Reflectivity and photoelectron yield from copper in accelerators. E. La Francesca *et al.* [108]. DOI = 10.1103/PhysRevAccelBeams.23.083101**: The previously mentioned collaboration between CERN and INFN, arranged to measure the photoelectron yield of FCC-hh BS technical materials, resulted in this publication. It was written by LNF-INFN. It contains further information about the measurements procedure and presents the acquired experimental data.

The Conceptual Design Report (CDR) of the FCC-hh concludes this list.

- **FCC-hh: The Hadron Collider. Future Circular Collider Conceptual Design Report Volume 3. FCC collaboration [1]. DOI = 10.1140/epjst/e2019-900087-0**: This document constitutes the third volume of the FCC Conceptual Design Report, devoted to the hadron collider FCC-hh. It summarizes the physics discovery opportunities, presents the FCC-hh accelerator design, the staged operation plan, discusses the underlying technologies, the civil engineering, technical infrastructure and sketches a possible implementation. A summary of the work presented in this thesis is included.

6.2 Other publications

- **Summary of modelling studies on the beam induced vacuum effects in the FCC-hh. I. Bellafont *et al.* [161]**: Written for the IPAC 2019 proceedings, this publication summarizes the preliminary outcomes of the study of the beam induced effects in the FCC-hh which were obtained by then. It was superseded by the previously mentioned peer-reviewed publications on the FCC-hh vacuum chamber.

- **Results on the FCC-hh Beam Screen Sawtooth at the KIT Electron Storage Ring KARA. L. A. Gonzalez *et al.* [65]**: This publication, part of the IPAC 2019 proceedings, presents the pressure and reflectivity data acquired at BESTEX equipped with the third and latest prototype of the FCC-hh BS. The mounted BS includes the LHC sawtooth finishing Cu on both sides of the chamber, assembled with different orientations. Its primary chamber is treated with LASE. Both sawtooth surfaces are analysed. The obtained results indicate that, as expected, a nominal orientation of the sawtooth profile would be preferable in order to cope with SR in a more efficient way. Although not presented, several simulations were carried out to predict the scattered photon contribution impinging on the conical absorber placed at the exit of the test BS and to predict the system's vacuum level for both orientations.

- **Results on the FCC-hh beam screen at the kit electron storage ring KARA. L. A. González *et al.* [64]**: Written for the IPAC 2018 proceedings. This first publication on BESTEX begins with a short presentation of the setup capabilities. Follows by presenting the first pressure measurements of the irradiation of the two first BS prototypes, along with the previously calculated ones, and the measured current in the clearing electrodes. A reasonably good match between the experimental measurements and the Monte Carlo calculations is observed. Extensive simulations of the SR distribution along the BESTEX beamline were also carried out to guide the slits alignment and as fundamental pre-requisite for the interpretation of the experimental data.

Bibliography

[1] A. Abada *et al.*, "FCC-hh: The Hadron Collider: Future Circular Collider Conceptual Design Report Volume 3," *Eur. Phys. J. ST*, vol. 228, no. 4, pp. 755–1107, 2019.

[2] M. Benedikt, *European Circular Energy Frontier Collider Study*, H2020-INFRADEV-1-2014-1, proposal N^{o} 654305, 2014.

[3] M. Benedikt, M. Capeans Garrido, F. Cerutti, B. Goddard, J. Gutleber, J. M. Jimenez, M. Mangano, V. Mertens, J. A. Osborne, T. Otto, J. Poole, W. Riegler, D. Schulte, L. J. Tavian, D. Tommasini, and F. Zimmermann, "Future Circular Collider - European Strategy Update Documents," CERN, Geneva, Tech. Rep. CERN-ACC-2019-0005, 2019.

[4] (2019). "EuroCirCol WP4 website," [Online]. Available: `fcc.web.cern.ch/eurocircol/Pages/WP4.aspx`.

[5] ATLAS Collaboration, "Observation of a new particle in the search for the Standard Model Higgs boson with the ATLAS detector at the LHC," *Physics Letters B*, vol. 716, no. 1, pp. 1–29, 2012.

[6] CERN. (2012). "Higgs Bosson press release," [Online]. Available: `https://home.cern/news/press-release/cern/cern-experiments-observe-particle-consistent-long-sought-higgs-boson`.

[7] D. Schulte, "FCC-hh Design Highlights," *ICFA Beam Dyn. Newslett.*, vol. 72, 2017.

[8] E. Mobs, "The CERN accelerator complex. Complexe des accélérateurs du CERN," 2016, General Photo.

[9] J. Borburgh and W. Bartmann, *Injector Design*, presentation in the FCC Week 2019, 2019.

[10] M. Benedikt, A. Blondel, O. Brunner, M. Capeans Garrido, F. Cerutti, J. Gutleber, P. Janot, J. M. Jimenez, V. Mertens, A. Milanese, K. Oide, J. A. Osborne, T. Otto, Y. Papaphilippou, J. Poole, L. J. Tavian, and F. Zimmermann, "Future Circular Collider - European Strategy Update Documents," CERN, Geneva, Tech. Rep. CERN-ACC-2019-0003, 2019.

[11] L. Rossi and O. Brüning, "Introduction to the HL-LHC Project," in *The High Luminosity Large Hadron Collider: the new machine for illuminating the mysteries of Universe*, O. Brüning and L. Rossi, Eds. 2015, vol. 24, pp. 1–17.

[12] CERN. (2019). "EuroCirCol - The European Circular Energy-Frontier Collider Study," [Online]. Available: `http://www.eurocircol.eu/`.

[13] O. Gröbner, "Overview of the LHC vacuum system," *Vacuum*, vol. 60, no. 1-2, pp. 25–34, 2001.

[14] A. Chance, *New lattice design*, 4^{th} EuroCirCol General Meeting, 2018.

[15] A. Chancé, D. Boutin, B. Dalena, B. Holzer, A. Langner, and D. Schulte, "Updates on the Optics of the Future Hadron-Hadron Collider FCC-hh," in *Proc. of International Particle Accelerator Conference (IPAC'17), Copenhagen, Denmark, 14-19 May, 2017*, (Copenhagen, Denmark), ser. International Particle Accelerator Conference, Geneva, Switzerland: JACoW, 2017, pp. 2023–2026.

[16] A. Chance, *Lattice integration*, presentation in the FCC Week 2019, Brussels, 2019.

[17] M. Knudsen, "Die gesetze der molekularströmung und der inneren reibungsströmung der gase durch röhren," *Annalen der Physik*, vol. 333, no. 1, pp. 75–130, 1909.

[18] S. P. Parker, *Dictionary of scientific and technical terms*. McGraw-Hill Education, 2003.

[19] B. Sundén and J. Fu, "Chapter 4 - low-density heat transfer: Rarefied gas heat transfer," in *Heat Transfer in Aerospace Applications*, B. Sundén and J. Fu, Eds., Academic Press, 2017, pp. 45 –70.

[20] ULVAC cryogenics. (2020). "Basic Knowledge about Cryopumps," [Online]. Available: `https://www.ulvac-cryo.com/products-en/cryopumps/basic-knowledge-about-cryopumps-1/?lang=en`.

[21] M. Bernardini and L. Malter, "Vacuum problems of electron and positron storage rings," *Journal of Vacuum Science and Technology*, vol. 2, no. 3, pp. 130–141, 1965.

[22] O Gröbner, "The design and performance of the lep vacuum system at cern," *Vacuum*, vol. 43, no. 1, pp. 27 –30, 1992.

[23] V. Baglin, "Etude de la photo-desorption de surfaces techniques aux temperatures cryogeniques," Ph.D. dissertation, 1997, 299 P.

[24] R. Cimino and T. Demma, "Electron cloud in accelerators," *International Journal of Modern Physics A*, vol. 29, no. 17, p. 1 430 023, 2014.

[25] G. Rumolo and G. Iadarola, "Electron Clouds," in *Proceedings of the CAS-CERN Accelerator School: Intensity Limitations in Particle Beams*, 2015.

[26] K. Ohmi, F. Zimmermann, and E. Perevedentsev, "Wake-field and fast head-tail instability caused by an electron cloud," *Phys. Rev. E*, vol. 65, p. 016 502, 1 2001.

[27] O. Gröbner, "Dynamic outgassing," CERN, Geneva, Tech. Rep. CERN-OPEN-2000-275, 1999.

[28] O. S. Bruning, P. Collier, P. Lebrun, S. Myers, R. Ostojic, J. Poole, and P. Proudlock, "LHC Design Report Vol.1: The LHC Main Ring," CERN, Geneva, Tech. Rep. 2004-003-V1, 2004, ch. 12.

[29] O. Gröbner, "The LHC Vacuum System," no. LHC-Project-Report-181. CERN-LHC-Project-Report-181, 5 p, 1998.

[30] O. Gröbner, "The LHC vacuum system," in *Proceedings of the 1997 Particle Accelerator Conference*, vol. 3, IEEE, 1997, pp. 3542–3546.

[31] S. Sgobba and G. Hochortler, "New non-magnetic stainless steel for very low temperature applications," in *International Congress Stainless Steel'99 Science and Market*, vol. 2, 1999, pp. 391–401.

[32] A. Romano, G. Iadarola, K. Li, and G. Rumolo, "Effect of the LHC Beam Screen Baffle on the Electron Cloud Buildup," no. CERN-ACC-2016-256, TUPMW016. 4 p, 2016.

[33] D. Delikaris and L. Tavian, "Heat loads and cryogenics for HE-LHC," 4 p, 2011, Contribution to the EuCARD-AccNet-EuroLumi Workshop: The High-Energy Large Hadron Collider, Malta, 14–16 Oct 2010.

[34] C. Garion, *FCC-hh beam screen studies and cooling scenario*, presentation in the FCC Week 2016, Rome, 2016.

[35] F. Pérez, P. Chiggiato, C. Garion, and J. Fernández, "Preliminary beam screen and beam pipe engineering design," Tech. Rep. EuroCirCol-P2-WP4-D4.3, 2017.

[36] R. Cimino, V. Baglin, and F. Schäfers, "Potential remedies for the high synchrotron-radiation-induced heat load for future highest-energy-proton circular colliders," *Phys. Rev. Lett.*, vol. 115, p. 264 804, 26 2015.

[37] C. Garion, *Cold plasma spray application in the FCC*, presentation in the FCC Week 2017, Berlin, 2017.

[38] P. Lebrun and L. Tavian, "Beyond the Large Hadron Collider: A First Look at Cryogenics for CERN Future Circular Colliders," *Physics Procedia*, vol. 67, pp. 768–775, 2015.

[39] V. Baglin, *Cryogenic Beam Vacuum Specificities Applicable to FCC hh*, presentation in the FCC Week 2015, Washington, 2017.

[40] L. Spallino, M. Angelucci, and R. Cimino, "Thermal desorption of cryopumped gases from laser treated copper," *Phys. Rev. Accel. Beams*, vol. 23, p. 063 201, 6 2020.

[41] L. Spallino, *Material properties of relevance to cryogenic vacuum systems*, presentation in the FCC Week 2019, 2019.

[42] C. Benvenuti, J. Cazeneuve, P. Chiggiato, F. Cicoira, A. E. Santana, V. Johanek, V. Ruzinov, and J. Fraxedas, "A novel route to extreme vacua: The non-evaporable getter thin film coatings," *Vacuum*, vol. 53, no. 1, pp. 219–225, 1999.

[43] P. Manini, A. Conte, S. Raimondi, and A. Bonucci, "Non evaporable getter (neg) coatings for vacuum systems in synchrotron radiation facilities," *AIP Conference Proceedings*, vol. 879, pp. 287–290, Jan. 2007.

[44] P. Costa Pinto, *History and potential of Non Evaporable Getter (NEG) technology*, EIROforum Science-Business WAMAS, Workshop on Advanced Materials and Surfaces, 2013.

[45] P. C. Pinto, S. Calatroni, H. Neupert, D. Letant-Delrieux, P. Edwards, P. Chiggiato, M. Taborelli, W. Vollenberg, C. Yin-Vallgren, J. Colaux, and S. Lucas, "Carbon coatings with low secondary electron yield," *Vacuum*, vol. 98, pp. 29–36, 2013.

[46] C Yin Vallgren, G Arduini, J Bauche, S Calatroni, P Chiggiato, K Cornelis, P Costa-Pinto, B Henrist, E Metral, H Neupert, G Rumolo, E Shaposhnikova, and M Taborelli, "Amorphous carbon coatings for the mitigation of electron cloud in the CERN Super Proton Synchrotron," *Phys. Rev. Spec. Top. Accel. Beams*, vol. 14, no. CERN-OPEN-2011-040, p. 071 001, 2011.

[47] R. Valizadeh and O. B. Malyshev and S. Wang and T. Sian and M.D. Cropper and N. Sykes, "Reduction of secondary electron yield for e-cloud mitigation by laser ablation surface engineering," *Applied Surface Science*, vol. 404, pp. 370–379, 2017.

[48] G. Tang, A. C. Hourd, and A. Abdolvand, "Nanosecond pulsed laser blackening of copper," *Applied Physics Letters*, vol. 101, no. 23, p. 231 902, 2012.

[49] R. Valizadeh, O. B. Malyshev, S. Wang, S. A. Zolotovskaya, W. A. Gillespie, and A. Abdolvand, "Low secondary electron yield engineered surface for electron cloud mitigation," *Applied Physics Letters*, vol. 105, no. 23, p. 231 605, 2014.

[50] V. Baglin, *Cold/sticky systems*, CERN Accelerator School, 2007.

[51] V. Baglin, I. R. Collins, O. Gröbner, C. Grünhagel, and B. Jenninger, "Molecular desorption by synchrotron radiation and sticking coefficient at cryogenic temperatures for H_2, CH_4, CO and CO_2," *Vacuum*, vol. 67, pp. 421–428, Sep. 2002.

[52] R. Kersevan and M. Ady, "Recent developments of Monte-Carlo codes Molflow+ and Synrad+," in *10th International Particle Accelerator Conference*, 2019, TUPMP037.

[53] M. Ady and R. Kersevan. (2019). "Molflow+ and Synrad+ Website," [Online]. Available: `https://molflow.web.cern.ch/`.

[54] R. Kersevan, "SYNRAD: A Monte Carlo synchrotron radiation ray-tracing program," in *Proceedings of International Conference on Particle Accelerators*, Washington D.C.: IEEE, 1993, pp. 3848–3850.

[55] M. Ady and R. Kersevan, "Introduction to the Latest Version of the Test-particle Monte Carlo Code Molflow+," in *Proceedings of IPAC 2014*, Dresden: JACoW, 2014, pp. 2348–2350.

[56] M. Ady, "Monte Carlo simulations of ultra high vacuum and synchrotron radiation for particle accelerators," Ph.D. Thesis, presented 03 May 2016, 2016.

[57] G Dugan and D Sagan, *SYNRAD3D photon propagation and scattering simulations*, Contribution to the Joint INFN-CERN-EuCARD-AccNet Workshop on Electron-Cloud Effects: ECLOUD'12; 5-9 Jun 2012, La Biodola, Isola d'Elba, Italy, 2013.

[58] H. Hogrefe and C. Kunz, "Soft x-ray scattering from rough surfaces: Experimental and theoretical analysis," *Appl. Opt.*, vol. 26, no. 14, pp. 2851–2859, 1987.

[59] R. J. Noll and P. Glenn, "Mirror surface autocovariance functions and their associated visible scattering," *Appl. Opt.*, vol. 21, no. 10, pp. 1824–1838, 1982.

[60] D. Vaughan, "X-ray data booklet. revision," Lawrence Berkeley Lab., Tech. Rep., 1986.

[61] B. Henke, E. Gullikson, and J. Davis, "X-ray interactions: Photoabsorption, scattering, transmission, and reflection at e = 50-30,000 ev, z = 1-92," *Atomic Data and Nuclear Data Tables*, vol. 54, no. 2, pp. 181 –342, 1993.

[62] H. Hagemann, W. Gudat, and C. Kunz, "Optical constants from the far infrared to the x-ray region: Mg, al, cu, ag, au, bi, c, and al2o3," *J. Opt. Soc. Am.*, vol. 65, no. 6, pp. 742–744, 1975.

[63] L. A. Gonzalez, M. Gil-Costa, V. Baglin, P. Chiggiato, C. Garion, R. Kersevan, S. Casalbuoni, E. Huttel, I. Bellafont, and F. Pérez, "Commissioning of a beam screen test bench experiment with a future circular hadron collider type synchrotron radiation beam," *Phys. Rev. Accel. Beams*, vol. 22, p. 083 201, 8 2019.

[64] L. A. Gonzalez, V. Baglin, I. Bellafont, S. Casalbuoni, P. Chiggiato, C. Garion, M. Gil Costa, E. Huttel, R. Kersevan, and F. Pérez, "Results on the FCC-hh beam screen at the KIT electron storage ring KARA," in *Proceedings of IPAC 2018*, Vancouver: JACoW, 2018.

[65] L. A. Gonzalez, F. Pérez, I. Bellafont, V. Baglin, P. Chiggiato, C. Garion, R. Kersevan, S. Casalbuoni, and E. Huttel, "Results on the FCC-hh beam screen sawtooth at the KIT electron storage ring KARA," in *Proceedings of IPAC 2019*, Melbourne: JACoW, 2019, pp. 1323–1326.

[66] L. A. Gonzalez, V. Baglin, I. Bellafont, S. Casalbuoni, P. Chiggiato, C. Garion, E. Huttel, R. Kersevan, and F. Pérez, *Photodesorption Studies on FCC-hh Beam Screen Prototypes at KARA*, presentation in the FCC Week 2019, 2019.

[67] L. A. Gonzalez, M. Gil-Costa, V. Baglin, P. Chiggiato, C. Garion, R. Kersevan, S. Casalbuoni, E. Huttel, I. Bellafont, and F. Perez, "Commissioning of a beam screen test bench experiment with a future circular hadron collider type synchrotron radiation beam," *Phys. Rev. Accel. Beams*, vol. 22, p. 083 201, 8 2019.

[68] V Baglin, I. R. Collins, C Grünhagel, O. Gröbner, and B Jenninger, "First Results from COLDEX Applicable to the LHC Cryogenic Vacuum System," 4 p, 2000.

[69] R. Salemme, V. Baglin, F. Bellorini, G. Bregliozzi, K. Brodzinski, P. Chiggiato, P. Costa Pinto, P. Gomes, A. Gutierrez, V. Inglese, B. Jenninger, R. Kersevan, E. Michel, M. Pezzetti, B. Rio, and A. Sapountzis, "Recommissioning of the COLDEX Experiment at CERN," no. CERN-ACC-2015-242, WEPHA006. 3 p, 2015.

[70] D. H. Tomboulian and P. L. Hartman, "Spectral and angular distribution of ultraviolet radiation from the 300-mev cornell synchrotron," *Phys. Rev.*, vol. 102, pp. 1423–1447, 6 1956.

[71] V. Baglin, G. Bregliozzi, J. M. Jimenez, and G. Lanza, "Synchrotron Radiation in the LHC Vacuum System," in *Proceedings of IPAC 2011*, vol. C110904, 2011, pp. 1563–1565.

[72] A. Hofmann, "Characteristics of Synchrotron Radiation," in *CERN Accelerator School (CAS): Synchrotron Radiation and Free Electron Lasers Chester*, 1989, pp. 115–141.

[73] CERN. (2019). "Beam Lifetime. Taking a closer look at LHC," [Online]. Available: `https://www.lhc-closer.es/taking_a_closer_look_at_lhc/0.beam_lifetime`.

[74] I. Bellafont, L. Mether, R. Kersevan, O. B. Malyshev, V. Baglin, P. Chiggiato, and F. Pérez, "Beam induced vacuum effects in the future circular hadron collider beam vacuum chamber," *Phys. Rev. Accel. Beams*, vol. 23, p. 043 201, 4 2020.

[75] C. Kotnig, *Cold mass cooling with supercritical helium*, 2^{nd} FCC Cryogenics Day, 2016.

[76] T. Böhlen, F. Cerutti, M. Chin, A. Fasso, A. Ferrari, P. Ortega, A. Mairani, P. Sala, G. Smirnov, and V. Vlachoudis, "The fluka code: Developments and challenges for high energy and medical applications," *Nuclear Data Sheets*, vol. 120, pp. 211–214, 2014.

[77] A. Ferrari, P. R. Sala, A. Fasso, and J. Ranft, "FLUKA: A multi-particle transport code (Program version 2005)," 2005.

[78] J. R. Hunt, *Update on R2E and heat load simulations*, FCC Week 2019, 2019.

[79] I. Bellafont, M. Morrone, L. Mether, J. Fernández, R. Kersevan, C. Garion, V. Baglin, P. Chiggiato, and F. Pérez, "Design of the future circular hadron collider beam vacuum chamber," *Phys. Rev. Accel. Beams*, vol. 23, p. 033 201, 3 2020.

[80] J. R. Hunt, CERN, personal communication, 2019.

[81] O. S. Bruning, P. Collier, P. Lebrun, S. Myers, R. Ostojic, J. Poole, and P. Proudlock, *LHC Design Report Vol.1: The LHC Main Ring*. 2004, ch. 12.

[82] O. Gröbner, "Overview of the LHC vacuum system," *Vacuum*, vol. 60, no. 1-2, pp. 25–34, 2001.

[83] I. Bellafont, *Photon tracing and gas-density profile in the FCC-hh*, presentation in the FCC Week 2017, Berlin, 2017.

[84] C. Garion, CERN, personal communication, 2017.

[85] L. Mether, CERN, personal communication, 2018.

[86] L. Tavian, CERN, personal communication, 2017.

[87] P. Loïez, P. Rakosy, and L. Guiraud, "Beam screens for the LHC beam pipes. Les conduits pour les faisceaux LHC," 1997.

[88] V. Baglin, P. Lebrun, L. Tavian, and R. van Weelderen, "Cryogenic Beam Screens for High-Energy Particle Accelerators," CERN, Geneva, Tech. Rep. CERN-ATS-2013-006, 2013.

[89] A. Sven, *Betatron collimation system insertion*, FCC Week 2017, 2017.

[90] E. Métral, "Beam screen issues," in *EuCARD-AccNet-EuroLumi Workshop: The High-Energy Large Hadron Collider (HE-LHC10) 2010*, included in CERN Yellow Report CERN-2011-003, pp. 83-89, 2011.

[91] P Duthil, "Material Properties at Low Temperature," in *Proceedings of CAS 2013*, 2014, pp. 77–95. arXiv: 1501.07100.

[92] S. Arsenyev and D. Schulte, *Impedance of cold beamscreen*, FCC Week, Amsterdam, 2018.

[93] A. Sven, CERN, personal communication, 2017.

[94] S. Arsenyev, *Impedance budget and stability*, FCC Week, Brussels, 2019.

[95] D. Astapovych, personal communication, 2019.

[96] R. Valizadeh, M. Cropper, P. Goudket, O. Malyshev, B. Sian, N. Sykes, and S. Wang, "Low Secondary Electron Yield of Laser Treated Surfaces of Copper, Aluminium and Stainless Steel," in *Proceedings of IPAC 2016, Busan, Korea*, JACoW, 2016, pp. 1089–1092.

[97] L. Spallino, M. Angelucci, R. Larciprete, and R. Cimino, "On the compatibility of porous surfaces with cryogenic vacuum in future high-energy particle accelerators," *Applied Physics Letters*, vol. 114, no. 15, p. 153 103, 2019.

[98] V. Baglin, P. Chiggiato, and C. Garion, *Vacuum System in The High Luminosity Large Hadron Collider*, To be published, CERN, Geneva, 2020.

[99] K.-H. Leitz, B. Redlingshöfer, Y. Reg, A. Otto, and M. Schmidt, "Metal ablation with short and ultrashort laser pulses," *Physics Procedia*, vol. 12, pp. 230 – 238, 2011, Lasers in Manufacturing 2011 - Proceedings of the Sixth International WLT Conference on Lasers in Manufacturing.

[100] R. Valizadeh, A. Hannah, J. Much, D. Whitehead, P. Krkotic, O. B. Malyshev, J. M. O'Callaghan, and M. Pont, *Evaluation of LASER ablated surface engineering of copper and stainless steel for particle accelerators*, presentation in the in the in FCC Week 2019, 2019.

[101] S. Calatroni, M. Arzeo, S. Aull, M. Himmerlich, P. Costa Pinto, W. Vollenberg, B. Di Girolamo, P. Cruikshank, P. Chiggiato, D. Bajek, S. Wackerow, and A. Abdolvand, "Cryogenic surface resistance of copper: Investigation of the impact of surface treatments for secondary electron yield reduction," *Phys. Rev. Accel. Beams*, vol. 22, p. 063 101, 6 2019.

[102] F. Pérez, P. Chiggiato, O. B. Malyshev, R. Valizadeh, T. Sian, and R. Sirvinskaite, "Proposal on surface engineering to mitigate electron cloud effects," Tech. Rep. EuroCirCol-P2-WP4-M4.4, 2017.

[103] S. Arsenyev and D. Schulte, "Broadband Impedance of Pumping Holes and Interconnects in the FCC-hh Beamscreen," in *Proceedings of IPAC 2018*, 2018, pp. 153–156.

[104] G. Guillermo, D. Sagan, and F. Zimmermann, "Simulating Proton Synchrotron Radiation in the Arcs of the LHC, HL-LHC and FCC-hh," in *Proceedings of IPAC 2016, Busan, Korea*, JACoW, 2016, pp. 2073–2076.

[105] G. Guillermo, D. Sagan, and F. Zimmermann, "Examining mitigation schemes for synchrotron radiation in high-energy hadron colliders," *Physical Review Accelerators and Beams*, vol. 21, no. 2, p. 021 001, 2018.

[106] A. Sokolov, F. Eggenstein, A. Erko, R. Follath, S. Künstner, M. Mast, J. Schmidt, F. Senf, F. Siewert, T. Zeschke, *et al.*, "An XUV optics beamline at BESSY-II," in *Advances in Metrology for X-Ray and EUV Optics V*, International Society for Optics and Photonics, vol. 9206, 2014, 92060J.

[107] E. La Francesca, "Material science and accelerator R&D: Reflectivity and Photo Yield measurements of vacuum chamber technical Surfaces," Ph.D. dissertation, Rome U., 2019.

[108] E. La Francesca, M. Angelucci, A. Liedl, L. Spallino, L. A. Gonzalez, I. Bellafont, F. Siewert, M. G. Sertsu, A. Sokolov, F. Schäfers, and R. Cimino, "Reflectivity and photoelectron yield from copper in accelerators," *Phys. Rev. Accel. Beams*, vol. 23, p. 083 101, 8 2020.

[109] E. La Francesca, A. Liedl, M. Angelucci, M. G. Sokolov A.and Sertsu, F. Schäfers, F. Siewert, and R. Cimino, *Study of reflectivity and photo yield on FCC-hh proposed beam screen surfaces*, poster in FCC Week 2018, 2018.

[110] A. Liedl, E. La Francesca, M. Angelucci, and R. Cimino, *Photo reflectivity and photo electron yield of technical surfaces*, presentation in ECLOUD'18, 2018.

[111] O. S. Brüning, P. Collier, P Lebrun, S. Myers, R. Ostojic, J. Poole, and P. Proudlock, *LHC Design Report*, ser. CERN Yellow Reports: Monographs. Geneva: CERN, 2004, ch. 12.

[112] P Cruikshank, K Artoos, F Bertinelli, J. C. Brunet, R Calder, C Campedel, I. R. Collins, J. M. Dalin, B Feral, O. Gröbner, N Kos, A. G. Mathewson, L. I. Nikitina, I. N. Nikitin, A. Poncet, C Reymermier, G Schneider, J. C. Sexton, S. Sgobba, R Valbuena, and R. J. M. Veness, "Mechanical design aspects of the LHC beam screen," Tech. Rep. CERN-LHC-Project-Report-128, 1997.

[113] M. Chorowski, H. Correia, D. Delikaris, P. Duda, C. Haberstroh, F. Holdener, S. Klöppel, C. Kotnig, F. Millet, J. Polinski, H. Quack, and L. Tavian, "Towards the conceptual design of the cryogenic system of the Future Circular Collider (FCC)," in *Cryogenic Engineering Conference and International Cryogenic Materials Conference 2017 (CEC/ICMC'17)*, vol. 278, 2017, p. 012 097.

[114] C. Kotnig, CERN, personal communication, 2017.

[115] N. Kos, "LHC Beam screen insertion tests with sliding rings," CERN, Geneva, Tech. Rep. VACUUM-TECHNICAL-NOTE-00-06, 2000.

[116] L. R. Evans, *The Large Hadron Collider: a marvel of technology. Second edition*. EPFL Press, 2009, p. 102.

[117] C. Garion, *Considerations for large scale production of the FCC-hh beam screens*, FCC Week 2019, 2019.

[118] M. Benedikt *et al.*, "Cost estimate for the FCC-hh," CERN, Tech. Rep., personal communication.

[119] G Iadarola and G Rumolo, "PyECLOUD and build-up simulations at CERN," in *Proceedings of ECLOUD'12*, 2013.

[120] G. Iadarola, G. Rumolo, and G. Miano, "Electron cloud studies for CERN particle accelerators and simulation code development," Presented 23 May 2014, Ph.D. dissertation, 2014.

[121] M. A. Furman and M. T. F. Pivi, "Probabilistic model for the simulation of secondary electron emission," *Phys. Rev. ST Accel. Beams*, vol. 5, p. 124 404, 12 2002.

[122] R. E. Kirby and F. K. King, "Secondary electron emission yields from PEP-II accelerator materials," *Nucl. Instrum. Meth.*, vol. A469, pp. 1–12, 2001.

[123] R. Cimino, I. R. Collins, M. A. Furman, M. Pivi, F. Ruggiero, G. Rumolo, and F. Zimmermann, "Can low-energy electrons affect high-energy physics accelerators?" *Phys. Rev. Lett.*, vol. 93, p. 014 801, 1 2004.

[124] V Baglin, I Collins, B. Henrist, N. Hilleret, and G Vorlaufer, "A Summary of Main Experimental Results Concerning the Secondary Electron Emission of Copper," CERN, Geneva, Tech. Rep. LHC-Project-Report-472, 2001.

[125] B. Henrist, N. Hilleret, M. Jimenez, C. Scheuerlein, M. Taborelli, and G. Vorlaufer, "Secondary electron emission data for the simulation of electron cloud," in *Proceedings of ECLOUD'02*, 2002, pp. 75–78.

[126] R. Cimino and I. Collins, "Vacuum chamber surface electronic properties influencing electron cloud phenomena," *Applied Surface Science*, vol. 235, no. 1, pp. 231 –235, 2004.

[127] L. Mether, *Electron cloud*, FCC Week 2019, 2019.

[128] M. Angelucci, A. Novelli, L. Spallino, A. Liedl, R. Larciprete, and R. Cimino, "Minimum thickness of carbon coating for multipacting suppression," *Phys. Rev. Research*, vol. 2, p. 032 030, 3 2020.

[129] K Ohmi, "Electron cloud effect in damping rings of linear colliders," in *Proceedings of ECLOUD'04*, CERN, Geneva: CERN, 2005.

[130] L. Mether, *Electron cloud*, FCC Week 2018, 2018.

[131] *COMSOL Multiphysics Reference Manual*, 2017.

[132] M. Morrone, *Update of the design and thermal mechanical study of the FCC-hh beam screen*, FCC Week 2019, 2019.

[133] R. Calder, O. Gröbner, A. G. Mathewson, V. V. Anashin, A. Dranichnikov, and O. B. Malyshev, "Synchrotron radiation induced gas desorption from a Prototype Large Hadron Collider beam screen at cryogenic temperatures," *Journal of Vacuum Science & Technology A*, vol. 14, no. 4, pp. 2618–2623, 1996.

[134] C. Herbeaux, P. Marin, V. Baglin, and O. Gröbner, "Photon stimulated desorption of an unbaked stainless steel chamber by 3.75 keV critical energy photons," *Journal of Vacuum Science & Technology A*, vol. 17, no. 2, pp. 635–643, 1999.

[135] J. Gómez-Goñi, O. Gröbner, and A. G. Mathewson, "Comparison of photodesorption yields using synchrotron radiation of low critical energies for stainless steel, copper, and electrodeposited copper surfaces," *Journal of Vacuum Science & Technology A*, vol. 12, no. 4, pp. 1714–1718, 1994.

[136] V. Anashin, A. Bulygin, O. Malyshev, L. Mironenko, E. Pyata, V. Volkov, and D. Kramer, "Photodesorption and power testing of the SR crotch-absorber for BESSY-II," in *Proceedings of EPAC'98*, 1998, pp. 2163–2165.

[137] V. Baglin, "Measurement of the primary phodesorption yield at 4.2 K, 77 K and room temperature in a quasi-closed geometry," CERN, Geneva, Tech. Rep. LHC Project Report 9, 1996.

[138] O. Gröbner, A. G. Mathewson, and P. C. Marin, "Gas desorption from an oxygen free high conductivity copper vacuum chamber by synchrotron radiation photons," *Journal of Vacuum Science & Technology A*, vol. 12, no. 3, pp. 846–853, 1994.

[139] C. Foerster, H. Halama, G. Korn, M. Calderon, and W. Barletta, "Desorption measurements of copper and copper alloys for PEP-II," *Vacuum*, vol. 44, no. 5, pp. 489–491, 1993.

[140] R. Cimino, M. Commisso, D. R. Grosso, T. Demma, V. Baglin, R. Flammini, and R. Larciprete, "Nature of the decrease of the secondary-electron yield by electron bombardment and its energy dependence," *Phys. Rev. Lett.*, vol. 109, p. 064 801, 6 2012.

[141] T. Kobari, M. Matumoto, S. Ueda, M. Kobayashi, and Y. Hori, "Surface treatments and photodesorption of oxygen free copper used in an accelerator," in *Proceedings of International Conference on Particle Accelerators*, IEEE, 1993, pp. 3903–3905.

[142] M. Benedikt, D. Schulte, and F. Zimmermann, "Optimizing integrated luminosity of future hadron colliders," *Phys. Rev. Spec. Top. Accel. Beams*, vol. 18, no. CERN-ACC-2015-0166. 10, p. 101 002, 2015.

[143] V. V. Anashin, O. B. Malyshev, R. Calder, and O. Gröbner, "A study of the photodesorption process for cryosorbed layers of H_2, CH_4, CO or CO_2 at various temperatures between 3 K and 68 K," *Vacuum*, vol. 53, no. 1, pp. 269 –272, 1999.

[144] O. Gröbner, VLHC Workshop, CERN-LHC/VAC, 2000.

[145] V. Baglin, I. R. Collins, O. Gröbner, C. Grünhagel, and B. Jenninger, "Synchrotron radiation studies of the LHC dipole beamscreen with COLDEX," in *Proceedings of EPAC 2002*, 2002, pp. 2535–2537.

[146] O. B. Malyshev, V. V. Anashin, I. R. Collins, and O. Gröbner, "Photon stimulated desorption processes including cracking of molecules in a vacuum chamber at cryogenic temperatures," CERN, Geneva, Tech. Rep. Technical Note 99-13, Jan. 1999.

[147] V. Baglin and B. Jenninger, CERN, Geneva, Tech. Rep. Coldex Run 24, Sep. 1999.

[148] I. R. Collins and O. B. Malyshev, "Dynamic gas density in the LHC interaction regions 1&5 and 2&8 for optics version 6.3," CERN, Geneva, Tech. Rep. LHC-Project-Note-274, Dec. 2001.

[149] F. Billard, N. Hilleret, and G. Vorlaufer, "Some results on the electron induced desorption yield of ofhc copper," CERN, Geneva, Tech. Rep. Vacuum Technical Note 00-32, 2000.

[150] V. V. Anashin, I. R. R. Collins, R. V. Dostovalov, N. V. Fedorov, O. Gröbner, A. Krasnov, O. B. Malyshev, and E. Pyata, "Magnetic and Electric Field Effects on the Photoelectron Emission from Prototype LHC Beam Screen Material," *Vacuum*, vol. 60, Jan. 2001.

[151] Malyshev, O. B. and Rossi, A., "Ion desorption stability in the LHC," CERN, Geneva, Tech. Rep. Vacuum Technical Note 99-20, 1999.

[152] O. B. Malyshev, "The energy of the ions bombarding the vacuum chamber walls," CERN, Geneva, Tech. Rep. Vacuum Technical Note 99-17, Nov. 1999.

[153] O. Malyshev, "The ion impact energy on the LHC vacuum chamber walls," in *Proceedings of EPAC 2000*, Jun. 2000, pp. 951–953.

[154] O. B. Malyshev, "Ion induced pressure instability in the ILC positron DR," in *Proceedings of IPAC 2010*, Kyoto, May 2010, pp. 3566–3568.

[155] F. F. Rieke and W. Prepejchal, "Ionization cross sections of gaseous atoms and molecules for high-energy electrons and positrons," *Physical Review A*, vol. 6, pp. 1507–1519, Oct. 1972.

[156] V. Baglin, *The HL-LHC vacuum and beam dynamics issues*, presentation in the Beam Dynamics meets Vacuum, Collimations and Surfaces workshop, 2017.

[157] A. W. Chao and M. Tigner, *Handbook of Accelerator Physics and Engineering (3rd Printing)*. 1999.

[158] Stanford Research Systems (SRS) Website. (2018). "Bayard-Alpert Ionization Gauges," [Online]. Available: `https://www.thinksrs.com/downloads/PDFs/ApplicationNotes/IG1BAGapp.pdf`.

[159] L. A. Gonzalez, CERN, personal communication, 2019.

[160] (2019). "Physical Review - Accelerators and Beams (PRAB) journal," [Online]. Available: `https://journals.aps.org/prab`.

[161] I. Bellafont, R. Kersevan, and L. Mether, "Summary of modelling studies on the beam induced vacuum effects in the FCC-hh," in *Proceedings of IPAC2019, Melbourne, Australia, May 19-24*, 2019, pp. 1331–1334.